# Source Characteristics of Large Earthquakes at Short Periods

Thesis by

Heidi Houston

In Partial Fulfillment of the Requirements

for the Degree of

Doctor of Philosophy

California Institute of Technology

Pasadena, California

1987

(submitted December 18, 1986)

## Acknowledgements

I am very grateful to John Vidale for his support, encouragement, and page numbering skills. I thank my research advisor, Hiroo Kanamori, for his guidance, wisdom, and humor. I thank the students, faculty, and staff of the Seismo. Lab. for their help and friendship.

## Abstract

In Chapter 1, we analyzed short-period body waves recorded at teleseismic distances from great earthquakes. They provide information about source rupture processes and strong motions. First, we examined records of 19 earthquakes of moment magnitude $M_W$ of 6.5 to 9.5. Four parameters were measured from the short-period P-wave train: the maximum amplitude, the period at maximum amplitude, the time between the first arrival and when the maximum amplitude is attained, and coda length. An extension, $\hat{m}_b$, of the teleseismic body-wave magnitude, $m_b$, was defined using the maximum amplitude of the entire short-period P wave rather than the amplitude achieved in the first few P-wave cycles. $\hat{m}_b$ increases as $M_W$ increases. The time from the first arrival until the maximum amplitude is achieved and the coda length are roughly proportional to $M_W$, but were further interpreted by a simple asperity model of the rupture process. These data support that 1 to 2 sec waves are on average generated preferentially in the same regions of the fault plane as 10 to 50 sec waves.

An application to strong motion modeling is presented in which a 1971 San Fernando teleseismic short-period record is summed up to simulate teleseismic records produced by five great earthquakes. The summation procedure matches the moment of the event to be simulated, and includes rupture propagation, fault plane roughness, and randomness. The $\hat{m}_b$ data provide an important constraint on the summation procedure. Thus constrained, this summation procedure can be more confidently used with near-field strong motion records as Green's functions to predict strong motions from great

earthquakes.

In Chapter 2, we analyzed the spectra of short- and intermediate-period teleseismic GDSN (digital) records for seven large earthquakes and hand-digitized short-period analog records of the 1971 San Fernando earthquake. To obtain the source or moment-rate spectrum at periods between 1 and 30 sec, we Fourier-transformed the P waves, corrected for instrument response, attenuation, geometrical spreading, and radiation pattern (including the depth phases), and then averaged the records for each event. Significant differences exist between the spectra of different events, presumably due to variations in tectonic setting or seismic coupling. Using the digital data, we also investigated the relationship between time-domain amplitude and spectral amplitude for short-period P waves. From our empirical relation between spectral amplitude and time-domain amplitude, we estimated the spectral amplitudes implied by the $\hat{m}_b$ data. We compared our results to the $\omega^{-2}$ and Gusev source spectral models. Neither model can completely represent the data. Nevertheless, we consider the $\omega^{-2}$ model a useful reference model for comparing different events. The average source spectrum of six large events with $M_W$'s of 7.4 to 7.8 does not have the spectral structure suggested by Gusev.

In Chapter 3, source characteristics of the Sept. 19, 1985 Michoacan, Mexico earthquake and its aftershock on Sept. 21 are inferred from broadband and short-period teleseismic GDSN records. We obtained the teleseismic source spectrum from 1 to 30 sec. The Michoacan source spectrum is enriched at 30 sec and depleted at 1 to 10 sec relative to an average source spectrum of large interplate subduction events. Source spectra for the Sept. 21 aftershock, 1981 Playa Azul, 1979 Petatlan, and 1978 Oaxaca events follow a trend similar to

that of the 1985 Michoacan event. This spectral trend may characterize the Mexican subduction zone.

A station-by-station least-squares inversion of the Michoacan earthquake records for the source time function yields three source pulses, which we interpreted as events on the fault plane. The first two are similar in moment, and the third contains only 20% of the moment of the first. Directivity is evident in the timing. At each station, we measured the time differences between the pulses, and performed a least-squares nonlinear estimation of the strike, distance, and time separation between the events to locate them relative to one another. The second event occurred 26 sec after the first, and 82 km southeast of it, indicating southeastward rupture along the trench. The two large events are also seen in the near-field strong motions.

The mainshock records, spectrum, and time functions contain less high frequency radiation than those of the 1985 Valparaiso, Chile earthquake. Apparently, the Michoacan earthquake ruptured two relatively smooth, strong patches which generated large 30 sec waves, but small 1 to 10 sec waves. Such behavior contrasts with the Valparaiso event which had a more complex rupture process and generated more 1 to 5 sec energy. This difference is consistent with the higher near-field accelerations recorded for the Valparaiso event.

In Chapter 4, time functions and rupture processes of 4 recent large subduction zone earthquakes were determined from broadband teleseismic GDSN records using the iterative inversion technique of Kikuchi and Fukao. The method inverts the records simultaneously by determining the location, time, and seismic moment of a single point source that best explains the records,

then subtracting the synthetics for that point source from the records, and repeating the procedure for the residual records. Using this technique with the high-quality GDSN intermediate-band records provides more details of the rupture process than have been obtained previously.

Using the inversion, we produced maps of the spatial and temporal distribution of seismic moment release at periods of 3 to 30 sec for the 1985 Michoacan, Mexico, 1983 Akita-Oki, Japan, 1985 Valparaiso, Chile, and 1986 Andreanof Islands, Alaska earthquakes. These are four of the largest earthquakes that occurred from 1983 to 1986. Comparing the source spectra of these events yields complementary information at periods of 1 to 30 sec. These four earthquakes have distinct rupture styles.

In Chapter 5, we compared strong motion spectra of the 1985 Michoacan, Mexico and the 1983 Akita-Oki, Japan earthquakes with their teleseismic spectra. The spectral levels of the Michoacan strong motions, which were recorded by a high-quality digital array, agree to within a factor of 2 with those predicted by the Michoacan teleseismic records. The Michoacan teleseismic spectrum is lower than that of Akita-Oki. This relationship also holds for their strong motion spectra. This consistency means that teleseismic records, which are relatively more abundant, can be used to predict properties of strong motions from large earthquakes.

# Table of Contents

**Chapter 4**: Broad-band Rupture Process of 4 Large Subduction Zone Earthquakes:
Spatial Distribution of Seismic Moment Release

**Chapter 5**: Comparison of Strong Motion Spectra with Teleseismic Spectra

# Introduction

This thesis examines intermediate (1 to 30 seconds) and short (1 to 10 seconds) period seismograms of large and great earthquakes recorded at teleseismic distances. We need to understand the processes that occur during the rupture of large earthquakes to predict their damaging motions and ultimately perhaps to predict their occurrence.

My thesis focuses on large and great earthquakes because they can cause great destruction. Large earthquakes are recorded world-wide on many seismometers, so there exists a relatively complete record to study. Most of the earthquakes studied here are shallow subduction earthquakes because most large earthquakes occur at subduction plate boundaries at a shallow depth.

In seismology we often wish to separate the properties of the source of seismic waves from the effects of propagation of the waves through possibly complicated earth structures. Wave propagation is a complex phenomenon and the detailed structure is generally not known. Therefore, many studies, including this one, concentrate on teleseismic waves (that is, waves recorded at distances of 30° to 90°) which turn in the relatively simple and well-characterized lower mantle of the earth.

I study seismic body waves which have periods of 1 to 30 seconds because a sizeable number of such records exist, and because waves with periods of 1 to 10 seconds can cause considerable damage to large structures, such as buildings, bridges, and off-shore oil platforms. Shorter period waves are also of engineering concern, but are so attenuated at teleseismic distances that they cannot be interpreted with our current knowledge of the earth's attenuation.

At periods of 1 to 5 seconds, seismic waves from large earthquakes are too complicated to model deterministically, but the general character of the waveform still reflects properties of the seismic source. We can use average or integrated quantities, such as the spectrum, to characterize the source.

My work is oriented toward examining data and extracting important information about the source. Each chapter analyzes a different type of data or data set. Earthquake data is usually very noisy and factors of 3 or 5 or 10 difference in any given quantity for different stations or earthquakes are common. We try, therefore, to average together many stations for a given earthquake in order to reduce the uncertainty due to the scatter. Every earthquake is different, so we also average together many earthquakes of a given size to determine an average earthquake property.

Chapter 1 examines analog short-period seismograms of large and great earthquakes. These are virtually the only short-period records of the largest earthquakes in this century.

Recently, high-quality broadband digital data have become available. In Chapter 2, I have performed a spectral analysis of these records. A procedure to obtain the source spectrum at periods of 1 to 30 seconds is described.

Chapter 3 applies the techniques developed in Chapter 2 to the destructive 1985 Michoacan, Mexico earthquake. I have compared its source spectrum to that of other large earthquakes along the Mexican subduction zone and to the 1985 Valparaiso, Chile earthquake.

In Chapter 4, I have inverted broadband digital records to learn about the time history of the source and the spatial distribution of seismic moment release on the fault planes of four recent large earthquakes.

Chapter 5 compares the spectra of two sets of strong motion seismograms recorded close to the source with the teleseismic spectra studied in the previous chapters. The comparison indicates that teleseismic records can be used to estimate ground motions near large earthquakes.

Chapters 1 and 2 were published as 'Source spectra of great earthquakes: teleseismic constraints on rupture process and strong motion', *Bulletin of the Seismological Society of America, 76*, 19-42, 1986. Chapter 3 appeared in a slightly abbreviated form as 'Source characteristics of the 1985 Michoacan, Mexico earthquake at periods of 1 to 30 seconds', *Geophysical Research Letters, 13*, 597-600, 1986. The appendix has not been published before.

# Chapter 1

# Time Domain Characteristics of Short Period Records

## Abstract

Short-period body waves recorded at teleseismic distances from great earthquakes provide information about source rupture processes and strong motions. First, we examine mostly WWSSN records of 19 earthquakes with moment magnitude $M_W$ of 6.5 to 9.5. Four parameters are measured from the entire P wave: the maximum amplitude, the period at maximum amplitude, the time between the first arrival and when the maximum amplitude is attained, and coda length. An extension $\hat{m}_b$, of the teleseismic magnitude $m_b$, is defined using the maximum amplitude of the entire short-period P wave rather than the amplitude achieved in the first few cycles of the P wave. A least-squares fit to the data yields the following relationship between $\hat{m}_b$ and $M_W$: $\hat{m}_b = 0.53\ M_W + 2.70$ in the range $M_W = 6.5$ to 9.5. The time from the first arrival until the maximum amplitude is achieved and the coda length are roughly proportional to $M_W$, but are further interpreted by a simple asperity model of the rupture process. These data support that short-period waves are on average generated preferentially in the same regions of the fault plane as long-period waves (with periods of 10 to 50 seconds).

An application to strong motion modeling is presented in which a 1971 San Fernando teleseismic short-period record is summed up to simulate teleseismic records produced by five great earthquakes. The summation procedure matches the moment of the event to be simulated, and includes rupture propagation, fault plane roughness, and randomness. The $\hat{m}_b$ data provide an important constraint on the summation procedure. Thus constrained, this summation procedure can be more confidently used with near-field strong motion records as Green's functions to predict strong motions from great earthquakes.

## 1.1 Introduction

Although the earthquake source spectrum is commonly characterized well at long periods by seismic moment, it is poorly determined at shorter periods. In this chapter, we are concerned with periods of 1 to 10 seconds and refer to these as short periods, although strong motions with periods of 1 to 10 seconds are commonly called long-period strong motions. The source spectrum at short periods has implications for the earthquake rupture process and for strong motion. For example, knowledge of the earthquake source at periods of 1 to 10 seconds is important for the safe engineering design of large structures such as high-rise buildings or oil drilling platforms near fault zones, particularly near subduction zones.

Strong ground motions from great earthquakes have not been recorded reliably due to the infrequent occurrence of great earthquakes and the large amplitudes generated by great earthquakes that saturate most nearby seismometers. Therefore, the nature of the source spectrum of great earthquakes is poorly known at present. However, short-period waves from great earthquakes have been recorded at teleseismic distances. Figure 1.1 shows short-period records of some great earthquakes from the Worldwide Standardized Seismographic Network (WWSSN). The P waveforms in Figure 1.1 have durations of 2 to 5 minutes. Because these waveforms are so complex, it is impossible to analyze them deterministically, but the overall character of the waveform can provide useful information on the seismic source. Despite the importance of short-period radiation, only a few studies have been made of these teleseismic records due to their complexity (Koyama and Zheng, 1983,

- 6 -

ALASKA Mar. 28, 1964 $M_w$=9.2

BOG     78.0°     x12500



RAT ISLAND Feb. 4, 1965 $M_w$=8.7

ESK     73.7°     x12500



TOKACHI-OKI May 16, 1968 $M_w$=8.2

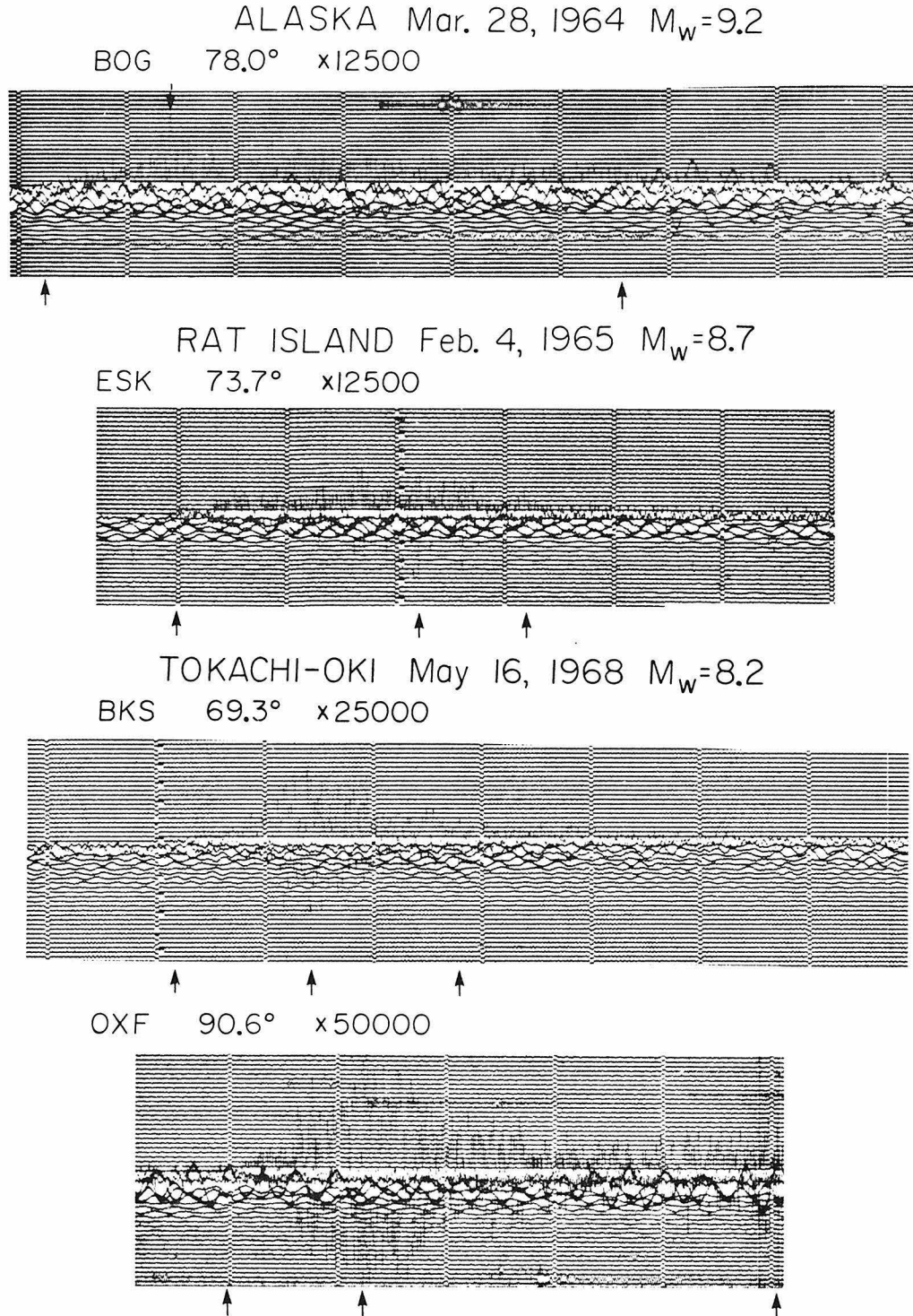BKS     69.3°     x25000



OXF     90.6°     x50000



Figure 1.1. Teleseismic short-period vertical records of three great earthquakes recorded by WWSSN. Note the minute marks. The first and second arrows show the beginning of the P wave and the time the maximum amplitude is achieved. The time between the first and last arrow is the coda length as defined in the text.

1985; Houston and Kanamori, 1983; Purcaru, 1984).

The WWSSN has operated since the early 1960's and has recorded 7 earthquakes with surface-wave magnitudes greater than 8.0. In this chapter, we present a new data set characterizing great earthquakes at short periods. First, we examine WWSSN records of 18 earthquakes of magnitude 6.5 to 9.2 and various short-period records for the 1960 Chilean event of magnitude 9.5. We define a magnitude, $\hat{m}_b$, which is determined at teleseismic distances but is analogous to local magnitude, $M_L$, determined at short distances. Four parameters are measured from the short-period P wave: the maximum amplitude, the period at maximum amplitude, the time between the first arrival and when the maximum amplitude is attained, and coda length. Our parameterization of the overall character of the waveform is interpreted in terms of a simple asperity model of the rupture process. Finally, we discuss the implications of these data for predictions of strong motions.

## 1.2 Short-Period WWSSN Data

For all but one of the 19 events studied, we examined 8 to 27 records from WWSSN short-period vertical seismometers at teleseismic distances of 30 to 100 degrees. For the 1960 Chilean event, various short-period records were used, including records written by Benioff short-period, Wood-Anderson, Willmore short-period, and Milne-Shaw seismometers. More than 330 records were studied.

We measured A, the maximum amplitude seen in the P-wave record, and T, the period at the maximum amplitude. An extension, $\hat{m}_b$, of the teleseismic

magnitude, $m_b$, is defined using the maximum amplitude of the entire short-period P wave rather than the maximum amplitude achieved in the first few cycles of the P wave:

$$\hat{m}_b = \log \frac{A_g}{T} + Q(\Delta) \qquad (1.1)$$

where $A_g$ is the true amplitude of the maximum ground displacement obtained from A and the instrument gain at T, and $Q(\Delta)$ is the empirical Gutenberg-Richter distance calibration function for PZ waves (or PH waves for Wood-Anderson records of the 1960 Chilean event). The period at the maximum amplitude, T, enters (1.1) explicitly, and implicitly through $A_g$ because the gain depends strongly on T. Koyama and Zheng (1985) measured an average period of several cycles around the maximum amplitude (Koyama, pers. comm., 1985). The range of T that we measured can be seen in Figure 1.4c. We also measured $T_M$, the time between the first arrival of energy and the time of the maximum amplitude, and C, the coda length, which we define as the time from the first arrival until the peak-to-peak amplitude on the record has decreased to A/2; that is, until the amplitude has decreased to about 25% of its maximum value. Examples of picks of $T_M$ and C are shown in Figure 1.1. The appendix contains $A_g$ (in microns), T (sec), C (min.), $T_M$ (min.), and $\hat{m}_b$ for each record. Table 1 presents average values of T, C, $T_M$, and $\hat{m}_b$ for each earthquake. Moment magnitude, $M_W$, and surface-wave magnitude, $M_S$, are also listed for comparison (mostly taken from Lay, Kanamori, and Ruff, 1982). All events in Table 1 are subduction-zone thrust events except: #4, which is an intraplate normal faulting event at the trench, #13, 14, 15, 16, and 18, which are strike-slip events, and #17, which is an intraplate thrust

TABLE 1

SUMMARY OF RESULTS

| Event ID | No. of Stations | $T$ (sec) | $C$ (min) | $T_M$ (min) | $\hat{m}_b$ | $M_w$ | $M_S$ |
|---|---|---|---|---|---|---|---|
| 0 Chile 1960 | 13 | 2.19 | 5.74 | 2.44 | 7.57 | 9.5 | 8.5 |
| 1 Alaska 1964 | 19 | 1.81 | 5.63 | 1.43 | 7.64 | 9.2 | 8.4 |
| 2 Rat Island 1965* | 17 | 1.48 | 5.08 | 0.77 | 7.19 | 8.7 | 8.2 |
| | | | | 2.31 | | | |
| 3 Kurile Island 1963 | 20 | 1.73 | 3.30 | 1.49 | 7.23 | 8.5 | 8.1 |
| 4 Sumbawa 1977 | 8 | 1.89 | 4.44 | 0.82 | 7.47 | 8.3 | 8.1 |
| 5 Tokachi-Oki 1968 | 27 | 1.56 | 3.96 | 1.35 | 7.18 | 8.2 | 8.1 |
| 6 Kurile Island 1969 | 9 | 1.67 | 3.39 | 0.70 | 6.90 | 8.2 | 7.8 |
| 7 Colombia 1979 | 16 | 1.67 | 3.72 | 1.09 | 6.91 | 8.2 | 7.7 |
| 8 Mindanao 1976 | 16 | 2.08 | 2.68 | 0.99 | 7.26 | 8.1 | 7.8 |
| 9 Peru 1974 | 17 | 1.94 | 3.06 | 0.58 | 7.00 | 8.1 | 7.6 |
| 10 Santa Cruz Island 1980 | 20 | 1.64 | 2.35 | 0.86 | 6.79 | 7.8 | 7.7 |
| 11 Oaxaca 1978 | 17 | 2.18 | 2.35 | 0.35 | 6.87 | 7.6 | 7.8 |
| 12 Petatlan 1979 | 18 | 1.81 | 2.37 | 0.32 | 6.71 | 7.6 | 7.6 |
| 13 Tangshan 1976 | 21 | 1.55 | 3.47 | 0.29 | 6.76 | 7.45 | 7.7 |
| 14 Guatemala 1976 | 17 | 1.56 | 3.88 | 0.89 | 6.66 | 7.5 | 7.5 |
| 15 Turkey 1976 | 17 | 1.78 | 2.06 | 0.22 | 6.58 | 7.2 | 7.3 |
| 16 Turkey 1967 | 22 | 1.51 | 2.06 | 0.21 | 6.38 | 7.4 | 7.1 |
| 17 San Fernando 1971 | 26 | 1.26 | 0.82 | 0.03 | 6.41 | 6.6 | 6.7 |
| 18 Imperial Valley 1979 | 19 | 1.60 | 1.75 | 0.30 | 5.92 | 6.5 | 6.5 |

* For the Rat Island 1965 earthquake, $T_M$ has a bimodal distribution: $T_M = 0.77 \pm 0.30$ and $T_M = 2.31 \pm 0.26$.

event. A comparison of $m_b$ and $M_S$ for about 50 earthquakes with $M_S$ of 5.0 to 7.5 indicates that for a given $M_S$, thrust earthquakes have $m_b$ about 1/4 units higher on the average than strike-slip earthquakes (Eissler and Kanamori, 1985).

The quality of the WWSSN records is very uneven. The standard deviations in $\hat{m}_b$ values are about 0.25, which is typical of most magnitude scales. The period, T, is the most difficult parameter to measure and, since the gain of the instrument depends on the period, uncertainty in T may account for some of the scatter in $\hat{m}_b$.

Figure 1.2 shows that unlike $m_b$, $\hat{m}_b$ does not appear to saturate completely with increasing $M_W$. For example, $m_b$ for the 1964 Alaskan earthquake is 6.4, while $\hat{m}_b$ is 7.6. A least-squares fit to the data shown in Figure 1.2 yields the following relationship between $\hat{m}_b$ and $M_W$:

$$\hat{m}_b = 0.53 \, M_W + 2.70 \tag{1.2}$$

in the range $M_W$=6.5 to $M_W$=9.5. Since $M_W$ is defined by

$$M_W = (\log M_0 - 16.1)/1.5 \, ,$$

(1.1) and (1.2) imply, assuming T is constant, that

$$A_g \ \alpha \ M_0^{0.35} \tag{1.3}$$

where $M_0$ is the seismic moment.

Figure 1.3a shows a general increase in coda length with increasing $M_W$. Intuitively, the coda length should be proportional to fault length. In Figure 1.3b, C is plotted against the rupture time (i.e., fault length, L, divided by rupture velocity, V). The coda length has a large scatter because of

Figure 1.2. $\hat{m}_b$ vs. $M_W$. The vertical bars show the standard deviations around the average $\hat{m}_b$ value. The number next to each data point refers to the event number in Table 1. The straight line was obtained by a least-squares fit to the data and follows equation (1.2). The black squares represent the results of the simulation procedure discussed in Section 1.4. The events simulated are #0, 1, 2, 3, and 5 in Table 1. The subevent is #17.
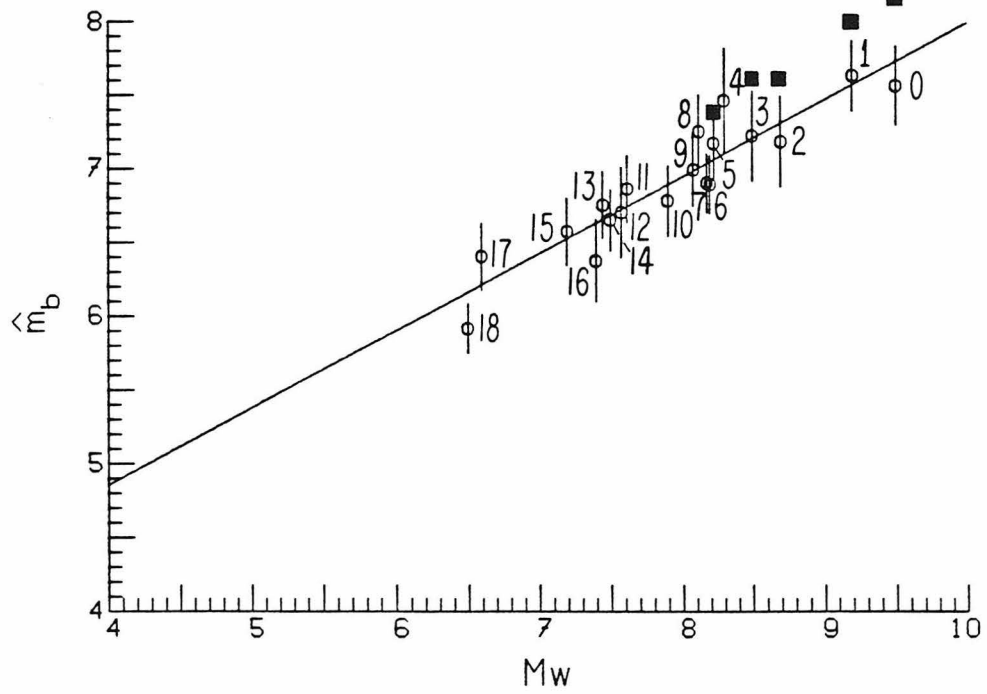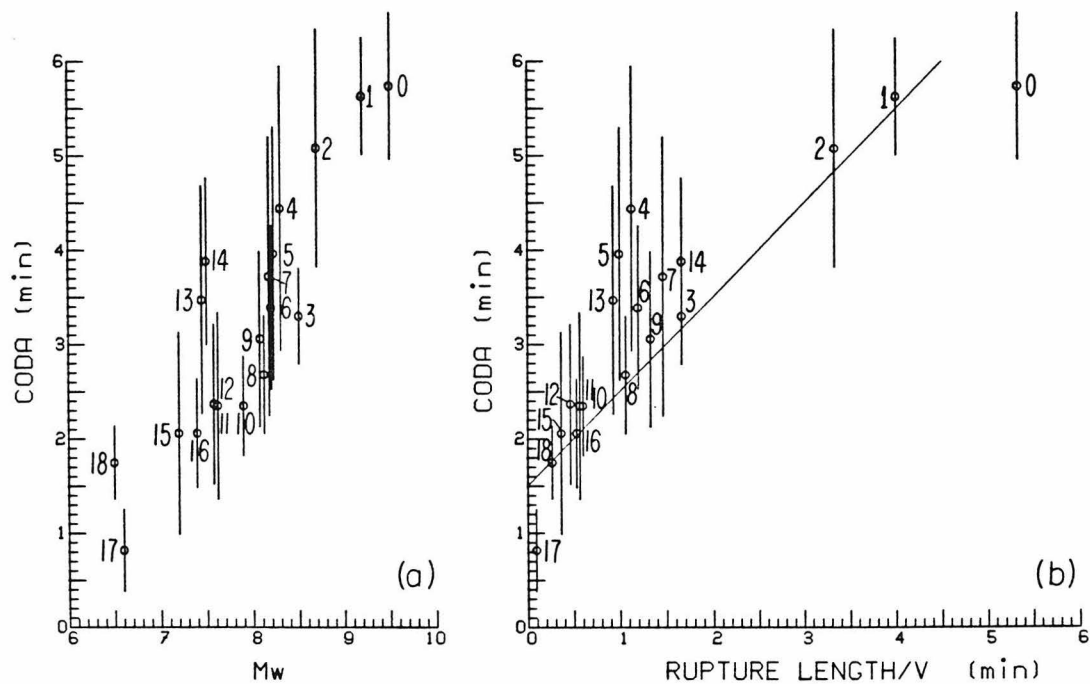
Figure 1.3. (a) Coda length vs. $M_W$. The vertical bars show the standard deviations around the average coda value. The number next to each data point refers to the event number in Table 1. (b) Coda length vs. rupture time. The reference line shows the relation: coda length = fault length/V + 1.5 minutes where V = rupture velocity = 2.5 km/sec (see text).

contamination by aftershocks, different receiver effects, and, occasionally, the arrival of the phase PP. Nevertheless, the data support the interpretation that the coda is roughly equal to the rupture time plus a constant time. The reference line in Figure 1.3b represents the relationship $C = L/V + 1.5$ minutes. We take $V = 2.5$ km/sec, which is typical of the rupture velocities summarized in Lay, Kanamori, and Ruff (1982). Fault plane dimensions are generally taken from Lay, Kanamori, and Ruff (1982). The extra 1 to 1.5 minutes is probably partly caused by scattering at the source and at the receiver. It may also result from the contaminating effects mentioned above, or from our particular definition of coda length.

In a general sense, the increase of $T_M$ with $M_W$ seen in Figure 1.4a can be explained if we view the occurrence of the maximum amplitude as a statistical event that is composed of arrivals from various parts of a uniformly rough fault plane. In this case, $T_M$ should increase linearly with the length and width of the fault, hence its increase with $M_W$. However, the deviation of $T_M$ from a steady increase with $M_W$ can be interpreted by considering the large-scale asperities (here defined as stronger regions with higher than average moment release per unit area). If asperities are important in releasing short-period energy, the distribution of moment release will interact statistically with random receiver or path effects to control $T_M$. On average, $T_M$ should be proportional to the distance between the hypocenter and the most significant asperity. Figure 1.4b shows measured $T_M$ with standard deviation bars, plotted against our estimate of the time between the initiation of rupture and the production of the maximum moment release per unit time. This quantity is estimated by adding the distance, D, from the hypocenter to the middle of the
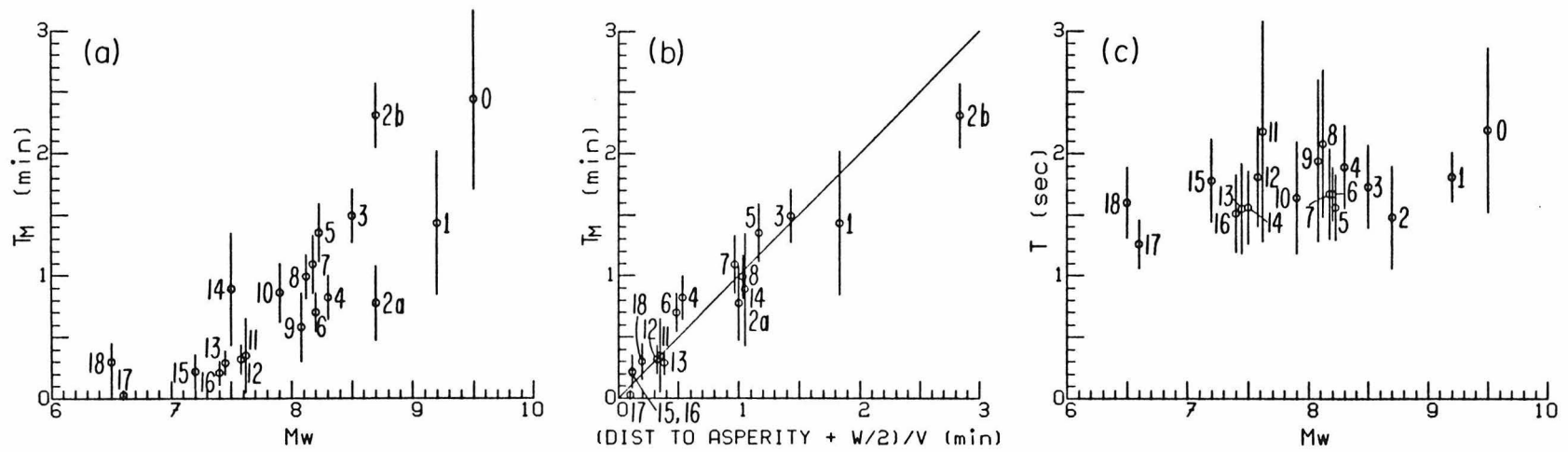
Figure 1.4. (a) Time from the beginning of the P wave until the maximum amplitude is achieved, $T_M$ vs. $M_W$. The vertical bars show the standard deviations in $T_M$. The number next to each data point refers to the event number in Table 1. (b) $T_M$ vs. time for rupture to propagate from hypocenter to largest asperity (see text). The reference line of slope 1 represents equation (1.4). (c) Period at maximum amplitude vs. $M_W$. The vertical lines show the standard deviations in the period.

largest asperity to half of the width of the fault plane, W, and dividing the sum by the rupture velocity, V:

$$\text{estimated } T_M \approx \frac{D + W/2}{V} \ . \tag{1.4}$$

Here we envision that after the rupture front arrives at a point, the slip motion there continues for $W/V$ seconds. Then $W/2V$ is half the duration of the slip motion. If the hypocenter is located within the largest asperity, then D is taken to be the radius of the asperity.

The positions of the asperities are inferred from studies in which long-period WWSSN records are deconvolved to yield the location in time and space of the areas on the fault plane that generate the most long-period radiation (with periods of 10 to 50 seconds). The moment release has been mapped by such methods for most of the earthquakes we are examining (Kikuchi, written comm. 1984; Beck and Ruff, 1984, 1985; Stewart and Kanamori, 1982; Kanamori and Stewart, 1978; Ruff and Kanamori, 1983; Hartzell and Heaton, 1983; Butler et al., 1979; Stewart and Cohn, 1979; Langston, 1978; Chael and Stewart, 1982).

For each earthquake, $T_M$ is an average; earthquake #2, Rat Island, 1965, possesses a markedly bimodal distribution of $T_M$ that is quite consistent with Kikuchi's and with Ruff and Kanamori's (1983) pattern of asperities. Both deconvolutions show two large asperities, one near the hypocenter and the other about 200 km to the west. Therefore, we separated the $T_M$'s for Rat Island, 1965, into two groups ($T_M$=0.77 ±0.31 minutes and $T_M$=2.31 ±0.26 minutes), and calculated two estimated $T_M$'s based on the distances to the two asperities. The results are plotted in Figure 1.4b as points 2a and 2b. The

generally good agreement in Figure 1.4b between the data and our estimate suggests that short-period radiation is on average generated preferentially in the same regions of the fault plane as longer-period radiation (with periods of 10 to 50 seconds).

The period at the maximum amplitude, T, is plotted against moment magnitude, $M_W$, in Figure 1.4c. T is longer than 0.7 seconds, the period of the peak in the WWSSN short-period response curve, because the instrument response is multiplied in the frequency domain by a source spectrum that decreases as period decreases. Figure 1.4c suggests that despite large scatter, T remains almost constant as $M_W$ increases. The two smallest earthquakes, San Fernando, 1971, and Imperial Valley, 1979, have shorter periods. It should be noted that T is usually about 0.4 seconds longer than the average period of the P wave (Boore, 1986).

## 1.3  Implications for Local Magnitude

Although it is known (Brune, 1970; Kanamori, 1979) that local magnitude, $M_L$, appears to saturate for California strike-slip events at about 7 1/4, the behavior of $M_L$ is not known for great thrust earthquakes. Since $\hat{m}_b$ and $M_L$ represent the amplitude of seismic waves at about the same period, the behavior of $M_L$ for great earthquakes may be similar to $\hat{m}_b$. However, the rupture plane-site geometry may be an important factor. Since $\hat{m}_b$ is determined at teleseismic distances, seismic radiation from the entire fault plane contributes to $\hat{m}_b$ equally. In contrast, $M_L$, which is determined in the near-field, weights the closest part of the fault plane more heavily. Hence, it is possible

that $M_L$ for great thrust earthquakes saturates as $M_W$ increases, even though $\hat{m}_b$ does not.

## 1.4 Application to Strong Motion Prediction

In this section we illustrate how our teleseismic data can constrain strong motion modeling of great earthquakes. Kanamori (1979) simulated the rupture of a one-dimensional strike-slip fault. Here we extend his approach to a two-dimensional, dipping fault plane. The fault plane is divided into subfaults and empirical Green's functions (or subevents) are superimposed with some randomness. The technique of superposition of Green's functions has been used by many workers and can be implemented in different ways. Our procedure adheres to two principles: 1) it is consistent with gross seismological parameters of the event to be simulated and the subevent, such as total moment, fault dimensions, and presence of large scale asperities, and 2) it incorporates randomness in several different ways.

In our procedure the displacement at the site can be expressed as

$$d(t) = \sum_{i=1}^{I} \sum_{j=1}^{J} f_{ij}(t - \eta_{ij}) \qquad (1.5)$$

where $f_{ij}(t)$ is the displacement at the site due to the $ij^{th}$ point source, t is time, I and J are the number of subfaults into which the two-dimensional fault plane is divided in length and width, and $\eta_{ij}$ is the delay applied to the ij-th subfault to simulate rupture propagation. To make the procedure physically realistic, we chose I and J so that the length and width of the subfault are equal to the length and width of the subevent rupture. $\eta_{ij}$ is calculated by dividing the

distance from the hypocenter to the ij-th subfault by a rupture velocity chosen from a random Gaussian distribution. The rupture front is thus roughly circular.

In using this method we neglect the effects of radiation pattern and dispersion and assume that attenuation and geometrical spreading can be approximated by a power law decay in amplitude with distance. With these assumptions, $f_{ij}(t)$ can be written

$$f_{ij}(t) = \left[ \frac{\Delta_0}{\Delta_{ij}} \right]^p g_{ij}(t - \frac{1}{c}\Delta_{ij}) \tag{1.6}$$

where $g_{ij}(t)$ is the displacement at the site due to the ij-th subfault at distance $\Delta_0$, the distance at which the subevent record was written, $\Delta_{ij}$ is the distance between the ij-th subfault and the site, p is the power of the attenuation, and c is the phase velocity (assumed to be 6.0 km/sec for the teleseismic calculation and 3.0 km/sec for the near-field calculation). $\Delta_{ij}$ is calculated from the 3-dimensional relationship of the dipping fault plane to the site.

It remains to obtain $g_{ij}$ by summing subevent records:

$$g_{ij}(t) = m_{ij} \sum_{k=1}^{n_{ij}} g_0(t - \tau_{ijk}) \tag{1.7}$$

where $g_0(t)$ is the subevent record, $\tau_{ijk}$ is a time delay, $n_{ij}$ is determined from the strength of the subfault, and $m_{ij}$ is a factor near 1 chosen so that an integral number of subevent records, $n_{ij}$, can sum to a desired subfault moment. That is, $n_{ij} = [M_{ij}/m_0]$ and $m_{ij} = M_{ij}/(n_{ij} m_0)$ where $M_{ij}$ is the moment assigned to each subfault, $m_0$ is the moment of the subevent, and [ ] means nearest integer to the argument. In our implementation $M_{ij}$ can be drawn

from one of two Gaussian distributions, of which one represents weak zones and the other stronger zones (asperities). We specify the average values and the standard deviations of the Gaussian distributions so that the total moment of the subevents sums to the moment, $M_0$, of the event to be simulated. That is, $<M_{ij}> = M_0/IJ$ where $< >$ means the average value of the argument. $\tau_{ijk}$ in (1.7) is randomly drawn from a uniform distribution between 0 and $n_{ij}\tau$ where $\tau$ is a somewhat arbitrary time; we chose $\tau$ to be roughly the effective width of the time function of the subevent. The calculation is not sensitive to $\tau$. As discussed in Kanamori (1979), randomly picking $\tau_{ijk}$ is a middle course between the two extremes of summing all the subevent records at once (e.g., $g_{ij}(t)=m_{ij}n_{ij}g_0(t)$) and delaying each subevent record by a uniform time (e.g., $g_{ij}(t)=m_{ij}\sum_{k=1}^{n_{ij}} g_0(t-k\tau)$). Using the first scheme increases the maximum amplitude of simulated ground motions produced by a long strike-slip rupture by a factor of 4 compared to the second scheme (see Figure 7 of Kanamori, 1979). The middle course of picking $\tau_{ijk}$ randomly produces amplitudes half as large as the first and twice as large as the second scheme.

To make this calculation we must choose an appropriate subevent and a typical subevent record to serve as $g_0(t)$. We chose the 1971 San Fernando earthquake (#17 in Table 1; $M_W = 6.6$) because it was a thrust event that was well-recorded in both the near- and far-field. For the San Fernando earthquake, we chose $\tau$ to be 2 seconds (Langston, 1978). We used the Matsushiro, Japan, short-period WWSSN record ($\Delta_0 = 80°$) as $g_0(t)$. We simulated five great subduction earthquakes (1960 Chile, 1964 Alaska, 1965 Rat Is., 1963 Kurile Is., and 1968 Tokachi-Oki), using the summation procedure outlined

above. The dip of the fault plane was assumed to be 30°. We chose a rupture velocity of 2.5 km/sec with a standard deviation of 0.3 km/sec. Attenuation was not included in the teleseismic simulations (eg. $\Delta_{ij} \approx \Delta_0$ or, equivalently, p=0 in (1.6)). Therefore the simulated WWSSN records must be considered to be at the same distance as $g_0(t)$. For simplicity, we took all $M_{ij}$'s to be equal. Examples of the observed and simulated traces are shown in Figure 1.5. For each earthquake, an average $\hat{m}_b$ is calculated from 5 or more simulations with different random seeds. The resulting simulated $\hat{m}_b$'s are shown as black squares in Figure 1.2. The simulated $\hat{m}_b$'s are about 0.3 $\hat{m}_b$ units larger than the observed $\hat{m}_b$'s (except for the 1960 Chilean earthquake). Considering that the difference in moment between the subevent and the event to be simulated is three to four orders of magnitude, the agreement between the observed and the simulated $\hat{m}_b$'s is good. The entire fault plane was assumed to have uniform strength in the teleseismic simulations. Including large-scale asperities increased the displacement amplitudes only about 20% (Houston and Kanamori, 1984).

This simulation procedure can be applied to predict the amplitude and duration of strong-ground motion given the rupture plane and moment of an earthquake by choosing for $g_0(t)$ a near-field strong motion record. Coats, Kanamori, and Houston (1984) used the method described above to simulate the near-field motions at Anchorage, Alaska caused by the 1964 Alaska earthquake. As various $g_0(t)$'s, Coats et al. (1984) used three 1971 San Fernando strong-motion records written at distances of 40 km to 110 km: H121, N191, and O206 (Hudson et al., 1969). The dip of the fault plane was prescribed to be 15°. The calculations assumed an average rupture velocity of 3.0 km/sec

SAN FERNANDO Feb.4,1971 $M_o = 1\times10^{26}$
MAT $\Delta = 79.7°$ × 100000

0.63 $\mu$ ×17

1 Green's function

14 km × 20 km

TOKACHI OKI May 16,1968 $M_o = 2.8\times10^{28}$
BKS $\Delta = 69.3°$ ×25000

4.9 $\mu$

5.5 $\mu$

280 Green's functions

150 km × 100 km

KURILE IS. Oct. 13, 1963 $M_o = 7.5\times10^{28}$
STU $\Delta = 80.5°$ ×25000

5.6 $\mu$

7.0 $\mu$

750 Green's functions

250 km × 150 km

RAT ISLAND Feb. 4, 1965 $M_o = 1.4\times10^{29}$
ESK $\Delta = 73.7°$ ×12500

3.3 $\mu$

7.0 $\mu$

1400 Green's functions

500 km × 150 km

ALASKA Mar. 28, 1964 $M_o = 7.5\times10^{29}$
BOG $\Delta = 78.0°$ ×12500

13.1 $\mu$

16.6 $\mu$

7500 Green's functions

500 km × 300 km

CHILE May 22, 1960 $M_o = 2.7\times10^{30}$
PLM $\Delta = 82.2°$ ×30000

19.8 $\mu$

26.3 $\mu$

27000 Green's functions

800 km × 200km

Figure 1.5. A comparison between actual records and the simulated records for five great earthquakes. Length and width of the fault plane and the number of subevent records summed are given on the right. Minute marks are visible on the WWSSN and Benioff records. Distances and gains are given for the WWSSN and Benioff records. The amplitude of the ground motion in microns is shown next to each trace. The record from WWSSN station MAT of the 1971 San Fernando earthquake has been digitized and serves as the subevent record. It is shown both to scale and expanded 17 times for ease of viewing. All simulated traces represent teleseismic records at a distance of 80°, which is the distance from San Fernando to the station MAT. Note the similarity in duration and time to the maximum amplitude between the simulated and actual records for each event.

with a standard deviation of 0.3 km/sec. They included the large asperity determined from deconvolutions of long-period body waves (Ruff and Kanamori, 1983); subfaults within the asperity were assumed to release about twice as much moment as subfaults in the weak zone. Using uniform moment release decreased the velocities at the site by a factor of about 1.3 over those produced by the fault plane containing the asperity. This factor would increase if the asperity were assumed to be stronger. Both amplitude and duration of the strong motion were somewhat sensitive to the degree of attenuation that was assumed. The power, p, in (1.6) is prescribed to be 1.7. Coats et al. (1984) computed $M_L$'s of 7.4 to 7.8 and peak-to-peak displacements at the site averaging 35 cm. The duration of significant motion exceeded 3 minutes. It is not clear whether the $M_L$'s should be adjusted down by the amount that the simulated $\hat{m}_b$ for 1964 Alaska is too high. Ultimately, small earthquakes from a given seismogenic zone recorded at the site under consideration can be used as subevents, thus reducing the considerable uncertainty caused by propagation and site effects.

The success of a summation scheme depends on the way in which the subevent records are superposed (see, for example, Joyner and Boore, 1986). This can be understood in the frequency domain as a requirement that the summation procedure take the spectrum of the subevent to an appropriate spectrum for the earthquake to be simulated. The discrepancy between the actual and simulated $\hat{m}_b$ seen in Figure 1.2 could be due to the choice of a very impulsive, high stress-drop earthquake to serve as the subevent. In an essentially similar approach, strong motions can be modeled in the frequency domain directly (e.g., Boore, 1983) if the source spectrum of the event to be

simulated can be assumed (for example, the source spectra determined in Chapter 2 could be used). Such modeling should be consistent with the teleseismic data presented above.

## 1.5   Conclusions

A new teleseismic body-wave magnitude, $\hat{m}_b$, is defined using the maximum amplitude of the P wave rather than the amplitude in the first few cycles of the P wave. Analysis of WWSSN short-period teleseismic records of 19 large to great earthquakes shows that $\hat{m}_b$ does not saturate with increasing $M_W$. The empirical relation between $\hat{m}_b$ and $M_W$ is given by (1.2). We chose to further parameterize the complex short-period waveform by the coda length and the build-up time to the maximum amplitude. These data are consistent with a simple model of rupture propagating at a velocity of 2.5 km/sec across a fault plane with asperities. Figure 1.4b confirms that short-period waves are generated preferentially in the same regions of the fault plane as longer-period waves with periods of 10 to 50 seconds, and to some extent supports the mapping of moment release on the fault plane performed by other workers by deconvolutions of long-period waves.

An application to strong motion modeling is presented in which a 1971 San Fernando teleseismic short-period record is summed up to simulate teleseismic records produced by five great earthquakes. The summation procedure matches the moment of the event to be simulated, and includes rupture propagation, fault plane roughness, and randomness. The $\hat{m}_b$ data constrains the summation procedure at periods of 1 to 2 seconds. The simulated $\hat{m}_b$'s are

about 0.3 $\hat{m}_b$ units larger than the observed $\hat{m}_b$'s (except for the 1960 Chilean earthquake). Considering that the difference in moment between the subevent and the event to be simulated is three to four orders of magnitude, the agreement between the observed and the simulated $\hat{m}_b$'s is good. This method can also be evaluated in the frequency domain using the source spectra that we will determine from digital records in Chapter 2. Thus constrained at short periods by teleseismic data, this summation procedure can be more confidently used with near-field strong motion records as Green's functions to predict strong motions from great earthquakes.

## 1.6 References

Beck, S., and L. Ruff, The rupture process of the great 1979 Colombia earthquake: evidence for the asperity model, *J. Geophys. Res., 89,* 9281-9291, 1984.

Boore, D. M., Stochastic simulation of high-frequency ground motions based on seismological models of the radiated spectra, *Bull. Seism. Soc. Am., 54,* 1865-1894, 1983.

Boore, D., Short-period P-wave radiation from large earthquakes: implications for spectral scaling laws, *Bull. Seism. Soc. Am., 76,* 43-64, 1986.

Brune, J., Tectonic stress and the spectra of seismic shear waves from earthquakes, *J. Geophys. Res., 75,* 4997-5009, 1970.

Butler, R., G. S. Stewart and H. Kanamori, The July 27, 1976 Tangshan, China earthquake - a complex sequence of intraplate events, *Bull. Seism. Soc. Am., 69,* 207-220, 1979.

Chael, E., and G. Stewart, Recent large earthquakes along the Middle American Trench and their implications for the subduction process, *J. Geophys. Res., 87,* 329-338, 1982.

Coats, D., H. Kanamori, and H. Houston, Simulation of the strong motion

from the 1964 Alaskan earthquake (abs.), *Earthquake Notes, 55*, 18, 1984.

Eissler, H. K., and H. Kanamori, Depth estimates of large earthquakes on the island of Hawaii since 1940, *J. Geophys. Res., 91*, 2063-2076, 1985.

Hartzell, S. H., and T. Heaton, Inversion of strong ground motion and teleseismic waveform data for the fault rupture history of the 1979 Imperial Valley, California, earthquake, *Bull. Seism. Soc. Am., 73*, 1553-1583, 1983.

Houston, H., and H. Kanamori, Rupture process of great earthquakes at short periods (abs.), *EOS*, (Trans. Am. Geophys. Un.) *64*, 771, 1983.

Houston, H., and H. Kanamori, The effect of asperities on short-period seismic radiation with application to the 1964 Alaskan earthquake (abstract), *Earthquake Notes, 55*, 990, 1984.

Hudson, D.E., M.D. Trifunac, and A.G. Brady, Analysis of strong motion accelerograms, Index vol. (EERL Report No. 76-02), Earthquake Engineering Research Laboratory, California Institute of Technology, Pasadena, California, 1969.

Joyner, W. B., and D. M. Boore, On simulating large earthquakes by Green's function addition of smaller earthquakes, *Proceedings of the* 5th Maurice Ewing Symposium on Earthquake Source Mechanics, AGU, 269-274, 1986.

Kanamori, H., A semi-empirical approach to prediction of long period ground motions from great earthquakes, *Bull. Seism. Soc. Am., 69*, 1645-1670, 1979.

Kanamori, H., and G. Stewart, Seismological aspects of the Guatamala earthquake of February 4, 1976, *J. Geophys. Res., 83*, 3427-3434, 1978.

Koyama, J., and S. Zheng, Excitation of short-period body waves by recent great earthquakes, ZISIN, *J. Seis. Soc. Japan, 36*, 237-245, 1983 (in Japanese w/ English abstract).

Koyama, J., and S. Zheng, Excitation of short-period body waves by recent great earthquakes, *Phys. Earth Planet. Inter., 37*, 108-123, 1985.

Langston, C. A., The February 9, 1971 San Fernando earthquake: a study of source finiteness in teleseismic body waves, *Bull. Seism. Soc. Am., 68*, 1-29, 1978.

Lay, T., H. Kanamori, and L. Ruff, The asperity model and the nature of large subduction zone earthquakes, *Earthquake Prediction Research, 1*, 3-71, 1982.

Purcaru, G., Rupture process pattern of earthquakes from frequency-time-dependent body-wave magnitudes $m_B(t,T)$ and a subasperity model, (abs.), *IASPEI*, Regional Meeting, abstract volume, Hyderabad, India, Oct. 31 - Nov. 7, 19, 1984.

Ruff, L., and H. Kanamori, The rupture process and asperity distribution of three great earthquakes from long-period diffracted P waves, *Phys. Earth Planet. Inter., 31*, 202-330, 1983.

Stewart, G., and S. N. Cohn, The 1976 August 16, Mindanao Phillipine earthquake ($M_S$=7.8) - evidence for a subduction zone south of Mindanao, *Geophys. J. R. Astr. Soc., 57*, 51-65, 1979.

Stewart, G. S. and H. Kanamori, Complexity of rupture in large strike-slip earthquakes in Turkey, *Phys. Earth Planet. Inter., 28*, 70-84, 1982.

# Chapter 2

# The Teleseismic Source Spectrum

## Abstract

We analyze the spectra of short- and intermediate-period teleseismic GDSN records for 7 earthquakes with $M_W$'s of 6.4 to 7.8 and hand-digitized short-period WWSSN records of the 1971 San Fernando earthquake. Significant differences exist between the spectra of different events, due partly to variations in tectonic setting or seismic coupling. Using the digital data, we also investigate the relationship between time-domain amplitude and spectral amplitude for short-period P-waves. From our empirical relation between spectral amplitude and time-domain amplitude, we estimate the spectral amplitudes implied by the $\hat{m}_b$ data presented in Chapter 1. We compare our results to the $\omega^{-2}$ and Gusev spectral models. Neither model can completely represent the data. Nevertheless, we consider the $\omega^{-2}$ model a useful reference model for comparing different events. The average source spectrum of 6 large events with $M_W$ 7.4 to 7.8 does not have the spectral structure suggested by Gusev.

## 2.1 Introduction

Several theoretical studies have been made to relate the seismic source spectrum to rupture processes (Haskell, 1964, 1966; Aki, 1967; Brune, 1970). Also, many investigators have estimated the source spectrum empirically (e.g., Aki, 1972, 1983; Gusev 1983). Various spectral models have been proposed, both theoretically and empirically. Important differences exist between these models. Previous empirical approaches to obtaining source spectra have been indirect, often deduced from comparisons of $m_b$, $M_S$, and other magnitude scales. Since $m_b$ is a measurement at one period, and since it is determined from the first few cycles of the P-wave train only, it does not always represent the source spectrum correctly.

In the past few years, high-quality broadband digital data have become available from Global Digital Seismic Network (GDSN). Since the nature of the source spectrum is important to understand the earthquake rupture process and for empirical prediction of strong ground motion (as in Boore, 1983), we investigate this problem by analyzing these records.

We analyze GDSN records for 7 earthquakes of magnitude 6.4 to 7.8. The digital data are Fourier transformed. The resulting displacement spectra are corrected for instrument response, attenuation, geometrical spreading, and radiation pattern, and then averaged to determine the source spectra from 1 to 30 seconds. Using digitally-recorded or hand-digitized records, we also estimate empirically the relationship between time-domain amplitude and spectral amplitude for short-period P-waves. This enables us to estimate spectral amplitudes at about 2 sec from $\hat{m}_b$ determined in Chapter 1. Combining those

spectral amplitudes with the directly determined spectra, we determine source spectra for earthquakes with $M_W= 6.4$ to $9.5$. We discuss the implications of these data for source spectral models.

## 2.2 Spectral Analysis of Broadband Data

We study seven earthquakes recorded by GDSN including five large subduction-zone thrust events (1983 Akita-Oki, 1980 Santa Cruz Is., 1983 North Chile, 1982 Tonga Is., 1983 Costa Rica), a normal-faulting event (1983 Chagos Ridge), and a California thrust event (1983 Coalinga). We also analyze teleseismic hand-digitized WWSSN records of the 1971 San Fernando earthquake used by Langston (1978). The events and the stations used for each event are listed in Table 1.

We analyzed both intermediate-period records from DWWSSN and RSTN stations, and short-period records from DWWSSN, SRO, and ASRO stations. The short-period DWWSSN, SRO, and ASRO instrument responses peak between 0.5 and 0.7 seconds and fall off about as $\omega^{-2}$ between 1 Hz and 0.1 Hz (1 and 10 seconds). The broadband intermediate-period DWWSSN and RSTN responses peak at 1 second, but fall off only as $\omega^{-1}$ between 1 Hz and 0.1 Hz. A total of 91 records is used. We use only unclipped or slightly clipped records.

For the well-recorded Akita-Oki event, excellent coherence is observed from station to station, and between the intermediate- and short-period records at a given station. Figure 2.1 shows some of these records. We window, taper, and Fourier transform the P-wave train. The window length is

TABLE **1**

RECORDS USED IN SPECTRAL ANALYSIS

| Station | Type | $\Delta$ (°) | Azimuth (°) | $R_{\theta\phi}$ | C |
|---|---|---|---|---|---|
| Akita-Oki, Japan 26 May 1983 $M_u = 7.8$ | | | | | subduction thrust |
| CTAO | SP ASRO | 60.7 | 172.3 | 0.80 | 1.79 |
| KONO | SP ASRO | 71.9 | 335.7 | 0.86 | 1.84 |
| COL | IP DWWSSN | 47.2 | 33.7 | 1.41 | 1.73 |
| LON | IP DWWSSN | 67.2 | 47.3 | 1.44 | 1.81 |
| HON | IP DWWSSN | 56.0 | 89.8 | 1.64 | 1.76 |
| KEV | IP DWWSSN | 59.6 | 338.1 | 0.81 | 1.79 |
| AFI | IP DWWSSN | 70.7 | 128.8 | 1.17 | 1.83 |
| BER | IP DWWSSN | 72.6 | 338.0 | 0.87 | 1.84 |
| TAU | IP DWWSSN | 83.4 | 173.9 | 0.93 | 1.88 |
| RSNT | IP RSTN | 62.7 | 30.3 | 1.31 | 1.80 |
| RSSD | IP RSTN | 78.4 | 40.9 | 1.30 | 1.87 |
| RSNY | IP RSTN | 90.0 | 23.3 | 1.16 | 1.90 |
| RSON | IP RSTN | 77.9 | 31.0 | 1.24 | 1.87 |
| Santa Cruz Islands 17 July 1980 $M_u = 7.8$ | | | | | subduction thrust |
| CHTO | SP SRO | 73.0 | 294.2 | 0.98 | 1.84 |
| NWAO | SP SRO | 48.8 | 237.1 | 0.78 | 1.73 |
| TATO | SP SRO | 57.2 | 310.8 | 0.91 | 1.77 |
| MAJO | SP ASRO | 55.4 | 332.9 | 0.98 | 1.76 |
| SNZO | SP SRO | 29.8 | 166.5 | 0.93 | 1.63 |
| GUMO | SP SRO | 33.3 | 320.4 | 0.82 | 1.65 |
| Chagos Ridge, Indian Ocean 30 November 1983 $M_u = 7.7$ | | | | | Normal |
| GUMO | SP SRO | 75.0 | 74.0 | 0.84 | 1.85 |
| NWAO | SP SRO | 49.2 | 128.1 | 0.76 | 1.73 |
| KONO | SP ASRO | 82.6 | 332.9 | 1.32 | 1.88 |
| KEV | IP DWWSSN | 82.5 | 345.6 | 1.29 | 1.88 |
| SLR | IP DWWSSN | 45.8 | 240.6 | 0.86 | 1.71 |
| TAU | IP DWWSSN | 74.5 | 132.5 | 0.93 | 1.85 |
| North Chile 4 October 1983 $M_u = 7.6$ | | | | | subduction thrust |
| SCP | IP DWWSSN | 67.6 | 354.2 | 0.77 | 1.82 |
| LON | IP DWWSSN | 86.5 | 327.5 | 0.72 | 1.89 |
| SLR | IP DWWSSN | 86.2 | 116.9 | 1.19 | 1.89 |
| TOL | IP DWWSSN | 90.8 | 45.1 | 1.23 | 1.91 |
| ANMO | SP SRO | 70.0 | 329.3 | 0.62 | 1.83 |
| SNZO | SP SRO | 89.1 | 223.2 | 0.96 | 1.90 |
| JAS | SP DWWSSN | 79.4 | 322.1 | 0.70 | 1.87 |
| Tonga-Kermadec Trench 19 December 1982 $M_u = 7.5$ | | | | | subduction thrust |
| COL | SP DWWSSN | 91.5 | 11.6 | 0.84 | 1.91 |
| LON | SP DWWSSN | 85.9 | 34.0 | 0.85 | 1.89 |
| JAS | SP DWWSSN | 80.8 | 41.3 | 0.86 | 1.87 |
| TAU | SP DWWSSN | 35.6 | 229.2 | 1.49 | 1.66 |
| ANMO | SP SRO | 88.2 | 50.4 | 0.92 | 1.90 |
| CTAO | SP ASRO | 35.3 | 269.0 | 1.97 | 1.66 |
| Costa Rica 3 April 1983 $M_u = 7.4$ | | | | | subduction thrust |
| SCP | IP DWWSSN | 32.3 | 7.5 | 1.92 | 1.64 |
| COL | IP DWWSSN | 71.5 | 336.0 | 1.35 | 1.84 |

TABLE *1—Continued*

| LON | IP DWWSSN | 50.2 | 326.0 | 1.35 | 1.74 |
|---|---|---|---|---|---|
| TOL | IP DWWSSN | 76.0 | 51.1 | 1.33 | 1.86 |
| BER | IP DWWSSN | 81.7 | 30.1 | 1.42 | 1.88 |
| ANMO | SP SRO | 33.6 | 324.1 | 1.39 | 1.65 |
| GRFO | SP SRO | 86.2 | 40.4 | 1.32 | 1.89 |
| ZOBO | SP ASRO | 29.0 | 149.1 | 0.54 | 1.62 |
| KONO | SP ASRO | 83.9 | 30.7 | 1.39 | 1.89 |
| HON | SP DWWSSN | 72.8 | 289.6 | 0.87 | 1.84 |
| KEV | SP DWWSSN | 88.6 | 19.1 | 1.37 | 1.90 |
| AFI | SP DWWSSN | 90.1 | 256.2 | 0.86 | 1.91 |
| RSCP | IP RSTN | 26.9 | 355.6 | 1.86 | 1.61 |
| RSSD | IP RSTN | 39.7 | 336.3 | 1.56 | 1.68 |
| RSNY | IP RSTN | 36.5 | 10.4 | 1.91 | 1.66 |
| RSON | IP RSTN | 43.0 | 350.2 | 1.72 | 1.70 |

| Coalinga 2 May 1983 | | | | | intraplate |
| $M_u = 6.4$ | | | | | thrust |
|---|---|---|---|---|---|
| ZOBO | SP ASRO | 71.9 | 126.9 | 0.91 | 1.84 |
| MAJO | SP ASRO | 77.2 | 306.1 | 1.40 | 1.86 |
| KONO | SP ASRO | 75.7 | 23.6 | 0.98 | 1.85 |
| SCP | SP DWWSSN | 33.2 | 70.0 | 0.54 | 1.64 |
| HON | SP DWWSSN | 40.0 | 256.1 | 1.14 | 1.68 |
| KEV | SP DWWSSN | 71.5 | 11.4 | 1.14 | 1.84 |
| AFI | SP DWWSSN | 69.7 | 234.3 | 0.88 | 1.83 |
| COL | IP DWWSSN | 33.0 | 338.8 | 1.79 | 1.64 |

| San Fernando 9 February 1971 | | | | | intraplate |
| $M_u = 6.6$ | | | | | thrust |
|---|---|---|---|---|---|
| BLA | SP WWSSN | 30.8 | 73.7 | 0.92 | 1.63 |
| AFI | SP WWSSN | 69.9 | 236.1 | 1.10 | 1.83 |
| MAT | SP WWSSN | 79.7 | 307.2 | 1.07 | 1.87 |
| KEV | SP WWSSN | 73.1 | 11.9 | 0.89 | 1.84 |
| NUR | SP WWSSN | 80.7 | 17.6 | 0.96 | 1.87 |
| KTG | SP WWSSN | 60.1 | 22.7 | 0.79 | 1.79 |
| PTO | SP WWSSN | 80.9 | 46.0 | 0.99 | 1.88 |
| OGD | SP WWSSN | 34.9 | 65.9 | 0.89 | 1.65 |
| GIE | SP WWSSN | 42.5 | 135.9 | 1.27 | 1.70 |
| PEL | SP WWSSN | 80.7 | 141.6 | 1.26 | 1.87 |
| KIP | SP WWSSN | 37.1 | 260.2 | 0.90 | 1.67 |
| NAT | SP WWSSN | 87.2 | 98.5 | 1.18 | 1.90 |
| BHP | SP WWSSN | 43.6 | 116.2 | 1.17 | 1.70 |
| ARE | SP WWSSN | 67.4 | 130.7 | 1.23 | 1.82 |
| HNR | SP WWSSN | 88.5 | 257.6 | 1.12 | 1.90 |
| ALE | SP WWSSN | 51.8 | 8.0 | 0.72 | 1.75 |
| AQU | SP WWSSN | 91.8 | 33.6 | 1.06 | 1.91 |
| ATL | SP WWSSN | 28.2 | 82.3 | 0.96 | 1.62 |
| CUM | SP WWSSN | 54.4 | 102.2 | 1.11 | 1.76 |
| ESK | SP WWSSN | 74.9 | 32.4 | 0.92 | 1.85 |
| GDH | SP WWSSN | 49.4 | 25.1 | 0.75 | 1.73 |
| KON | SP WWSSN | 76.9 | 24.3 | 0.93 | 1.86 |
| STU | SP WWSSN | 85.0 | 31.7 | 1.00 | 1.89 |
| TRI | SP WWSSN | 89.3 | 31.4 | 1.04 | 1.90 |
| FBC | SP WWSSN | 42.2 | 30.4 | .76 | 1.69 |
| SCH | SP WWSSN | 40.9 | 43.8 | 0.80 | 1.69 |
| STJ | SP WWSSN | 49.8 | 53.8 | 0.85 | 1.74 |
| FCC | SP WWSSN | 29.2 | 26.0 | 0.77 | 1.62 |
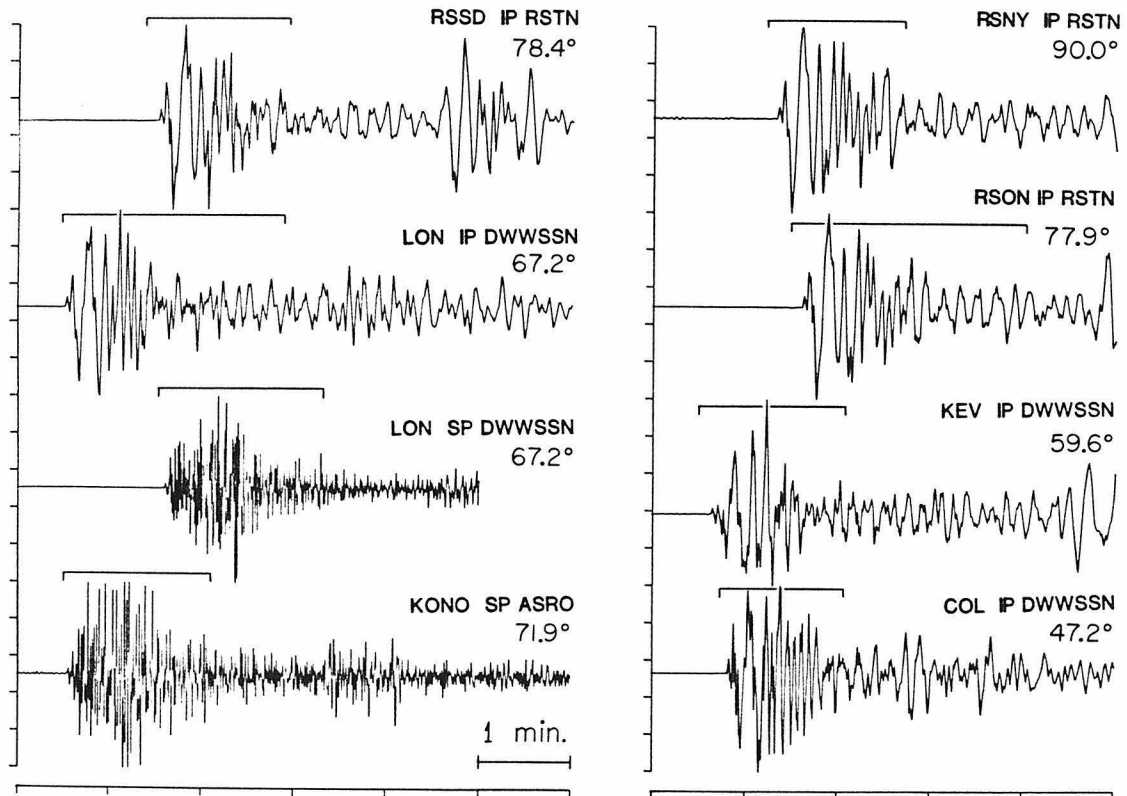
Figure 2.1. Examples of digital intermediate- and short-period seismograms from the GDSN Network for the 1983 Akita-Oki earthquake. For each record, instrument type and distance are given. Brackets show the portion of the P wave that is windowed and Fourier transformed.

given by the coda length as defined in our analysis of WWSSN records above. Typical coda lengths are 1 to 3 minutes.

After removing the appropriate instrument response from the spectra, we correct for attenuation with a constant $t^* = 0.7$ sec where $t^*$ is the P-wave attenuation parameter defined by $t^* = \int_s ds/Q(s)\, \alpha(s)$. Here $Q(s)$ and $\alpha(s)$ are the quality factor and the P-wave velocity along the ray path s, and the integral is taken along s.

Admittedly, $t^*$ depends on station distance (Kanamori, 1967), frequency (Der and Lees, 1984), and tectonic province (Der and Lees, 1984). However, in the interest of simplicity and because the detailed behavior of $t^*$ is not well known for all the source-station paths used in this study, we chose a constant $t^*$. The effect of using Der and Lees' (1984) QPST model for $t^*$ compared to using a constant $t^*=0.7$ sec is to lower the spectral amplitude at the source by a factor of 1.1 at 2 seconds and a factor of 1.6 at 1 second. Spectral amplitudes are not significantly affected at periods longer than 2 seconds.

Another frequency-dependent effect is the amplification of waves as they travel toward the surface through material of decreasing velocity. This effect is discussed by Boore (1986) and Gusev (1983). It tends to amplify short-period waves more than long period waves, and, therefore, operates in the same direction as Der and Lees' (1984) frequency-dependent $t^*$. Boore (1986) estimates that the near-surface amplification effect will increase 1-second amplitudes by a factor of 1.32 more than 10-second amplitudes. Gusev (1983) finds this factor to be 1.78. 10-second energy is amplified by a factor of only 1.10 according to Boore (1986) and not at all according to Gusev (1983). Since

it depends on the station site, we chose to ignore it. Because of the neglect of the frequency dependence of t* and the near-surface amplification effect, spectral amplitudes at 1 second could be slightly uncertain. However, our estimate of the spectral amplitudes at periods longer than 2 seconds is considered reliable.

Each spectrum is further corrected for distance (geometrical spreading), radiation pattern, and free-surface receiver effect. Then, for each earthquake, 6 to 16 corrected spectra are averaged together in a logarithmic sense (that is, we average the logarithm of the spectral amplitude). We thus obtain the average moment rate spectrum, or equivalently, moment rate spectral density, $\hat{M}(\omega)$, for each earthquake according to:

$$\hat{M}(\omega) = \frac{4\pi\rho\alpha^3 R_E}{g(\Delta)R_{\theta\phi}C} \left[ \frac{e^{\frac{\omega t^*}{2}}}{\hat{I}(\omega)} \hat{u}(\omega) \right] \tag{2.1}$$

where $\rho$ and $\alpha$ are the density and P-wave velocity at the source, $R_E$ is the radius of the earth, $g(\Delta)$ represents geometrical spreading, $R_{\theta\phi}$ is the effective radiation pattern of the P-wave train that includes the P, pP, and sP phases, C is the free-surface receiver effect, t* represents attenuation, $\hat{I}(\omega)$ is the instrument response, and $\hat{u}(\omega)$ is the observed displacement spectrum. The symbol '^' in (2.1) denotes a Fourier transformed quantity.

In all these events the crust is involved in faulting. Hence, we take $\rho = 2.8$ gm/cm$^3$ and $\alpha = 6.5$ km/sec for the larger events, and $\rho = 2.65$ gm/cm$^3$ and $\alpha = 6.1$ km/sec for the shallower California events. Geometric spreading, $g(\Delta)$, is taken from Kanamori and Stewart's (1976) Figure 8. The radiation pattern and free-surface receiver effect, $R_{\theta\phi}$ and C, are computed from the

station distance and azimuth and the focal mechanism of the event. The effective radiation pattern, $R_{\theta\phi}$, is obtained by first computing the amplitudes of the P, pP, and sP phases at the station using equation (8) of Kanamori and Stewart (1976), and then taking the root-mean-square value. A similar procedure is used by Boore and Boatwright (1984).

In reality, the three phases will interfere to yield a frequency-dependent radiation pattern. However, this is not important in an average sense, especially for extended ruptures. To show this, we divide a dipping fault plane into subfaults, choose the point where rupture begins, and let rupture propagate with an average rupture velocity. For each subfault, we calculate the amplitudes of the P, pP, and sP phases (which depend on the fault mechanism) and the time delays of the pP and sP phases after P (which depend on the depth of the subfault and the position of the receiver). We sum the arrivals in time (each arrival is simply a spike), Fourier transform, and divide the spectrum by the spectrum of the P arrivals only, to normalize it. The resulting spectrum is essentially the radiation pattern as a function of frequency. Figure 2.2 shows the average of eight such spectra computed at different azimuths for a thrust mechanism on a 150 km by 70 km fault plane dipping 30° divided into 105 subfaults. The average radiation pattern ratio exhibits little frequency dependence and matches the average scalar radiation pattern ratio, $\sqrt{(R^P)^2 + (R^{pP})^2 + (R^{sP})^2}/R^P$ where $R^X$ represents the amplitude of the phase X. This justifies our use of a frequency-independent radiation pattern.

The spectrum of each record in Table 1 is corrected according to (2.1). Then, for each earthquake, the corrected spectra are averaged and shown in
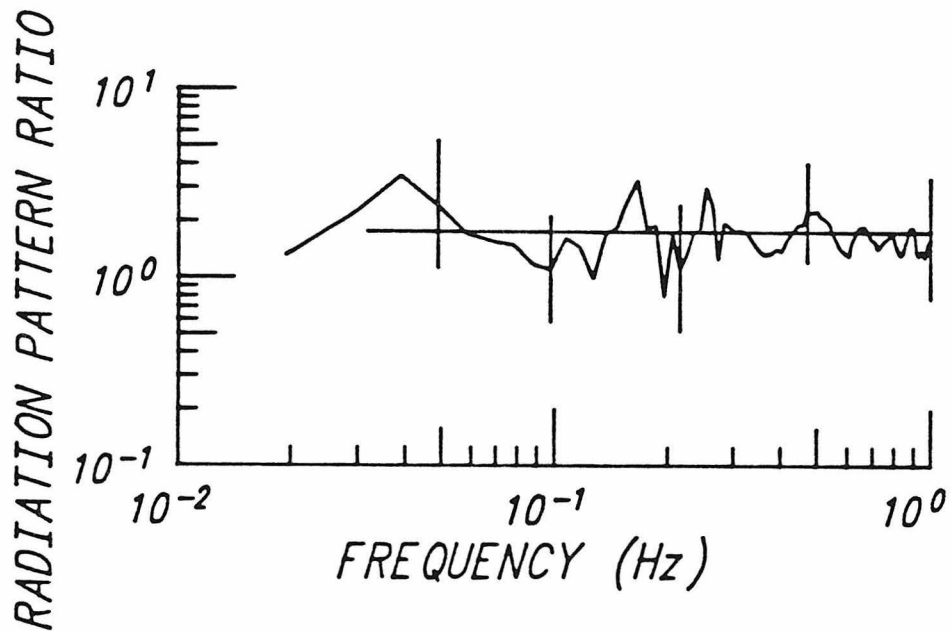
Figure 2.2. Average radiation pattern ratio as a function of frequency for an extended fault model in a half-space. We divide $[P + pP + sP](\omega)$ by $P(\omega)$ for each of eight azimuths and average the results around an extended thrust event on a fault-plane that dips $30°$. The vertical lines show standard deviations of the average at selected frequencies. The horizontal line represents the average of the ratios of the scalar radiation pattern ratio, $\sqrt{(R^P)^2 + (R^{pP})^2 + (R^{sP})^2}/R^P$. The good comparison justifies our use of the frequency-independent scalar radiation pattern in computing the source spectrum.

Figures 2.3 and 2.4. Theoretical spectra for an $\omega^{-2}$ model are shown as a reference (for a description of the model, see (2.4) below). The spectral values at the low-frequency end of the spectrum in Figures 2.3 and 2.4 were obtained from the scalar seismic moments determined from long-period waves. The standard deviations of the average are shown by vertical bars. The scatter seems to be caused by path and receiver-site effects, since removing the effects of distance, distance-dependent t*, radiation pattern, and the free-surface receiver effect caused the standard deviations to decrease less than 20%. In this connection, Koyama and Zheng (1985) have observed that short-period P-waves do not follow the P-wave radiation pattern. Considering the uncertainties in our method of reduction and the scatter in the data, we must be careful not to overinterpret the results. However, it is evident in Figure 2.3 that the Tongan earthquake has proportionally less high-frequency energy than the other five events. This can be interpreted as the result of weaker coupling of the subduction interface caused by the greater age and density of the subducting sea-floor (Ruff and Kanamori, 1980). The Costa Rica earthquake spectrum falls between that of the Tongan and Akita-Oki events.

Figure 2.4 shows source spectra of the two California events, Coalinga and San Fernando, with the $\omega^{-2}$ spectral model as a reference. Figures 2.3 and 2.4 illustrate the pitfalls of considering only spectral slopes or approximating the $\omega^{-2}$ model by a line of slope 0 and a line of slope -2. The roll-off actually occurs over nearly a decade in frequency. A straight line fit to the Akita-Oki spectrum by least squares between 0.1 Hz and 1 Hz has a slope of -1.75, but it is evident from Figure 2.3 that the Akita-Oki spectrum is close to the $\omega^{-2}$ model.
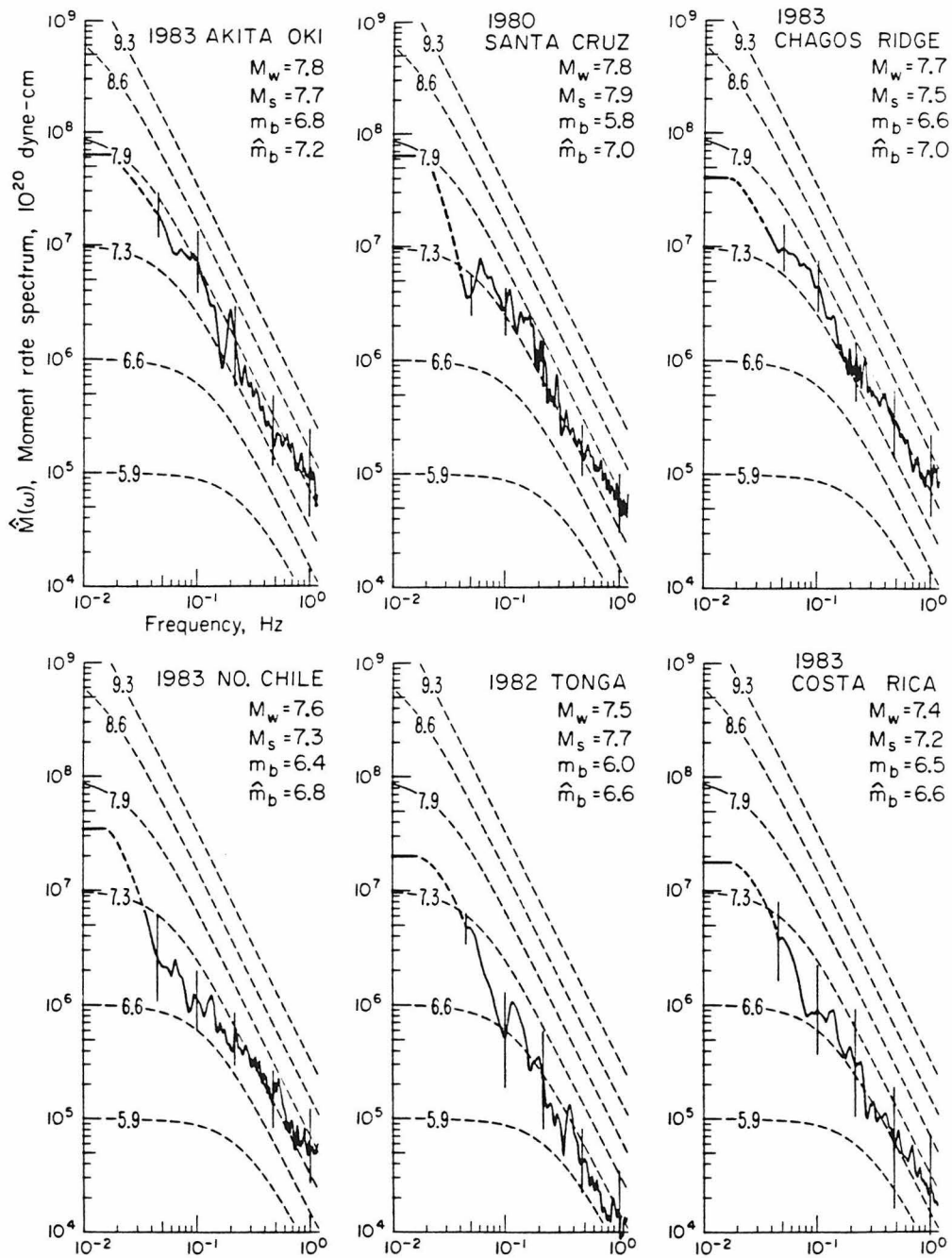
Figure 2.3. Comparison of the average moment rate spectra for six earthquakes. The dashed curves show theoretical spectra for an $\omega^{-2}$ model. These curves are shown as a reference. The spectral values at the low-frequency end were obtained from the scalar seismic moment determined from long-period waves. The vertical bars show standard deviations at selected frequencies.
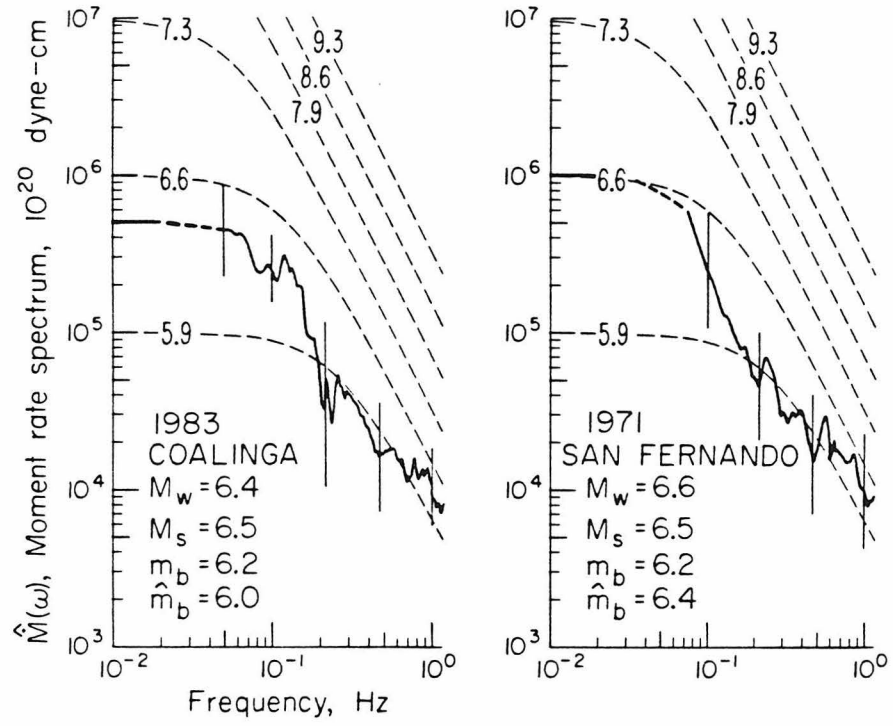
Figure 2.4. Moment rate spectra for two California earthquakes. See caption for Figure 2.3.

## 2.3  Relation Between $\hat{m}_b$ and Spectral Amplitude

We can obtain source spectra from GDSN records as described above only for recent earthquakes; the largest earthquake that was well-recorded on GDSN has $M_W$=7.8. For great earthquakes, only $\hat{m}_b$'s measured from WWSSN records are available. In this section we use the $\hat{m}_b$ data to estimate spectral amplitudes at short periods. For $M_W$=9.0 and 8.0, we estimate an average $\hat{m}_b$=7.48 and 6.95, respectively, from (1.1), and an average period, T=1.8 seconds, from Figure 1.4c. We fix the distance, $\Delta$, at about the average of the station distances used to calculate $\hat{m}_b$; we take $\Delta$=75°. Then (1.1) gives the average maximum ground motion from body waves, $A_g = 10.8\mu$ and $5.1\mu$, at $\Delta$=75° for $M_W = 9.0$ and 8.0, respectively.

The conventional procedure for relating time-domain amplitude of a signal to its spectral amplitude is to postulate that

$$\hat{u}(\omega_o) \ \alpha \ A \ C_D{}^m \tag{2.2}$$

where A is the maximum amplitude in the time domain, $\hat{u}(\omega_o)$ is spectral amplitude at the angular frequency where A is measured or defined, and $C_D$ is some measure of the duration of the signal. For well-dispersed waves (e.g. 20 second surface waves) m can be taken to be 0 (Aki, 1967). However, the appropriate value for m in (2.2) is not obvious for complex short-period body waves. If the wave-train is approximated by a sine wave modulated by a Gaussian envelope of amplitude A and duration $C_D$, then (2.2) applies with m=1. That approximation naturally produces a very sharp spike in the spectrum, and ignores the random nature of short-period waves. If the wave-train

is approximated by a random signal of maximum amplitude A and duration $C_D$ with an appropriate bandwidth, then in (2.2) m is 0.5 (Koyama and Zheng, 1985, equation A12).

We prefer an empirical approach to estimate $\hat{u}(\omega_o=2\pi/T)$ from A. For the digital data, both time-domain and spectral amplitudes are known, so we plot log $[A/\hat{u}(\omega_o)]$ vs. $M_W$ in Figure 2.5. We use available short-period records from the GDSN stations listed in Table 1, as well as short-period GDSN records of the 1984 Morgan Hill, California, 1978 Oaxaca, 1979 Petatlan, and 1979 Colombia earthquakes. The last three events are included in Table 1 of Chapter 1. Two hand-digitized records are used: the 1964 Alaskan earthquake recorded by a Wood-Anderson seismograph at Pasadena, California, and the 1960 Chilean earthquake recorded by a Willmore short-period vertical seismograph at Halifax, Canada. The Wood-Anderson response is deconvolved from the 1964 Alaska record, and a standard short-period DWWSSN response is convolved with the resulting ground displacement. The simulated short-period record is then treated like the GDSN records. We obtain two values of log $[A/\hat{u}(\omega_o)]$ from Figure 2.5 that correspond to $M_W=8.0$ and $M_W=9.0$ and are shown by X's.

The reference line in Figure 2.5 represents (2.2) with m=0.25. This can be seen by applying the standard scaling relation between moment and length, ($M_0 \propto L^3$), and the proportionality between fault length and coda duration demonstrated in Figure 1.3b. Although the data for great earthquakes are sparse, m does not seem to be a strong function of $M_W$ or C, so that (2.2) may be a valid assumption. From Figure 2.5, m appears to be significantly less than 0.5.

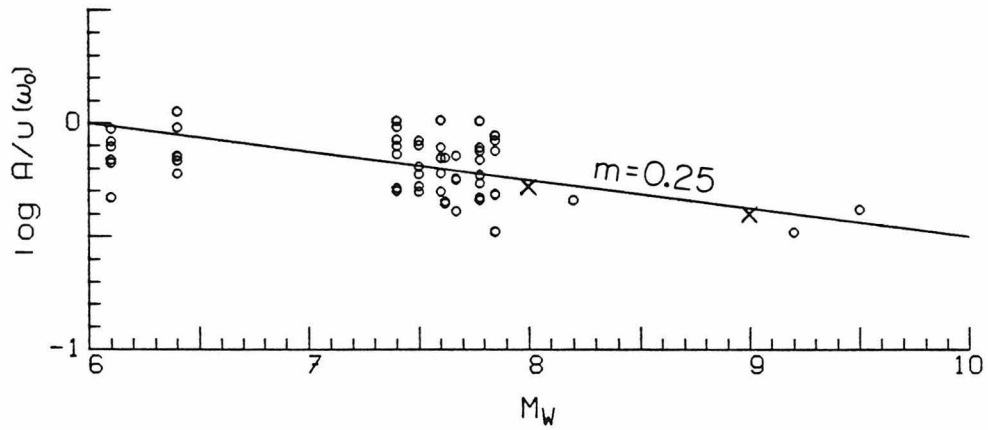Figure 2.5. Ratio of time-domain amplitude to spectral amplitude as a function of $M_W$. $A_g$ is time-domain amplitude at period, T, and $U(\omega_o)$ is frequency-domain amplitude at $\omega_o = 2\pi/T$ after the instrument response is removed. The X's show the ratios used in this study to estimate spectral amplitudes from $\hat{m}_b$. The reference line represents equation (2.2) with m=0.25.

Finally, the moment rate spectral density, $\hat{M}(\omega_0)$, is calculated from $\hat{u}(\omega_o)$ by (2.1) using the following parameters: as before, $\rho = 2.8$ gm/cm$^3$ and $\alpha = 6.5$ km/sec, $g(\Delta) = 0.3$, $C = 1.8$, $R_{\theta\phi} = 1.0$, and $t^* = 0.7$ sec. The moment rate spectral densities thus estimated from $\hat{m}_b$ and T are

$$\hat{M} \left(0.55 \text{ Hz} = \frac{1}{1.8 \text{ sec}}\right) = \begin{cases} 8.8 \times 10^{25} \text{ dyne-cm} & \text{for } M_W = 9.0 \\ 1.9 \times 10^{25} \text{ dyne-cm} & \text{for } M_W = 8.0. \end{cases} \quad (2.3)$$

In the same way that (2.3) was determined, we can determine $\hat{M}(0.55\text{Hz})$ for the 1964 Alaskan earthquake ($M_W$=9.2). From Table 1 of Chapter 1, $\hat{m}_b$ is 7.64 and T is 1.81 sec. Therefore, $A_g$ is 12.5 $\mu$ at a distance of 75°. We choose log $[A/u(\omega_o)] = $ -0.44 from Figure 2.5. Then for the 1964 Alaskan earthquake

$$\hat{M} (0.55 \text{ Hz}) = 1.3 \times 10^{26} \text{ dyne-cm}$$

in contrast to Koyama and Zheng's (1985) estimate of $1.7 \times 10^{27}$ dyne-cm (at 1.4 sec, Koyama, written comm.). Koyama and Zheng's estimate is larger than ours for two main reasons. First, they use a $t^*$ of about 1.4 sec compared to our $t^*$ of 0.7 sec. This difference tends to overestimate the source spectrum by a factor of 5. In addition, their estimate of spectral density from time-domain amplitude is based on their equation A12, which overestimates the spectrum by a factor of 1.5 to 2 (see Koyama and Zheng, 1985, Figure A3). Our estimate of $\hat{M}(0.55 \text{ Hz})$ from $\hat{m}_b$ from the 1964 Alaskan earthquake is consistent with (1.3 times larger than) the spectrum obtained from the Pasadena Wood-Anderson record of the 1964 Alaskan earthquake (see below and Figure 2.7c).

## 2.4 Discussion: Comparison of Data with Spectral Models

Figure 2.6 compares four spectra from GDSN records and the spectral amplitudes that we estimated from the $\hat{m}_b$ data to an $\omega^{-2}$ spectral model given by:

$$\hat{M}(\omega) = \frac{M_0\,\omega_c{}^2}{\omega_c{}^2 + \omega^2} \quad \text{with corner frequency,} \quad \frac{\omega_c}{2\pi} = 0.49\beta\left[\frac{\Delta\sigma}{M_0}\right]^{\frac{1}{3}} \quad (2.4)$$

with stress parameter, $\Delta\sigma$=30 bars, and S-wave velocity, $\beta$=3.75 km/sec (Brune, 1970). The spectral amplitudes estimated from $\hat{m}_b$ and given in (2.3) are shown in Figure 2.6 by dots whose error bars represent the change in $\hat{M}(\omega_o)$ associated with a change of $\pm$ 0.17 in $\hat{m}_b$, which is the standard error of the estimate of the least squares fit to $\hat{m}_b$ vs. $M_W$. Figure 2.6 also compares the same data to the Gusev source spectral model. The Gusev spectral model was constructed empirically from a synthesis of different magnitude relations (Gusev, 1983; Aki, 1983, 1972). Hence, it is a more complicated model than the $\omega^{-2}$ model, as shown by its lack of similitude. For large moments, the Gusev model predicts decreased amplitudes at 10 to 20 seconds and enhanced amplitudes at about 2 seconds compared to the $\omega^{-2}$ model with $\Delta\sigma$=30 bars. Of the digitally recorded events, the Akita-Oki earthquake fits the $\omega^{-2}$ model better than it fits the Gusev model, the Costa Rica earthquake fits the Gusev model better, and the Tonga earthquake has a faster spectral fall-off than the $\omega^{-2}$ model.

From the definition of $M_W$, the spacing of the spectral amplitudes in (2.3) for $M_W$=8.0 and 9.0 yields
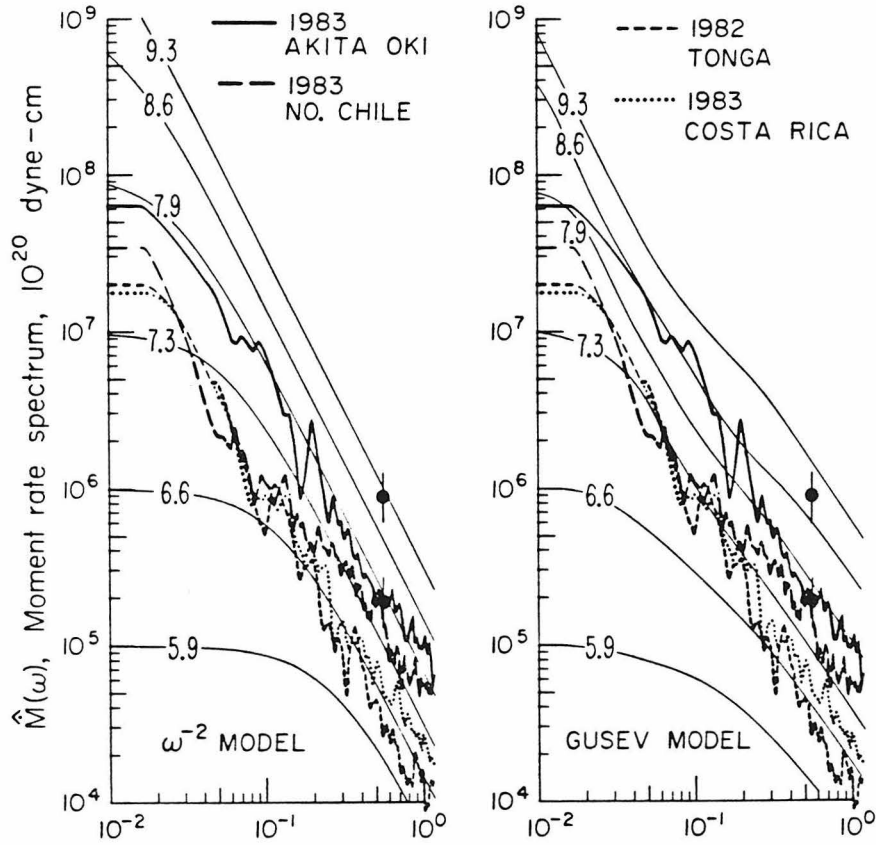
Figure 2.6. Comparison of the spectra of four earthquakes and spectral amplitudes estimated from the $\hat{m}_b$ data with $\omega^{-2}$ and Gusev spectral models. The spectral values at the low-frequency end were obtained from the scalar seismic moments determined from long-period waves. Between 100 sec and about 30 sec, the spectra are inferred by interpolation. The two dots show the spectral amplitudes at 0.55 Hz estimated from $\hat{m}_b$ for $M_W = 8.0$ and $M_W = 9.0$. The vertical bars show the uncertainty associated with the standard error of the estimate in $\hat{m}_b$ vs. $M_W$, $\pm 0.17$.

$$\hat{M} \left( 0.55 \text{ Hz} = \frac{1}{1.8 \text{ sec}} \right) \alpha M_0^{0.45}. \tag{2.5}$$

An exponent of 1/3 would be consistent with the spectral fall-off of -2 associated with an $\omega^{-2}$ model. The exponent of 0.45 in (2.5) suggests a spectral fall-off of -1.7. However, to fit the absolute levels in (2.3) to an $\omega^{-1.7}$ model defined in a fashion similar to (2.4), the $\Delta\sigma$ in (2.4) would need to be much smaller than 30 bars. A comparison of (2.5) with (1.3) and (2.2) suggests that m in (2.2) is about 0.3, providing a further indication than Figure 2.5 that m is significantly smaller than 0.5.

Hartzell and Heaton (1985) obtained source spectra from hand-digitized teleseismic records of 61 large and great earthquakes recorded by the Pasadena, California Benioff 1-90 seismometer. They found significant differences between spectra of similar size earthquakes. They grouped the earthquakes in five magnitude ranges ($M_W$ = 7.0 to 7.5, 7.5 to 8.0, 8.0 to 8.5, 8.5 to 9.0, and 9.0 to 9.5), averaged together the spectra in each group, and plotted the averages in their Figure 11a. We adjust their spectra (which are heavily smoothed) to be consistent with our choice of parameters $(\alpha, \rho, t^*, R_{\theta\phi}, C)$. With the following changes, we average the spectra of the earthquakes in the same five magnitude ranges and plot the averages in Figure 2.7a. Using a P-wave velocity, $\alpha$=6.5 km/s, as we do, instead of Hartzell and Heaton's (1985) $\alpha$=8.0 km/s lowers the level of the spectra. Using a radiation pattern computed separately for each event from the mechanisms in Hartzell and Heaton's (1985) Table 1, as we do, also has the effect, in general, of lowering the level of the spectra, because Hartzell and Heaton (1985) correct each spectrum with the same average P-wave radiation coefficient and ignore the pP and sP phases (the inclusion of which increases the amplitude of the
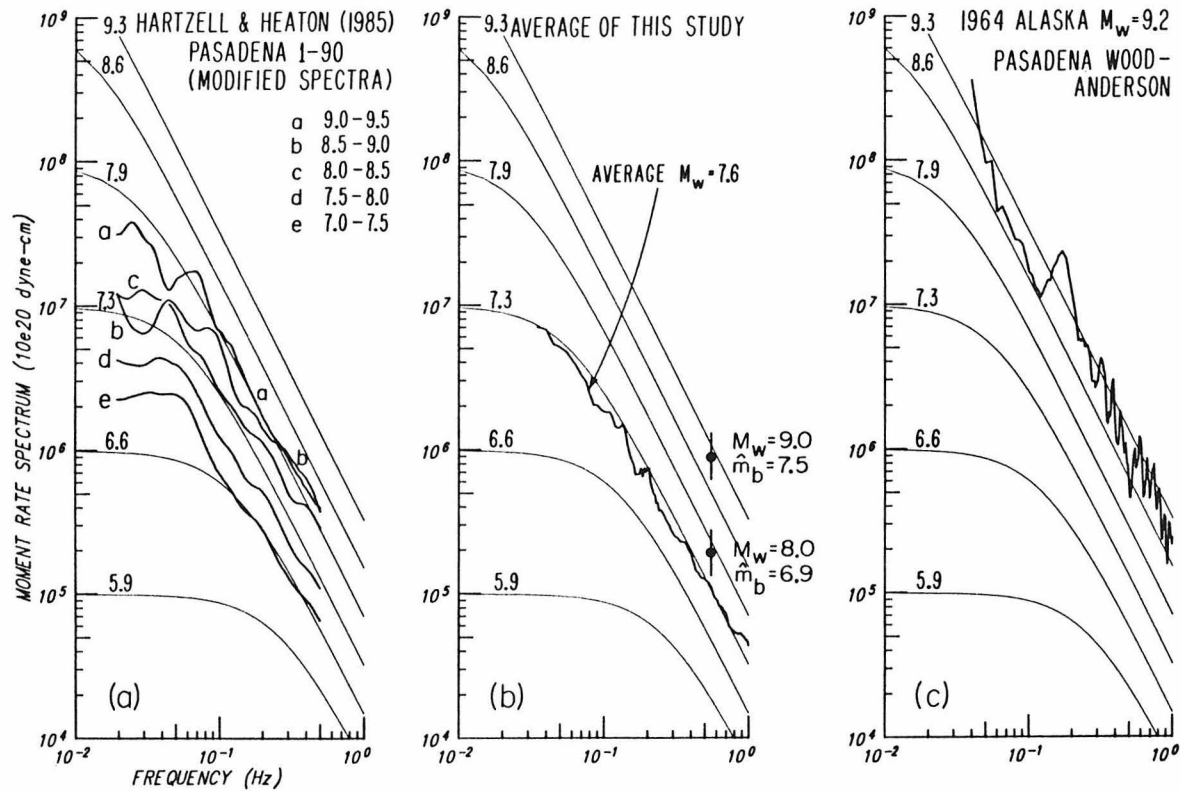
Figure 2.7. (a) Averages of the source spectra of 61 Pasadena, California Benioff 1-90 records. The earth-quakes have been grouped into five magnitude ranges: $M_W$ = 7.0 to 7.5, 7.5 to 8.0, 8.0 to 8.5, 8.5 to 9.0, and 9.0 to 9.5. The smoothed spectra in each group have been averaged together. The $\omega^{-2}$ spectral model described in equation (2.4) is shown for reference. This figure can be compared with Hartzell and Heaton's (1985) figure 11a. (b) The average of the source spectra of the 6 earthquakes in Figure 2.3. The average $M_W$ is 7.63. The two dots show the spectral amplitudes at 0.55 Hz estimated from $\hat{m}_b$ for $M_W$ = 8.0 and $M_W$ = 9.0. The vertical bars show the uncertainty associated with the standard error of the estimate in $\hat{m}_b$ vs. $M_W$, ±0.17. (c) The source spectrum of the Pasadena Wood-Anderson record (radial component) of the 1964 Alaska earthquake ($M_W$ = 9.2).

radiation pattern). The spectral shapes have changed because we use $t^*=0.7$ sec instead of $t^*=1.0$ sec. We also reclassify the 1957 Aleutian event, their earthquake #42, into a lower moment range, $M_W = 8.5$ to 9.0, as suggested by Ruff, Kanamori, and Sykes (1985). Because of digitization error, the 1-90 spectra are not reliable at periods shorter than 2 seconds. The $\omega^{-2}$ model specified in (2.4) is shown for reference. The only earthquake that we and Hartzell and Heaton (1985) both analyzed is the 1983 Akita-Oki event. For that event our average spectrum from GDSN records agrees well with the spectrum of the Pasadena 1-90 record. Figure 2.7a and Hartzell and Heaton's Figure 11a show an apparent saturation of spectral amplitude with increasing moment.

Figure 2.7b shows the average of the 6 source spectra presented in Figure 2.3. The average $M_W$ for those 6 events is 7.63. Therefore, the average spectrum from this study falls below the $\omega^{-2}$ model described in (2.4) by about 0.4 $M_W$ units or, equivalently, 0.6 log $M_0$ units. However, it lies slightly above Hartzell and Heaton's (1985) average spectrum for $M_W = 7.5$ to 8.0. The average spectrum from this study does not have a spectral structure suggested by Gusev. The spectral amplitudes in (2.3) estimated from $\hat{m}_b$ are also shown by dots in Figure 2.7b. They do not show the saturation of spectral amplitude with increasing moment that is seen in the 1-90 spectra (Figure 2.7a).

The spectrum of the Pasadena, California Wood-Anderson record of the 1964 Alaskan earthquake is shown in Figure 2.7c. We estimated vertical displacements from the horizontal Wood-Anderson record (radial component) using Gutenberg's calibration for PH waves. The level of the spectrum is consistent with the $\omega^{-2}$ model described in (2.4) and with the spectral amplitude

obtained from $\hat{m}_b$ in the previous section, but it is not consistent with the saturation of spectral amplitude with increasing moment seen in Figure 2.7a. Since we reclassified the 1957 Aleutian earthquake into a lower magnitude range, our magnitude range 9.0 to 9.5 in Figure 2.7a contains only two events: the 1960 Chilean earthquake and the 1952 Kamchatka earthquake (which could be moved to a lower magnitude range, too). Hartzell and Heaton (1985) and we did not include the 1964 Alaskan earthquake spectrum in the average spectra because the 1-90 record for that event is off-scale. Similarly, Hartzell (personal comm., 1985) notes that the Wood-Anderson record of the 1964 Alaskan earthquake is significantly bigger than the Wood-Anderson record of the 1960 Chilean earthquake after correction for the effects of distance. This is consistent with the levels of the spectra shown in Figure 2.7a and 2.7c. If an on-scale 1-90 record were available for the 1964 Alaska earthquake, Hartzell and Heaton's average spectrum for $M_W$ between 9.0 and 9.5 (their Figure 11a) would be significantly higher.

Taken together, the data from this study (Figures 2.7b and 2.7c) show spectral levels slightly above the 1-90 spectral levels for $M_W$ from 7.0 to 8.5. For $M_W$ from 8.5 to 9.5, our analysis of $\hat{m}_b$ indicates spectral levels significantly higher than the 1-90 levels.

Rather than discuss the differences and similarities between the models, we prefer to emphasize the differences between different events and the importance of determining the whole spectrum. The $\omega^{-2}$ model is a simple and useful reference model for discriminating between different earthquakes. However, the spectra of individual earthquakes deviate from the model considerably.

See Boore (1986) for further discussion of how $\hat{m}_b$ and $M_S$ might discriminate between various spectral models. Boore (1983) develops a stochastic method for simulation of near-field strong ground motions using random vibration theory. He demonstrates that an $\omega^{-2}$ model with $\Delta\sigma$ of 100 bars can explain essential aspects of strong ground motions for earthquakes in western North America with $M_W$ of 5.0 to 7.7. Boore (1986) extends this method to simulate teleseismic P-waves, and finds that an $\omega^{-2}$ model with $\Delta\sigma$ of 50 bars explains our $\hat{m}_b$ values for earthquakes with $M_W$ up to 9.5.

## 2.5  Conclusions

Magnitude scales are by definition a measurement at one period only and may give an inadequate and sometimes incorrect indication of the source spectrum. The moment rate spectra that we determined directly from intermediate-period and short-period teleseismic digital records are shown in Figures 2.3 and 2.4. Significant differences in spectral fall-off occur between events, and may be due to differences in seismic coupling.

Using the short-period digital records, we obtain an empirical relation between time-domain amplitude and spectral amplitude for short-period waves. Spectral amplitudes are estimated from the $\hat{m}_b$ data. We compare our results to the $\omega^{-2}$ and Gusev spectral models in Figures 2.6 and 2.7b. Neither model can completely represent the data. Nevertheless, we consider the $\omega^{-2}$ model a useful reference model for comparing different events. The average source spectrum of the six large events analyzed here does not have a spectral structure suggested by Gusev.

## 2.6 References

Aki, K., Scaling law of seismic spectrum, *J. Geophys. Res., 73* 1217-1231, 1967.

Aki, K., Scaling law of earthquake source time-function, *Geophys. J. R. Astr. Soc., 31*, 3-25, 1972.

Aki, K., Strong-motion seismology, Proceedings of the International School of Physics, Enrico Fermi, Earthquakes Observation, Theory and Interpretation, H. Kanamori and E. Boschi, 1983.

Boore, D. M., Stochastic simulation of high-frequency ground motions based on seismological models of the radiated spectra, *Bull. Seism. Soc. Am., 54*, 1865-1894, 1983.

Boore, D., Short-period P-wave radiation from large earthquakes: implications for spectral scaling laws, *Bull. Seism. Soc. Am., 76*, 43-64, 1986.

Boore, D. M., and J. Boatwright, Average body-wave radiation coefficients, *Bull. Seism. Soc. Am., 74*, 1615-1621, 1984.

Brune, J., Tectonic stress and the spectra of seismic shear waves from earthquakes, *J. Geophys. Res., 75*, 4997-5009, 1970.

Der, Z. A., and A. C. Lees, Methodologies of estimating $t^*(f)$ from short-period body waves and regional variations of $t^*(f)$ in the United States, *Geophys. J. R. Astr. Soc.*, submitted, 1984.

Gusev, A. A., Descriptive statistical model of earthquake source radiation and its application to an estimation of short-period strong motion, *Geophys. J. R. Astr. Soc., 74*, 787-80, 1983.

Haskell, N., Total energy and energy spectral density of elastic wave radiation from propagating faults, *Bull. Seism. Soc. Am., 54*, 1811-1842, 1964.

Haskell, N., Total energy and energy spectral density of elastic wave radiation from propagation faults, 2, *Bull. Seism. Soc. Am., 56*, 125-140, 1966.

Kanamori, H., Attenuation of P waves in the upper and lower mantle, *Bull. Earthquake Res. Inst. Tokyo Univ., 45*, 299-312, 1967.

Kanamori, H., and G. S. Stewart, Mode of the strain release along the Gibbs fracture zone, Mid-Atlantic Ridge, *Phys. Earth Planet. Inter., 11*, 312-332, 1976.

Hartzell, S. H., and T. Heaton, Teleseismic time functions for large shallow subduction zone earthquakes, *Bull. Seism. Soc. Am., 75*, 965-1004, 1985.

Koyama, J., and S. Zheng, Excitation of short-period body waves by recent

great earthquakes, *Phys. Earth Planet. Inter., 37*, 108-123, 1985.

Langston, C. A., The February 9, 1971 San Fernando earthquake: a study of source finiteness in teleseismic body waves, *Bull. Seism. Soc. Am., 68*, 1-29, 1978.

Ruff, L. and H. Kanamori, Seismicity and the subduction process, *Phys. Earth Planet. Inter., 23*, 240-252, 1980.

Ruff, L., H. Kanamori, and L. Sykes, The 1957 great Aleutian earthquake (abs.), *EOS, 66*, 298, 1985.

# Chapter 3

## Source Characteristics of the 1985 Michoacan, Mexico Earthquake
## at Periods of 1 to 30 Seconds

### Abstract

Source characteristics of the Sept. 19, 1985 Michoacan, Mexico earthquake and its aftershock on Sept. 21 were inferred from broadband and short-period teleseismic GDSN records. The Michoacan source spectrum is enriched at 30 s and depleted at 1 to 10 s relative to an average source spectrum of large interplate subduction events. Source spectra for the Sept. 21 aftershock, 1981 Playa Azul, 1979 Petatlan, and 1978 Oaxaca events follow a trend similar to that of the 1985 Michoacan event. This spectral trend may characterize the Mexican subduction zone.

A station-by-station least-squares inversion of the Michoacan earthquake records for the source time function yielded three source pulses, which we interpret  as events on the fault plane. The first two are similar in moment, and the third contains only 20% of the moment of the first. Directivity is evident in the timing. At each station, we measured the time differences between the pulses, and performed a least-squares nonlinear estimation of the strike, distance, and time separation between the events to locate them relative to one another. The second event occurred 26 s after the first, and 82 km southeast of it, indicating southeastward rupture along the trench. The two large events are also seen in the near-field strong motions.

The mainshock records, spectrum, and time functions contain less high frequency radiation than those of the 1985 Valparaiso, Chile earthquake. Apparently, the Michoacan earthquake ruptured two relatively smooth, strong patches which generated large 30 s waves, but small 1 to 10 s waves. Such behavior contrasts with the Valparaiso event which had a more complex rupture process and generated more 1 to 5 s energy. This difference is consistent with the higher near-field accelerations recorded for the Valparaiso event.

## 3.1  Introduction

On September 19, 1985 a large subduction earthquake ($M_W = 8.0$ or 8.1) occurred in the Michoacan gap along the Mexican trench (see Figure 3.1). It had the largest seismic moment of any earthquake in 1985. Unusually high accelerations in Mexico City caused heavy damage and thousands of deaths. From an earthquake engineering point of view, it is important to distinguish between the source effects of this earthquake and site or propagation effects peculiar to Mexico City. To this end, we analyzed teleseismic broadband and short-period GDSN (Global Digital Seismic Network) records of the Sept. 19 earthquake and its Sept. 21 aftershock ($M_W = 7.6$) to determine their source characteristics at periods of 1 to 30 s. We compared their source spectra to those of other recent Mexican subduction earthquakes which were digitally recorded. GDSN records are also available for the March 3, 1985 Valparaiso, Chile earthquake ($M_W = 8.0$) along the Chile trench, the second largest earthquake in 1985. We will show that the Michoacan earthquake source has a long duration (about 1 minute), but is depleted in energy at 1 to 10 s periods relative to an average source of that size and relative to the Valparaiso earthquake, suggesting that the unusually high accelerations in Mexico City were not a source effect. This conclusion is consistent with a comparison of the near-field strong motion data for the two events. Teleseismic data, therefore, can be used to predict some characteristics of near-field strong motions.
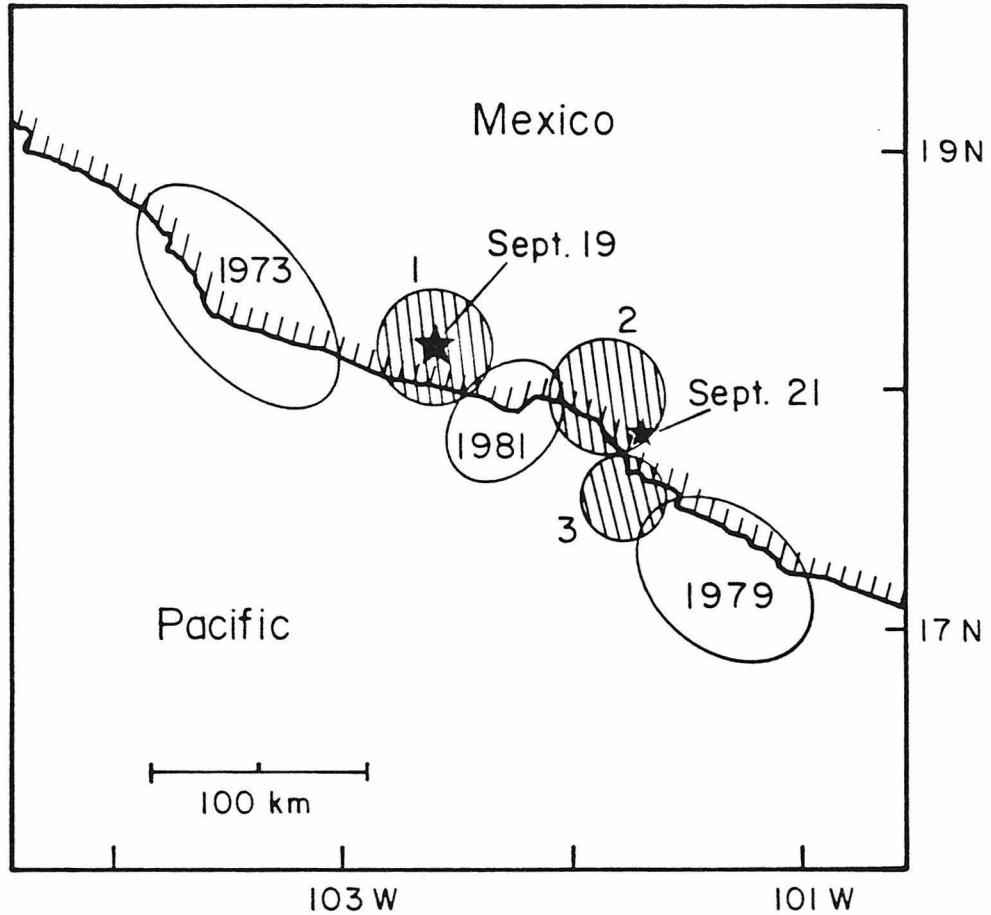
Figure 3.1. Map view of the 1985 Michoacan, Mexico earthquake rupture zone. Stars show the PDE epicenters of the mainshock and largest aftershock. The shaded areas show the inferred rupture zones of the three source sub-events of the mainshock found by this study, assuming a rupture velocity of 2.5 km/s and sub-event rise times of 10 s, 10 s, and 7 s. Rupture zones inferred from aftershock areas of the 1973, 1979, and 1981 earthquakes are also shown.

## 3.2  GDSN Records and Spectral Analysis

Figure 3.2 shows some of the broadband and short-period vertical records available for the Sept. 19 and Sept. 21 events. Two distinct source events about 25 s apart are clearly visible on the broadband records of the mainshock.

We performed a spectral analysis of the available records, using the procedure described in Chapter 2. Table 1 lists the records used. For the focal mechanism we used fault strike $\phi = -72°$, dip $\delta = 9°$, and rake $\lambda = 72°$ for both the mainshock and the aftershock (Eissler, Astiz, and Kanamori, 1986).

Figure 3.3 shows the average moment rate spectra for the Michoacan mainshock and the Sept. 21 aftershock, and the 1981 Playa Azul, 1979 Petatlan, 1978 Oaxaca, and 1985 Valparaiso, Chile earthquakes. All of the above earthquakes, except the last, occurred along the Mexican subduction zone. The Petatlan and Oaxaca spectra were computed from only 2 and 3 short-period SRO records, respectively; the Playa Azul spectrum was computed from 7 short-period SRO and DWWSSN records. The Michoacan spectrum and the Sept. 21 aftershock spectrum were computed from 15 GDSN records, mostly broadband. The spectral values at the low-frequency end of the spectra in Figure 3.3 were obtained from the scalar seismic moments determined from long-period waves. Theoretical spectra for an $\omega^{-2}$ source model with a stress drop of 30 bars are shown as a reference (for a description of the model, see equation 2.4). The dashed line shows the average source spectrum for 7 large interplate subduction earthquakes; we scaled the average spectrum to $M_W = 8.0$, so that it could be easily compared to the Michoacan spectrum.
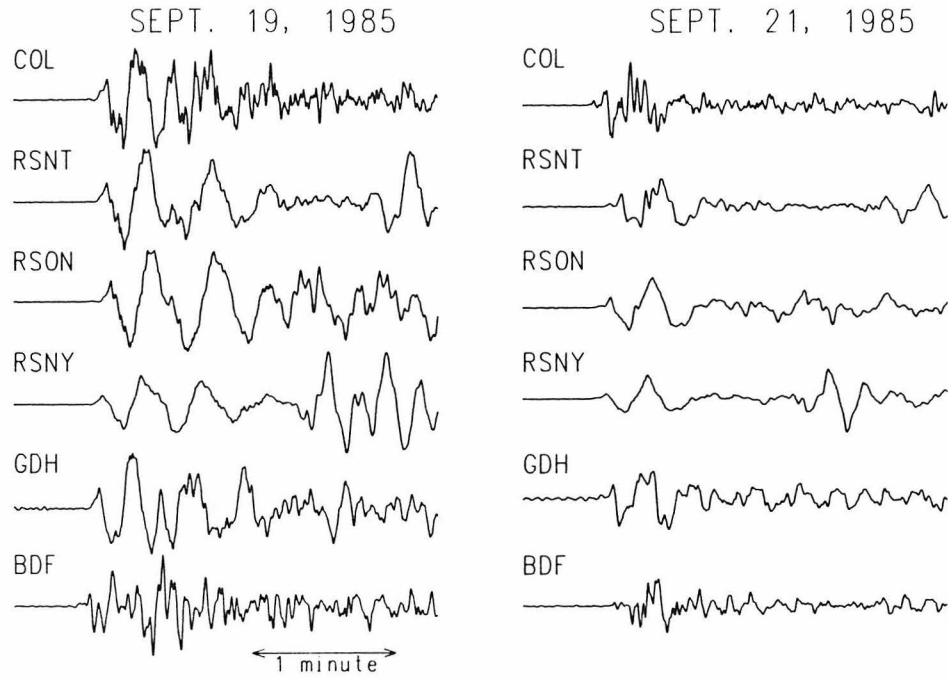
Figure 3.2. Vertical components of teleseismic broadband GDSN records from stations COL (distance=55°, azimuth=338°), RSNT (45, 352), RSON (33, 10), RSNY (35, 36), GDH (59, 18), and BDF (64, 118). At each station, the mainshock and aftershock records are plotted to the same scale.
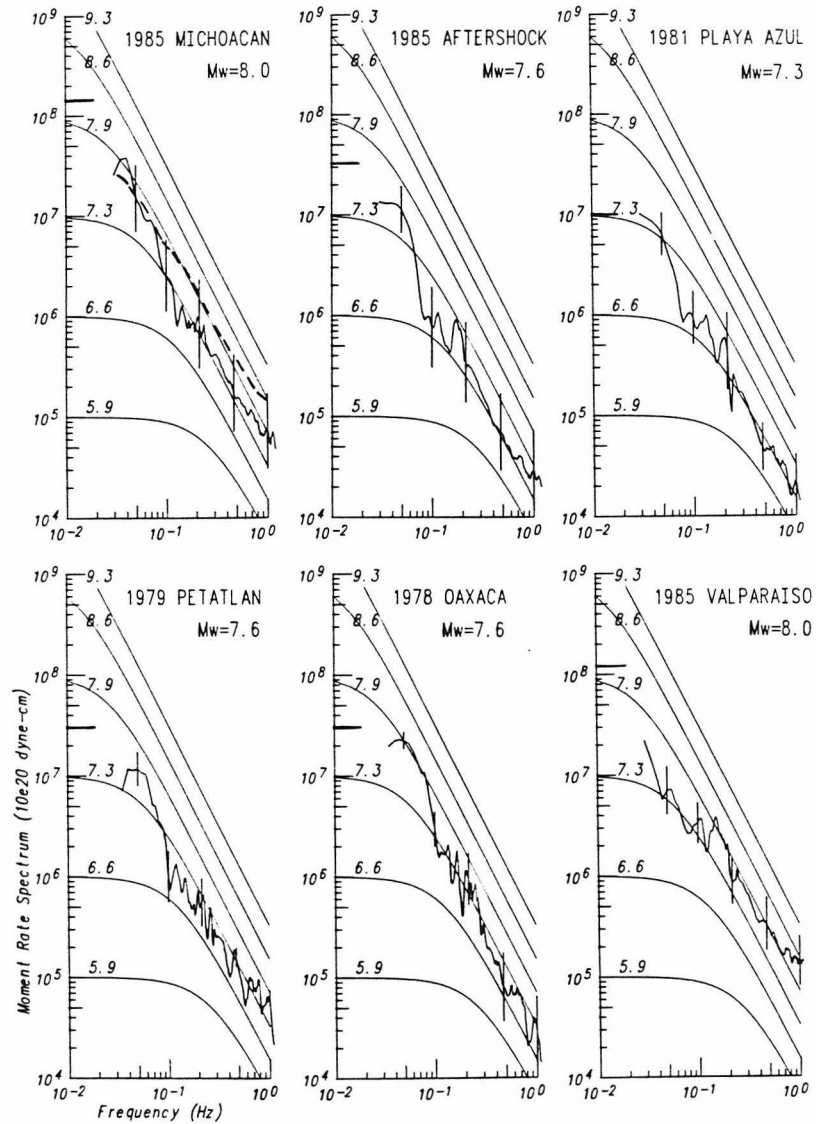
Figure 3.3. Comparison of the average moment rate spectra for six earthquakes. The spectral values at the low-frequency end were obtained from the scalar seismic moment determined from long-period waves. The vertical bars show standard deviations at selected frequencies. As a reference, theoretical spectra for an $\omega^{-2}$ model are shown by thin lines. The dashed line on the Michoacan spectrum shows the average spectrum of 7 subduction earthquakes scaled to $M_W=8.0$. The spectra of earthquakes along the Mexican trench are depleted in periods of 1 to 10 s relative to the average spectrum of subduction earthquakes.

Table 1: Records Used in Spectral Analysis

| Station | Type | $\Delta$ (deg) | Azimuth (deg) | $R_{\phi\delta}$ | C | $g(\Delta)$ |
|---|---|---|---|---|---|---|
| MICHOACAN, MEXICO Sept. 19. 1985 $M_W=8.0$ | | | | | | subduction thrust |
| KONO | SP ASRO | 85.0 | 28.1 | 1.41 | 1.89 | 0.27 |
| ZOBO | SP ASRO | 48.3 | 133.2 | 0.33* | 1.73 | 0.41 |
| HON | SP DWWSSN | 52.0 | 283.2 | 0.55 | 1.75 | 0.39 |
| SCP | IP DWWSSN | 31.0 | 38.1 | 2.02 | 1.63 | 0.61 |
| LON | IP DWWSSN | 32.6 | 335.2 | 1.07 | 1.64 | 0.57 |
| COL | IP DWWSSN | 55.5 | 338.5 | 1.06 | 1.76 | 0.37 |
| KEV | IP DWWSSN | 85.3 | 15.6 | 1.34 | 1.89 | 0.27 |
| GDH | IP DWWSSN | 59.2 | 18.2 | 1.71 | 1.78 | 0.36 |
| TOL | IP DWWSSN | 84.8 | 49.7 | 1.40 | 1.89 | 0.27 |
| BDF | IP DWWSSN | 63.5 | 118.5 | 0.55 | 1.80 | 0.35 |
| AFI | IP DWWSSN | 75.3 | 249.9 | 1.04 | 1.85 | 0.30 |
| RSNT | IP RSTN | 45.0 | 352.1 | 1.43 | 1.71 | 0.43 |
| RSON | IP RSTN | 33.4 | 10.2 | 1.82 | 1.65 | 0.56 |
| RSNY | IP RSTN | 35.2 | 35.6 | 2.00 | 1.66 | 0.53 |
| MICHOACAN, MEXICO AFTERSHOCK | | | Sept. 21, 1985 $M_W=7.6$ | | | subduction thrust |
| GRFO | SP SRO | 90.5 | 36.7 | 1.32 | 1.91 | 0.25 |
| ZOBO | SP ASRO | 47.3 | 133.8 | 0.25* | 1.72 | 0.41 |
| HON | SP DWWSSN | 53.0 | 283.7 | 0.54 | 1.75 | 0.38 |
| TOL | SP DWWSSN | 84.4 | 50.0 | 1.38 | 1.89 | 0.27 |
| LON | IP DWWSSN | 33.3 | 334.4 | 1.03 | 1.64 | 0.56 |
| COL | IP DWWSSN | 56.2 | 338.3 | 1.04 | 1.77 | 0.37 |
| SCP | IP DWWSSN | 30.7 | 36.9 | 1.99 | 1.63 | 0.61 |
| KEV | IP DWWSSN | 85.5 | 15.8 | 1.32 | 1.89 | 0.27 |
| GDH | IP DWWSSN | 59.3 | 18.0 | 1.70 | 1.78 | 0.36 |
| BDF | IP DWWSSN | 62.6 | 118.9 | 0.45* | 1.80 | 0.35 |
| AFI | IP DWWSSN | 76.0 | 250.2 | 1.07 | 1.86 | 0.30 |
| RSNT | IP RSTN | 45.5 | 351.6 | 1.40 | 1.71 | 0.42 |
| RSON | IP DWWSSN | 33.6 | 9.1 | 1.78 | 1.65 | 0.56 |
| RSNY | IP DWWSSN | 35.0 | 34.6 | 1.97 | 1.65 | 0.53 |
| PLAYA AZUL, MEXICO Oct. 25, 1981 $M_W=7.3$ | | | | | | subduction thrust |
| BOCO | SP SRO | 30.5 | 112.6 | 0.51 | 1.63 | 0.61 |
| GRFO | SP SRO | 90.6 | 36.6 | 1.33 | 1.91 | 0.25 |
| KONO | SP ASRO | 84.9 | 28.24 | 1.43 | 1.89 | 0.27 |
| SCP | SP DWWSSN | 30.8 | 37.5 | 1.95 | 1.63 | 0.61 |
| LON | SP DWWSSN | 32.9 | 334.7 | 1.55 | 1.64 | 0.57 |
| KEV | SP DWWSSN | 85.3 | 15.7 | 1.44 | 1.89 | 0.27 |
| BER | SP DWWSSN | 82.7 | 28.5 | 1.46 | 1.88 | 0.28 |
| PETATLAN, MEXICO Mar. 14, 1979 $M_W=7.6$ | | | | | | subduction thrust |
| GRFO | SP SRO | 90.6 | 36.8 | 1.34 | 1.91 | 0.25 |
| ZOBO | SP ASRO | 47.0 | 133.7 | 0.43* | 1.72 | 0.41 |
| OAXACA, MEXICO Nov. 29, 1978 $M_W=7.6$ | | | | | | subduction thrust |
| GRFO | SP SRO | 90.4 | 37.6 | 1.33 | 1.91 | 0.25 |
| ZOBO | SP ASRO | 44.0 | 135.0 | 0.31* | 1.70 | 0.43 |
| KONO | SP ASRO | 85.4 | 28.9 | 1.40 | 1.89 | 0.27 |
| VALPARAISO, CHILE Mar. 16, 1985 $M_W=8.0$ | | | | | | subduction thrust |
| SCP | SP DWWSSN | 74.0 | 355.3 | 0.73 | 1.84 | 0.30 |
| JAS | SP DWWSSN | 84.0 | 323.4 | 0.83 | 1.89 | 0.27 |
| LON | IP DWWSSN | 91.5 | 328.2 | 0.83 | 1.91 | 0.25 |
| SLR | IP DWWSSN | 84.1 | 117.0 | 1.34 | 1.89 | 0.27 |
| BDF | IP DWWSSN | 27.9 | 57.2 | 1.79 | 1.61 | 0.65 |
| RSSD | IP RSTN | 82.4 | 337.2 | 0.76 | 1.88 | 0.28 |
| RSNY | IP RSTN | 77.5 | 358.1 | 0.75 | 1.86 | 0.29 |
| RSON | IP RSTN | 86.0 | 346.4 | 0.77 | 1.89 | 0.27 |

Included in the average are the 1985 Michoacan, 1985 Valparaiso, Chile, 1983 Akita-Oki, 1983 Costa Rica, 1983 North Chile, 1982 Tonga, and 1980 Santa Cruz earthquakes. Relative to the average source spectrum, the spectrum of the Michoacan event is enriched at 30 s and depleted at 1 to 10 s. This observation suggests that the high accelerations in Mexico City are not a source effect. The spectra of the Sept. 21 aftershock, 1981 Playa Azul, 1979 Petatlan, and 1978 Oaxaca events follow a trend similar to that of the Michoacan event. This spectral character may be typical of earthquakes in the Mexican subduction zone.

### 3.3 Source Time Functions

We performed a least-squares inversion of the broadband records of the Michoacan earthquake and its Sept. 21 aftershock to obtain the source time functions using the method of Hartzell and Heaton (1985). In this method, a finite fault is approximated by a sum of point sources distributed over the depth range of the fault. We used three sources at 10, 20, and 30 km depth. For each depth k, we computed a Green's function $G_k(t)$ by convolving the sum of delta functions representing the depth phases (P + pP + sP) with the instrument response. The timing and amplitudes of the depth phases depend on the focal mechanism and the velocity structure above the source; we used the focal mechanism of Eissler et al. (1986) used above and used a halfspace with a P-velocity of 6.4 km/s and an S-velocity of 3.5 km/s. If $F_k(t)$ is the teleseismic time function for the $k^{th}$ depth, then the time function of the entire

earthquake is $\sum_k F_k(t)$. $F_k(t)$ is determined by matching $\sum_k F_k(t) * G_k(t)$ to the observed seismogram using the method of least squares, while constraining $F_k(t)$ to be positive.

Figure 3.4 shows time functions determined from 12 broadband GDSN records. The records are of much higher quality than those used in previous modeling studies and are filtered to retain all frequencies lower than 1 Hz. The beginning of each time function corresponds to 1 s before JB time. The short-period ASRO station ZOB is included because the station distribution to the south is rather sparse. For ZOB, we deconvolved the short-period ASRO response and convolved in the broadband DWWSSN response. To obtain a good match to the other time functions, however, we had to reverse its polarity. Although ZOB is located close to the nodal line, the apparent polarity reversal is probably not due to a change in the mechanism during faulting. We could not match the unreversed record with changes in the mechanism within the range of uncertainty. The ZOB time function is, therefore, considered tentative.

Three source pulses are evident in Figure 3.4. We interpret these to be events on the fault plane. The first two source pulses are similar in moment and time width (15 s), and occur about 25 s apart. The existence of two such events is consistent with the near-field strong motions (Anderson et al., 1986). The phase PP obscures part of the third pulse on the closest stations (LON, RSON, and SCP), but it can be clearly seen on RSNT and GDH. It contains only 20% of the moment of the first pulse, and occurs about 50 s after the first. A third event cannot be seen clearly on the strong motions. The moment determined from these broadband records averages about 30% of the

SOURCE TIME FUNCTIONS OF THE 1985 MICHOACAN, MEXICO EARTHQUAKE

Figure 3.4. Source time functions for the 1985 Michoacan earthquake obtained from broadband records. The focal mechanism and stations used in the inversions are shown. Directivity is evident in the timing between the first and second source pulses.

total moment determined from 256 s surface waves.

We also inverted several records of the Sept. 21 aftershock for a source time function, using the same focal mechanism that we used for the mainshock. The aftershock time function consists of a 15 s wide pulse, similar to one of the mainshock pulses.

The mainshock time functions in Figure 3.4 clearly show directivity; the two large pulses are separated by 30 s for the northwestern stations (COL, LON, AFI) and by 20 s for the southern stations (BDF, ZOB). Table 2 lists the time differences measured at each station between the peaks of the three pulses. We performed a least-squares nonlinear estimation to determine the strike, distance, and time (at the source) between them. The locations thus obtained are shown in Figure 3.1, where we arbitrarily located the first event at the earthquake's epicenter and ignored the dip of the slab. The shaded areas on Figure 3.1 show the inferred rupture zones of the three events, assuming a rupture velocity of 2.5 km/s and event rise times of 10 s, 10 s, and 7 s. The second event occurs 26 ±0.4 s after the first, and 82 ±7.5 km southeastward of it. The apparent rupture velocity from the first to the second event is then 3.2 km/s. The relative location of the third source event is less well-constrained; the third pulse might represent simultaneous radiation from two or more parts of the fault plane. If it represents just one event, the third event occurs 47 ±1.0 s after the first, and about 35 to 50 km seaward of the second. Rupture velocities between the first and third or second and third events are about 2.5 km/s.

For comparison Figure 3.5 shows inversions of the available broadband records of the 1985 Valparaiso, Chile earthquake. The very different nature of
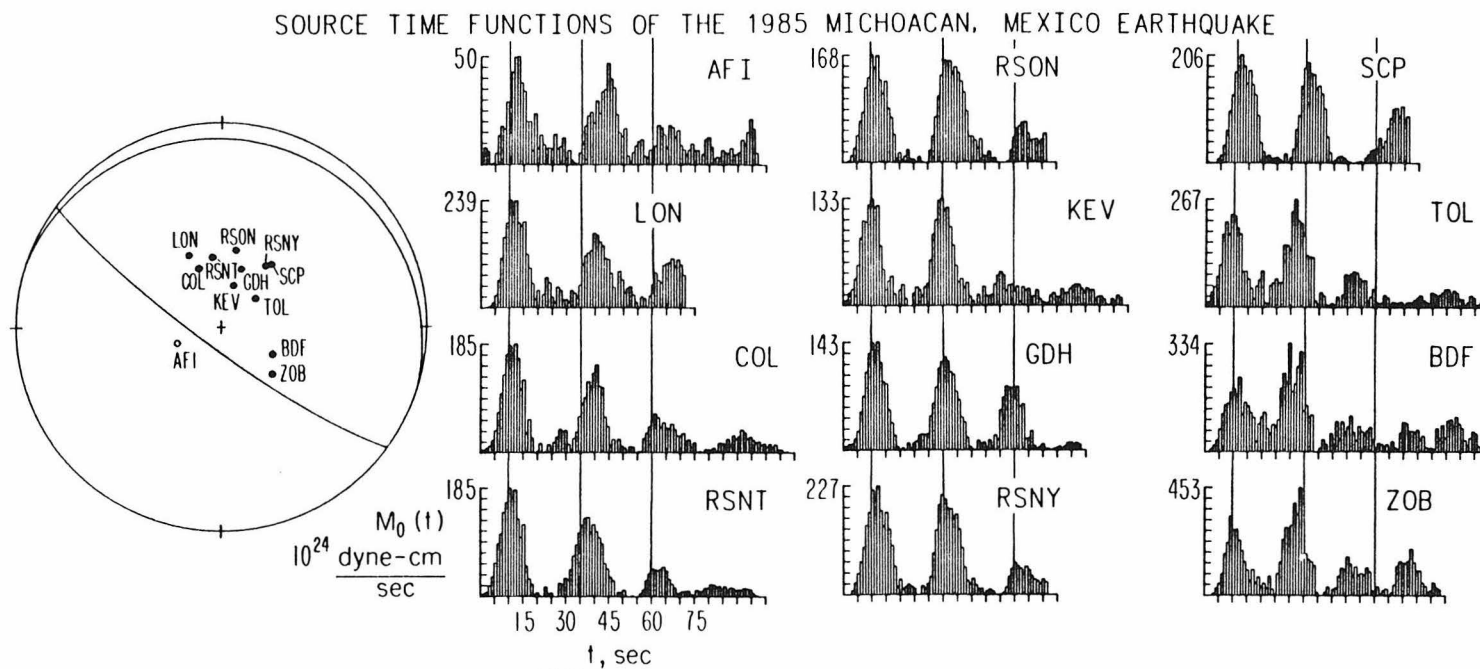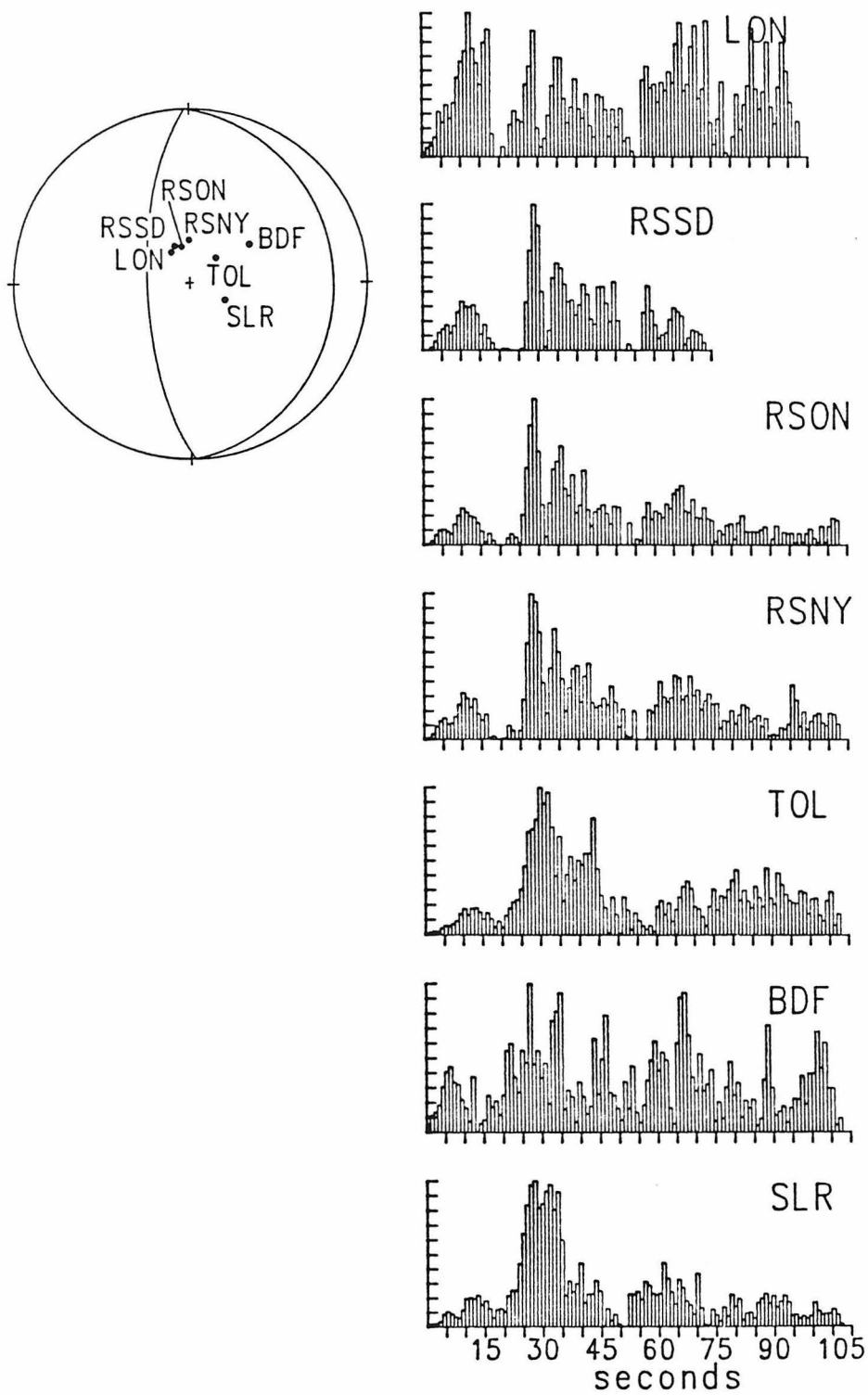
Figure 3.5. Source time functions for the 1985 Valparaiso earthquake obtained from broadband records. The focal mechanism and stations used in the inversions are shown.

Table 2:  Times between Pulses in the Source Time Functions
of the Michoacan, Mexico Earthquake

| Station | Azimuth (deg) | $t_{12}$ (sec) | $t_{23}$ (sec) | $t_{13}$ (sec) |
|---------|---------------|----------------|----------------|----------------|
| AFI  | 249.9 | 30.0 | 21.0 | 53.0 |
| LON  | 335.2 | 30.0 | 26.5 | 56.0 |
| COL  | 338.5 | 29.0 | 24.0 | 51.5 |
| RSNT | 352.1 | 27.0 | 24.0 | 52.0 |
| RSON | 10.2  | 27.0 | 25.0 | 51.5 |
| KEV  | 15.6  | 25.0 | 20.5 | 45.5 |
| GDH  | 18.2  | 25.0 | 23.0 | 48.5 |
| RSNY | 35.6  | 25.0 | 25.0 | 50.0 |
| SCP  | 38.1  | 24.0 | 26.0 | 50.0 |
| TOL  | 49.7  | 23.0 | 20.0 | 43.0 |
| BDF  | 118.5 | 20.0 | 18.5 | 40.0 |
| ZOBO | 133.2 | 21.0 | 18.5 | 41.0 |

$t_{12}$ is the time between the $1^{st}$ and $2^{nd}$ source pulses.

$t_{23}$ is the time between the $2^{nd}$ and $3^{rd}$ source pulses.

$t_{13}$ is the time between the $1^{st}$ and $3^{rd}$ source pulses.

the rupture processes between the Michoacan and Valparaiso earthquakes is immediately obvious.

## 3.4 Discussion

Large subduction earthquakes along the Mexican trench usually consist of one simple source on time-scales longer than 10 s (Chael and Stewart, 1982; Astiz and Kanamori, 1984; Singh et al., 1984). The Michoacan earthquake is composed mainly of two simple sources separated by about 80 km. Most of the moment release (e.g., displacement) came first from a region northwest of the rupture zone of the 1981 Playa Azul earthquake, and then 26 s later from a region southeast of that zone. The rupture zone of the 1981 Playa Azul earthquake, therefore, can be interpreted as a previously failed asperity that had not been loaded much since failure. Perhaps the rupture propagated from the first to the second source with relatively high velocity 3.2 km/s, because it did little or no work rebreaking the 1981 rupture zone. The Sept. 21 aftershock extended the rupture further south.

In order to compare the two largest earthquakes of 1985, we analyzed GDSN records of the March 3, 1985 Valparaiso, Chile earthquake ($M_W = 8.0$) along the Chile trench. The Valparaiso earthquake's moment rate spectrum and source time functions are shown in Figures 3.3 and 3.5, respectively. The Michoacan records, spectrum, and time functions contain less high-frequency radiation than those of the 1985 Valparaiso, Chile earthquake. As shown schematically in Figure 3.6, the Michoacan earthquake ruptured two relatively

1985 VALPARAISO, CHILE     1985 MICHOACAN, MEXICO

ASPERITY DISTRIBUTION

SOURCE TIME FUNCTIONS

Figure 3.6. Schematic comparison of records and time functions at two RSTN stations, and inferred asperity distributions for (a) the 1985 Valparaiso, Chile earthquake and (b) the 1985 Michoacan, Mexico earthquake.

smooth, strong patches which generated large 30 s waves, but small 1 to 10 s waves. This behavior contrasts with that of the Valparaiso event which had a more complex rupture process and generated more 1 to 5 s energy. These differences between the two earthquakes discerned from teleseismic records can also be seen in the near-field strong motions. Figure 3.7 shows that for a given distance, except at Mexico City, the near-field peak accelerations are significantly higher for the Valparaiso earthquake than for the Michoacan earthquake (Anderson et al., 1986). Admittedly, most of the peak accelerations occur at frequencies greater than 1 Hz (except at Mexico City). Also, the Mexican accelerographs are generally sited on hard rock (except at Mexico City), while some of the Chilean instruments are not (Anderson et al., 1986). Nevertheless, the large systematic difference suggests that the anomalously high accelerations in Mexico City are not a source effect. This conclusion is consistent with the teleseismic source spectra of the two earthquakes.

From Figure 3.3 a relative lack of high frequencies appears to characterize earthquakes along the Mexican trench, if recent large events are typical. This spectral character, which implies relative smoothness at scale-lengths of 3 to 30 km, may be typical of the Mexican subduction zone. This is also consistent with the relative lack of aftershocks of Mexican subduction earthquakes (Singh and Suarez, 1985). The cause must lie in the nature of the interplate coupling, which may reflect a relative lack of relief on the seafloor or conditions at the subduction thrust interface, such as subduction of sediments or high pore pressure.

Figure 3.7.  A comparison of peak accelerations vs. distance to the rupture plane for the strong motions of the 1985 Michoacan, Mexico and 1985 Valparaiso, Chile earthquakes (after Anderson et al., 1986).
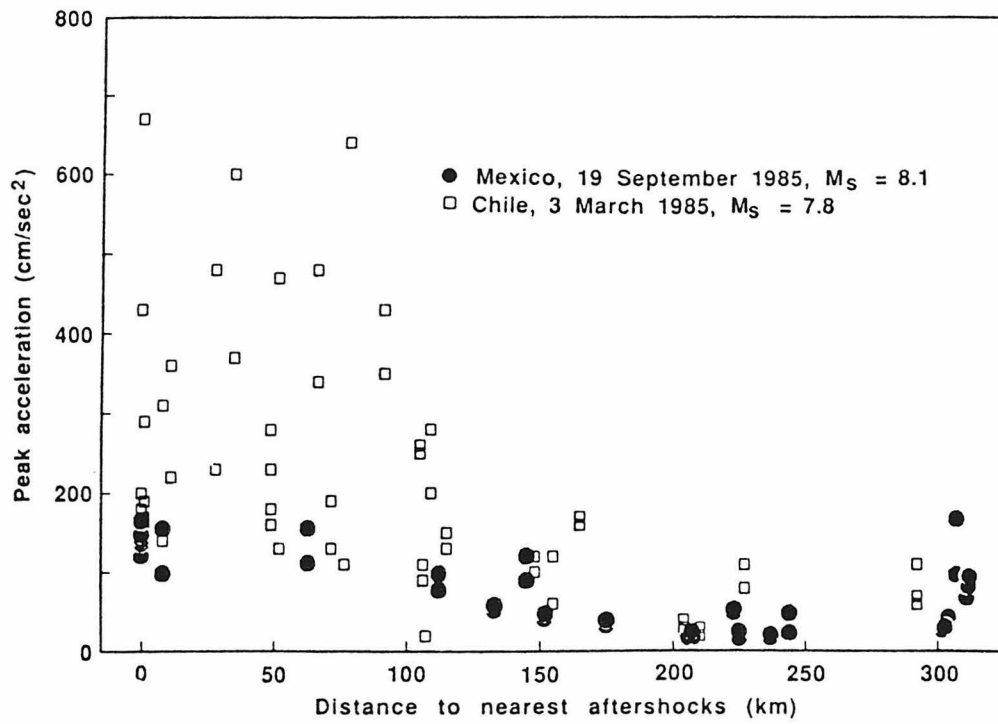
### 3.5 Conclusions

The Michoacan earthquake source spectrum is enriched at 30 s and depleted at 1 to 10 s relative to the average source spectrum of large interplate subduction events. Source spectra for the Sept. 21 aftershock, 1981 Playa Azul, 1979 Petatlan, and 1978 Oaxaca events follow a trend similar to that of the 1985 Michoacan event. This spectral character, which implies relative smoothness at scale-lengths of 3 to 30 km, may be typical of the Mexican subduction zone.

A station by station least-squares inversion for the source time function of the Michoacan earthquake yields three source pulses. The first two are similar in moment and occur 26 s apart. The variation from station to station of their separation in time indicates that a second source event originated about 80 km to the southeast of the first, implying southeastward rupture along the trench. The third pulse contains only 20% of the moment of the first.

The mainshock records, spectrum, and time functions contain less high-frequency radiation than those of the 1985 Valparaiso, Chile earthquake. The Michoacan earthquake ruptured two relatively smooth, strong patches which generated large 30 s waves, but small 1 to 10 s waves. This behavior contrasts with the 1985 Valparaiso event which had a more complex rupture process and generated more 1 to 5 s energy. Consistent with this are the higher near-field accelerations recorded during the Valparaiso earthquake compared to the lower accelerations generated by the Michoacan earthquake (except at Mexico City). The striking consistency of the near-field and teleseismic data for the Michoacan and Valparaiso earthquakes shows that broadband teleseismic data

are useful in characterizing strong motions from large and great earthquakes.

This study indicates that the relatively high accelerations in Mexico City were not a source effect, that is, were not due to an unusually intense source (for $M_W = 8.0$); however, the extended duration of shaking due to the multiple sources was responsible for much of the damage.

## 3.6 References

Anderson, J. G., P. Bodin, J. N. Brune, J. Prince, S. K. Singh, R. Quaas, and M. Onate, Strong ground motion from the Michoacan, Mexico earthquake, *Science, 233*, 1043-1049, 1986.

Astiz, L., and H. Kanamori, An earthquake doublet in Ometepec, Guerrero, Mexico, *Phys. Earth Planet. Interiors, 34*, 24-45, 1984.

Chael, E., and G. Stewart, Recent large earthquakes along the Middle American trench and their implications for the subduction process, *J. Geophys. Res., 87*, 329-338, 1982.

Eissler, Astiz, and Kanamori, Tectonic setting and source parameters of the September 19, 1985 Michoacan, Mexico earthquake, *Geophys. Res. Lett., 13*, 569-572, 1986.

Hartzell, S. H., and T. H. Heaton, Teleseismic time functions for large, shallow subduction zone earthquakes, *Bull. Seism. Soc. Am., 75*, 965-1004, 1985.

Houston, H., and H. Kanamori, Source spectra of great earthquakes: teleseismic constraints on rupture process and strong motion, *Bull. Seism. Soc. Am., 76*, 19-42, 1986.

Singh, S. K., T. Dominguez, R. Castro, and M. Rodriguez, P-waveform of

large, shallow earthquakes along the Mexican subduction zone, *Bull. Seism. Soc. Am.*, *74*, 2135-2156, 1984.

Singh, S. K., and G. Suarez, Regional variations in the number of aftershocks of large subduction zone earthquakes (abstract), *EOS, 66*, 958, 1985.

# Chapter 4

## Broadband Rupture Process of 4 Large Subduction Zone Earthquakes:
## Spatial Distribution of Seismic Moment Release

## Abstract

Time functions and rupture processes of 4 recent large subduction zone earthquakes are determined from broadband teleseismic GDSN records using the iterative inversion technique of Kikuchi and Fukao. The method inverts the records simultaneously by determining the location, time, and seismic moment of a single point source that best explains the records, then subtracting the synthetics for that point source from the records, and repeating the procedure for the residual records. Using this technique with the high-quality GDSN intermediate-band records provides more details of the rupture process than have been obtained previously.

The inversion produces maps of spatial and temporal distribution of seismic moment release at periods of 3 to 30 sec for the 1985 Michoacan, Mexico ($M_W$=8.0), 1983 Akita-Oki, Japan ($M_W$=7.8), 1985 Valparaiso, Chile ($M_W$=8.0), and 1986 Andreanof Islands, Alaska ($M_W$=8.0) earthquakes. The events are listed in order of increasing complexity of the rupture process. Comparing the source spectra of these events, computed from GDSN records, yields complementary information at periods of 1 to 30 sec. The Michoacan event had the simplest pattern. It ruptured two large smooth patches, generating relatively little 1 to 10 sec energy. The Akita-Oki event had two main patches of moment release - the first near the hypocenter, and the second 25 sec later about 50 km north. Some moment release was distributed irregularly and substantial 1 to 10 sec energy was generated. The Valparaiso event ruptured outward and southward from the hypocenter, with smaller but stronger patches which generated 1 to 10 sec energy distributed over the fault plane. The Andreanof Islands event had some clustering of moment release near the hypocenter at 10 to 20 sec and roughly 90 km west at 30 to 50 sec, but much activity was diffuse.

## 4.1 Introduction

In Chapter 3, I inferred the spatial distribution of seismic moment release of the 1985 Michoacan earthquake by obtaining a moment release time function for each teleseismic station and comparing the timing of features of the time functions to the azimuth of the station. Because picking features of time functions is rather subjective, it is preferable to invert all the available and relevant records of an earthquake simultaneously, rather than individually. Using the full least-squares approach that I used for individual stations in Chapter 3 for all the stations simultaneously would require many hours of computer time. A more computationally feasible approach is to use an iterative technique. In this chapter, I determine time functions and spatial distribution of moment release for 4 recent large subduction zone earthquakes from broadband teleseismic Global Digital Seismic Network (GDSN) records using the iterative inversion technique of Kikuchi and Fukao (1986). Using this technique with high-quality GDSN intermediate-band records provides more details of the rupture process than have been obtained previously. In the next chapter I will relate the rupture process to the strong motions.

## 4.2 Inversion Method

The inversion technique was developed by Kikuchi and Kanamori (1982, 1986), extended by Kikuchi and Fukao (1985) to locate subevents on a 2-dimensional fault plane, and applied to WWSSN LP records of 9 large

earthquakes by Kikuchi and Fukao (1986). The method inverts the records simultaneously by determining the location, time, and moment of a single point source that best explains the records, then subtracting the synthetics for that point source from the records, and repeating the procedure for the residual records. A time function and map of spatial distribution of moment release are obtained from the sum of the point sources. The location of the point source can vary over a specified 2-dimensional dipping grid that represents the fault plane. In the calculations of the synthetic seismograms due to a point source, the depth phases (pP and sP), radiation pattern, geometrical spreading, and instrument response are included. We specify one trapezoidal time function and focal mechanism to be used for all the point sources. Judgement is required to choose the duration of the trapezoid and the number of iterations (i.e., number of point sources) appropriate to the particular records that one is trying to invert. The moment of each point source is required to be positive. Thus, point sources of long duration can fit only long period features of the waveforms, whereas point sources of short duration can fit both long and short period features of the waveforms, although many point sources (or iterations) may be required to fit long period features. Hence, point sources with a shorter duration resolve more details of the temporal and spatial distribution of moment release. Of course, the usual trade-off of resolution vs. stability applies here. The shortest period that one wants to fit in the seismograms dictates the duration of the trapezoidal time function of the point source. The question of when to stop iterating (e.g., adding more point sources) has not been adequately resolved. One solution is to iterate until the error between the data and the synthetics is lower than a chosen

level. This level, however, would have to be different for different data sets, as some are larger or inherently more inconsistent than others. In the following work, the number of iterations has been chosen by trial, error and intuition.

## 4.3 Results of the Inversions

Table 1 lists the earthquakes, records, station types, distances, and azimuths of the data I used in the inversions. I equalized the data sets by deconvolving the various instrument responses of the digital records (see Table 1) and then convolving with a Benioff 1-90 instrument response which has a broadband response (1 to 30 seconds). Care was required in the deconvolution of the instrument response to retrieve periods of 30 seconds from short period digital records. Periods shorter than 3 seconds were filtered out. All records are vertical, teleseismic P-wave seismograms. At the relatively short periods examined here, the horizontal component of the P-wave is frequently larger than theoretically expected (presumably, this is due to scattering), so it is not advisable to use horizontal components.

The velocity structures at the source and receiver can be specified, although they are limited to simple forms. At the receiver, a half-space with P-velocity, $v_p$=6.0 km/sec and density, $\rho$=2.6 gm/cm$^3$ is assumed. The source has a 15 km layer with $v_p$=6.5 km/sec and $\rho$=2.8 gm/cm$^3$, over a half-space with $v_p$=7.8 km/sec and $\rho$=3.3 gm/cm$^3$. The fault plane is gridded so that point sources can be located every 10 km along strike and down dip.

## Table 1: Records Used in Inversions

| Station | Type | Δ (deg) | Azimuth (deg) |
|---|---|---|---|
| AKITA-OKI, JAPAN   May 26, 1983   $M_W$=7.8 | | | |
| RSNY | IP RSTN | 90.0 | 23.3 |
| RSNT | IP RSTN | 62.7 | 30.3 |
| RSON | IP RSTN | 77.9 | 31.0 |
| COL | IP DWWSSN | 47.2 | 33.7 |
| RSSD | IP RSTN | 78.4 | 40.9 |
| LON | IP DWWSSN | 67.2 | 47.3 |
| HON | IP DWWSSN | 56.0 | 89.8 |
| AFI | IP DWWSSN | 70.7 | 128.8 |
| TAU | IP DWWSSN | 83.4 | 173.9 |
| BER | IP DWWSSN | 72.6 | 338.0 |
| KEV | IP DWWSSN | 59.6 | 338.1 |
| VALPARAISO, CHILE   Mar. 16, 1985   $M_W$=8.0 | | | |
| BDF | IP DWWSSN | 27.9 | 57.2 |
| SLR | IP DWWSSN | 84.1 | 117.0 |
| LON | IP DWWSSN | 91.5 | 328.2 |
| RSSD | IP RSTN | 82.4 | 337.2 |
| RSON | IP RSTN | 86.0 | 346.4 |
| RSNY | IP RSTN | 77.5 | 358.1 |
| MICHOACAN, MEXICO   Sept. 19, 1985   $M_W$=8.0 | | | |
| RSON | IP RSTN | 33.4 | 10.2 |
| KEV | IP DWWSSN | 85.3 | 15.6 |
| GDH | IP DWWSSN | 59.2 | 18.2 |
| KONO | SP ASRO | 85.0 | 28.1 |
| RSNY | IP RSTN | 35.2 | 35.6 |
| SCP | IP DWWSSN | 31.0 | 38.1 |
| TOL | IP DWWSSN | 84.8 | 49.7 |
| BDF | IP DWWSSN | 63.5 | 118.5 |
| ZOBO | SP ASRO | 48.3 | 133.2 |
| AFI | IP DWWSSN | 75.3 | 249.9 |
| HON | SP DWWSSN | 52.0 | 283.2 |
| LON | IP DWWSSN | 32.6 | 335.2 |
| COL | IP DWWSSN | 55.5 | 338.5 |
| RSNT | IP RSTN | 45.0 | 352.1 |
| ANDREANOF ISLANDS, ALASKA   May 7, 1986   $M_W$=8.0 | | | |
| GDH | SP DWWSSN | 52.2 | 22.7 |
| RSNT | IP RSTN | 33.4 | 47.1 |
| RSNY | IP RSTN | 62.3 | 52.6 |
| RSON | IP RSTN | 48.4 | 56.9 |
| SCP | IP DWWSSN | 63.3 | 57.5 |
| RSSD | IP RSTN | 46.4 | 69.8 |
| LON | SP DWWSSN | 34.4 | 76.5 |
| ANMO | SP SRO | 50.6 | 81.0 |
| HON | IP DWWSSN | 32.8 | 150.1 |
| MAJO | SP ASRO | 36.3 | 264.4 |
| TATO | SP SRO | 54.6 | 266.4 |
| ANTO | SP SRO | 86.0 | 339.0 |
| KONO | SP ASRO | 69.2 | 357.6 |

It is easier to study the spatial rupture process of larger earthquakes because the teleseismic viewing aperture is only a fixed size. That is, the range of take-off angles of teleseismic rays is not very wide (16° to 32°). Larger earthquakes have longer durations so that the trade-off in resolving space and time is minimized. It is this as well as the particular station distribution that limits the spatial resolution of the inversion. The 4 largest earthquakes of 1983 to 1986 are studied here. They are all shallow subduction earthquakes.

In the following descriptions, I refer to a group of point sources clustered in space and time as a subevent, and to a group of point sources clustered in time only as a moment release episode.

## 1985 Michoacan, Mexico Earthquake

In inverting broadband records of this earthquake, I assumed a focal mechanism ($\phi$=288°, $\delta$=10°, $\lambda$=72°). that is similar to that assumed in the previous chapter. The extent of the fault plane was estimated from the aftershock distribution (Stolte et al., 1986, UNAM, 1986). 80 sec of record are inverted. The hypocenter is specified at the appropriate point on the fault plane 17 km deep.

For this earthquake I made many inversions using different durations of trapezoids and two different data sets: the digital records equalized to a 1-90 Benioff response and to a WWSSN long period response. All the source time functions and the spatial distributions of moment release were generally consistent with the results of the single station deconvolutions of the previous

chapter, thus lending credence to this inversion. That is, the Michoacan earthquake consisted mainly of two subevents of the same moment and duration separated by about 80 km and 25 sec. These subevents are considered to be asperities on the fault surface.

Figures 4.1, 4.2, and 4.3 show the results of an inversion of the WWSSN LP type records. Figure 4.1 compares the data to the synthetics. Only four iterations substantially explain the data since the trapezoid was chosen to correspond to one of the pulses of moment release in Figure 3.4 (in this case, rise time $\tau_1 = 9$ sec and duration $\tau_2 = 10$ sec). Figures 4.2a and b show the source time function and the initiation times of the point sources. The time function is obtained by convolving Figure 4.2b with the trapezoidal time function of each point source. Figure 4.3 shows a map of moment release on the fault plane. Each point source is represented by a circle whose area was obtained from Kanamori and Anderson's (1975) empirical relation between seismic moment and rupture area (estimated from aftershocks) for earthquakes:

$$M_0 \approx \xi \, S^{3/2} \, ,$$

where $M_0$ is the moment in dyne-cm, S is the area in $cm^2$, and $\xi = 1.23 \times 10^7$ dyne/$cm^2$. Since the point sources here are only part of a larger earthquake, and may, therefore, experience different boundary conditions from the complete earthquake, it may not be strictly correct to apply the above relation. Nonetheless, the size of the circle gives some estimate of the area ruptured by the point source.

Figure 4.1. The 1985 Michoacan, Mexico earthquake. Comparison of data (top line) and synthetics (bottom line) from the inversion of GDSN records equalized to a long period WWSSN response. Peak record amplitude is given in cm (e.g., gain is 1).

Figure 4.2. (a). The 1985 Michoacan, Mexico earthquake. Source time function obtained after 4 iterations. The trapezoidal time function of each point source has rise time $\tau_1 = 9$ sec and duration $\tau_2 = 10$ sec. Peak moment release rate is given in units of $10^{25}$ dyne-cm/sec. (b). The timing of the initiation of each point source.



Figure 4.3. The 1985 Michoacan, Mexico earthquake. Spatial distribution of moment release. Each point source is represented by a circle. The area of the circle estimates the rupture area of the source. The number in each circle gives the initiation time in seconds of the source. Note the orientation of the fault plane. The trench is located towards the top of the figure. An asterisk at (0,0) marks the hypocenter.

One can achieve considerably better resolution, however, by inverting the broadband data set which contains shorter periods. Figures 4.4, 4.5, 4.6, and 4.7 show the results of an inversion of the Benioff 1-90 type records using a trapezoid with $\tau_1=2$ sec and $\tau_2=3$ sec and 50 iterations (e.g., 50 point sources). Again the result is substantially similar to what we have seen before: two subevents 90 km and 25 sec apart. The time function shows a period of no moment release between 21 and 29 sec and the map of moment release shows a region between the first and second subevents that is devoid of moment release. Thus it appears that waves of periods 3 to 30 seconds were not generated in the aftershock zone of the 1981 Playa Azul earthquake. This may help constrain physical properties of the rupture process and the fault plane. It is not clear whether longer periods were generated as has been suggested by Ekstrom and Dziewonski (1986, Figures 3 and 4). The apparent third subevent found in the previous chapter (see Figures 3.1 and 3.4) is reduced in moment and spatially diffuse since point sources locate at both ends of the fault plane during the third pulse of moment release (55 to 65 sec).

It would be interesting to know whether the rupture progressed outward from an initial point or unilaterally across the asperity. Figure 4.7 shows time slices of 3 sec each of the rupture of the two asperities. Apparently, the first asperity broke from the center outward, while the second broke essentially unilaterally to the south-east. This corresponds to what might be expected intuitively.
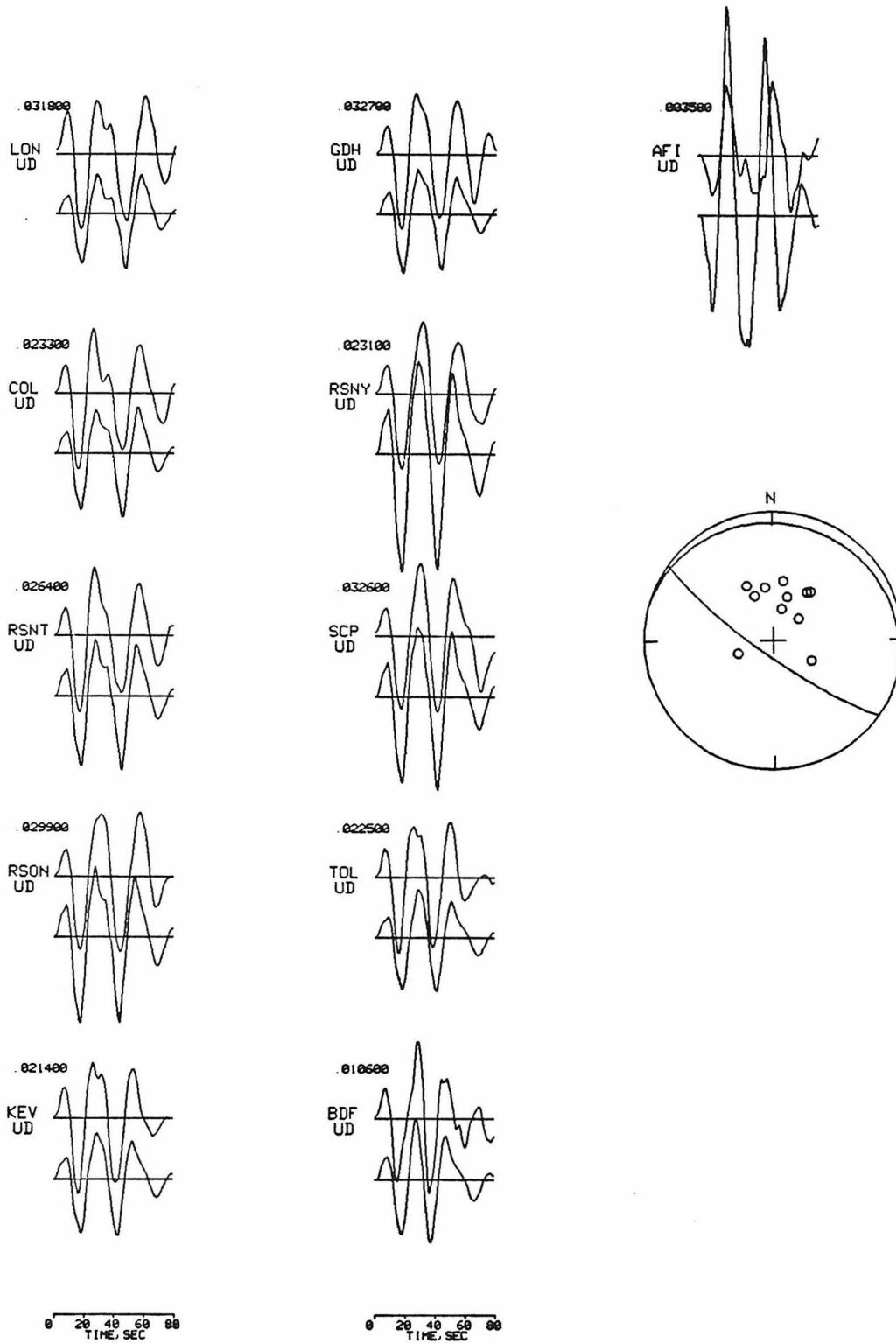
Figure 4.4. The 1985 Michoacan, Mexico earthquake. Comparison of data (top line) and synthetics (bottom line) from the inversion of GDSN records equalized to a broadband Benioff response. Peak record amplitude is given in cm (e.g., gain is 1).

24.8



Figure 4.5. (a). The 1985 Michoacan, Mexico earthquake. Source time function obtained after 50 iterations. The trapezoidal time function of each point source has rise time $\tau_1 = 2$ sec and duration $\tau_2 = 3$ sec. Peak moment release rate is given in units of $10^{25}$ dyne-cm/sec. (b). The timing of the initiation of each point source.
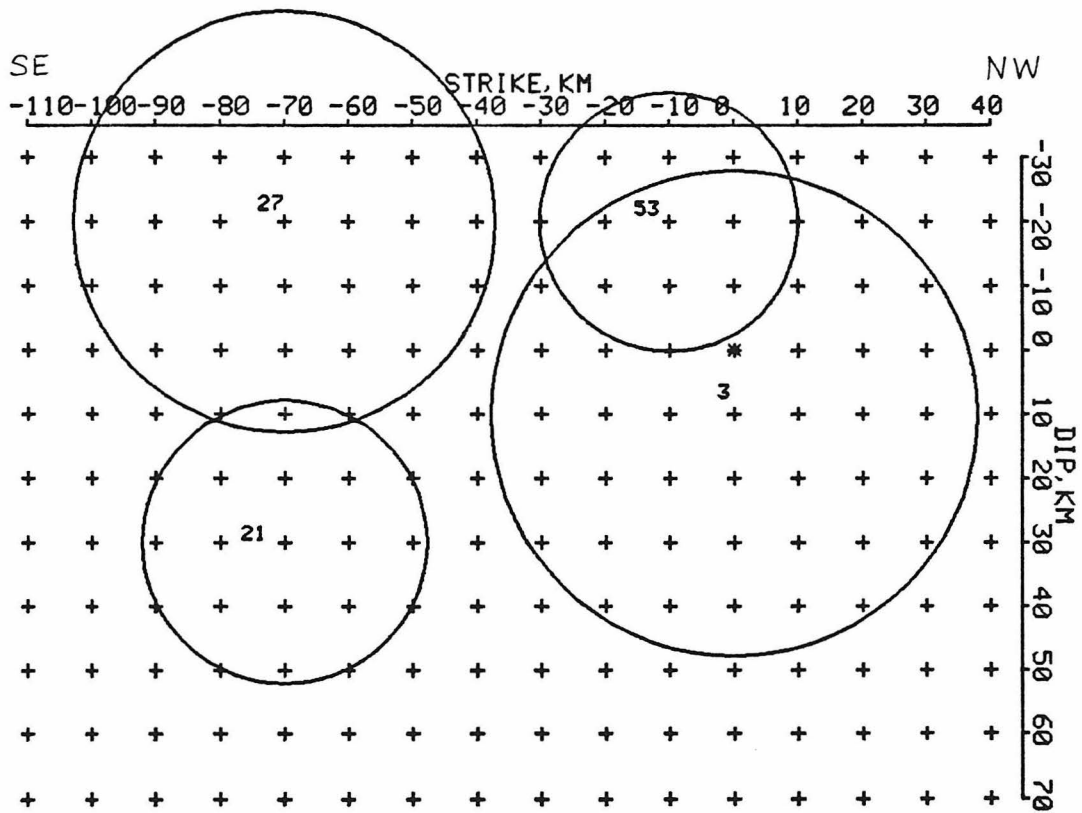


Figure 4.6. The 1985 Michoacan, Mexico earthquake. Spatial distribution of moment release. Each point source is represented by a circle. The area of the circle estimates the rupture area of the source. The moment releases represented by each circle are summed up over 80 sec. Shading is proportional to the moment release per unit area. Note the orientation of the fault plane. The trench is located towards the top of the figure. An asterisk at (0,0) marks the hypocenter.

Figure 4.7. The 1985 Michoacan, Mexico earthquake. Spatial distribution of moment release displayed in time windows of 3 sec durations. Each point source is represented by a circle. The area of the circle estimates the rupture area of the source. The number in each circle gives the initiation time in seconds of the source. No point source initiates between 17 and 29 sec. Note the orientation of the fault plane. An asterisk marks the hypocenter.

## 1985 Valparaiso, Chile Earthquake

For this event I used the focal mechanism from Zhang (personal communication) ($\phi=5.6°$, $\delta=24°$, $\lambda=96°$). The extent of the fault plane was estimated by extending the dipping thrust plane down to 60 km depth. 80 sec of record are inverted. The hypocenter is placed at 35 km depth (Christiansen and Ruff, 1986, Zhang, personal communication).

Figures 4.8, 4.9, 4.10, and 4.11 show the results of an inversion of the Benioff 1-90 type records using a trapezoid with $\tau_1=2$ sec and $\tau_2=3$ sec and 50 iterations. The number and distribution of stations is not as good as for the other events. The time function (Figure 4.9) shows a small episode of moment release (0 to 10 sec), then a hiatus, then the main episode of moment release (20 to 40 sec), then another hiatus, then a final episode of moment release (55 to 75 sec). The time function is consistent with those obtained by the single station deconvolutions of Chapter 3 (see Figure 3.5). The main moment release occurs between 20 and 40 sec with rupture progressing outward from the hypocenter and generally to the south (Figure 4.11). Our result is also consistent, spatially and temporally, with that of Christiansen and Ruff (1986, Figure 7) from long-period WWSSN records, although our data naturally has much more short-period detail.
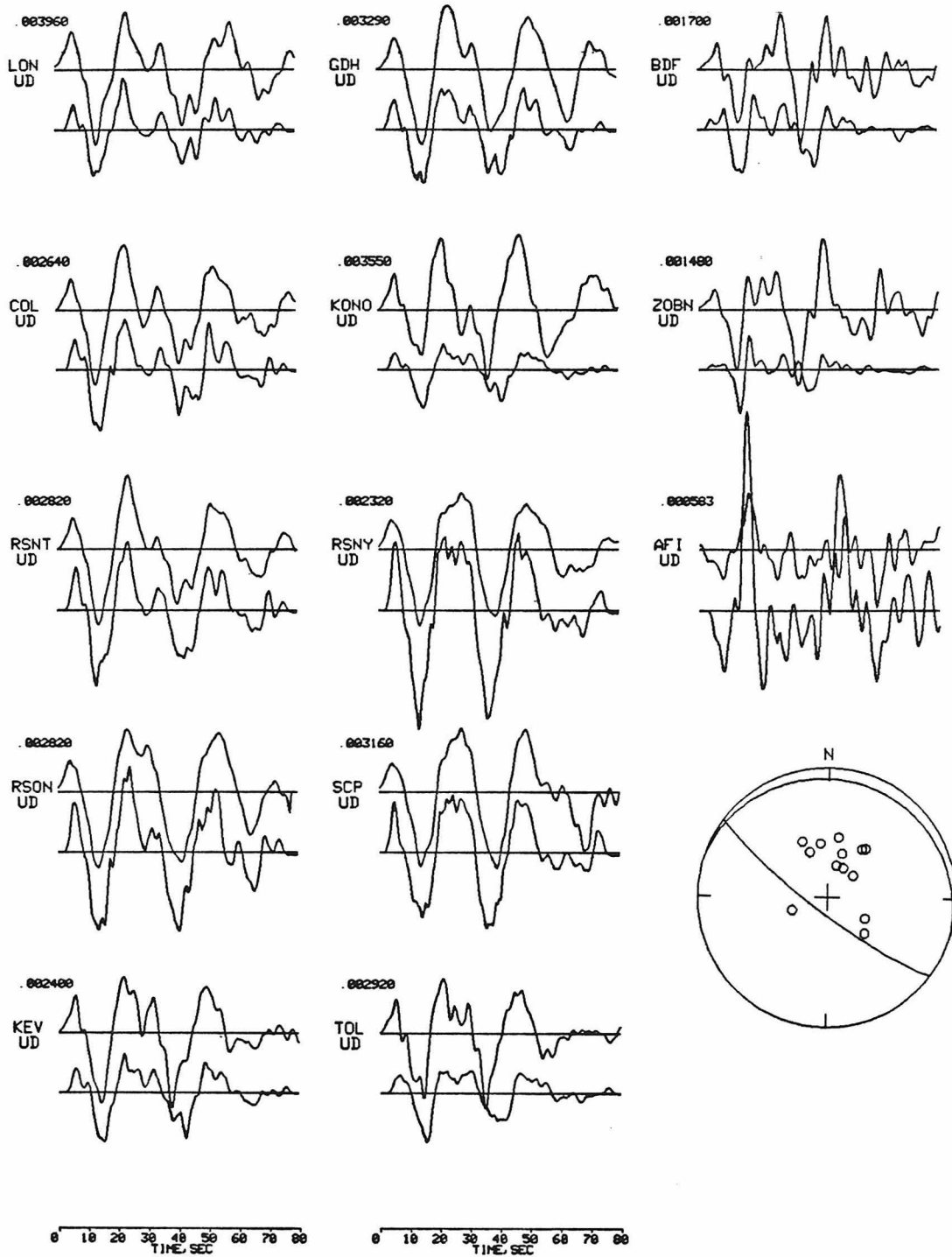
Figure 4.8. The 1985 Valparaiso, Chile earthquake. Comparison of data (top line) and synthetics (bottom line) from the inversion of GDSN records equalized to a broadband Benioff response. Peak record amplitude is given in cm (e.g., gain is 1).
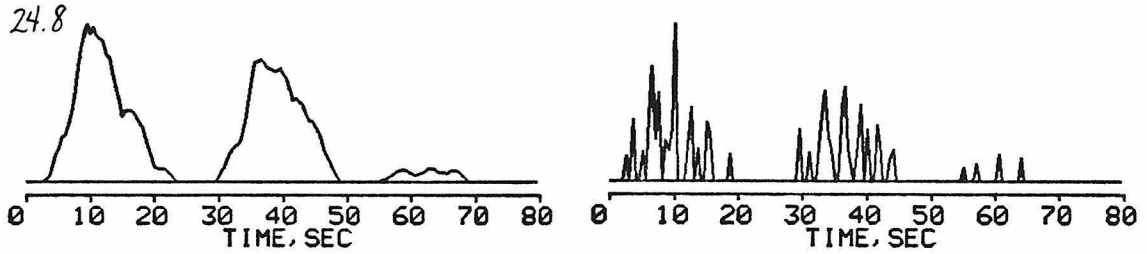
28. 1



Figure 4.9. The 1985 Valparaiso, Chile earthquake. Source time function obtained after 50 iterations. The trapezoidal time function of each point source has rise time $\tau_1=2$ sec and duration $\tau_2=3$ sec. Peak moment release rate is given in units of $10^{25}$ dyne-cm/sec. (b). The timing of the initiation of each point source.
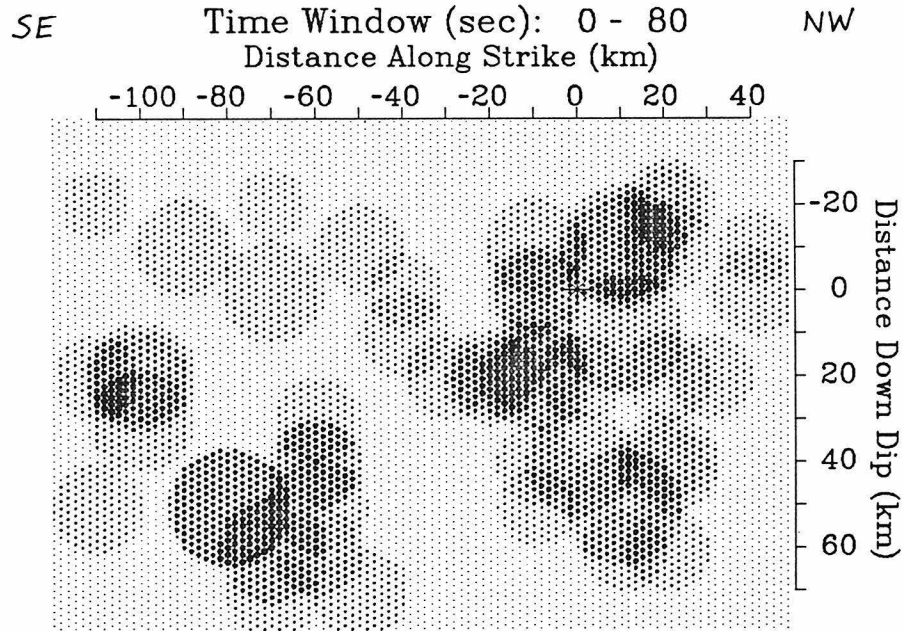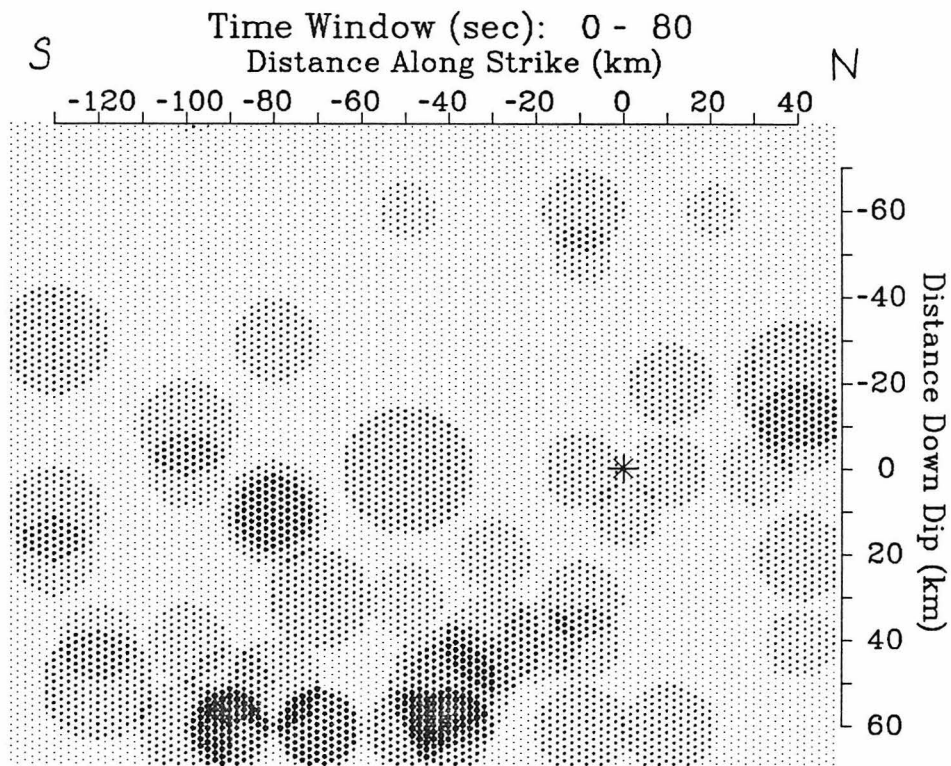


Figure 4.10. The 1985 Valparaiso, Chile earthquake. Spatial distribution of moment release. Each point source is represented by a circle. The area of the circle estimates the rupture area of the source. The moment releases represented by each circle are summed up over 80 sec. Shading is proportional to the moment release per unit area. Note the orientation of the fault plane. The trench is located towards the top of the figure. An asterisk marks the hypocenter.
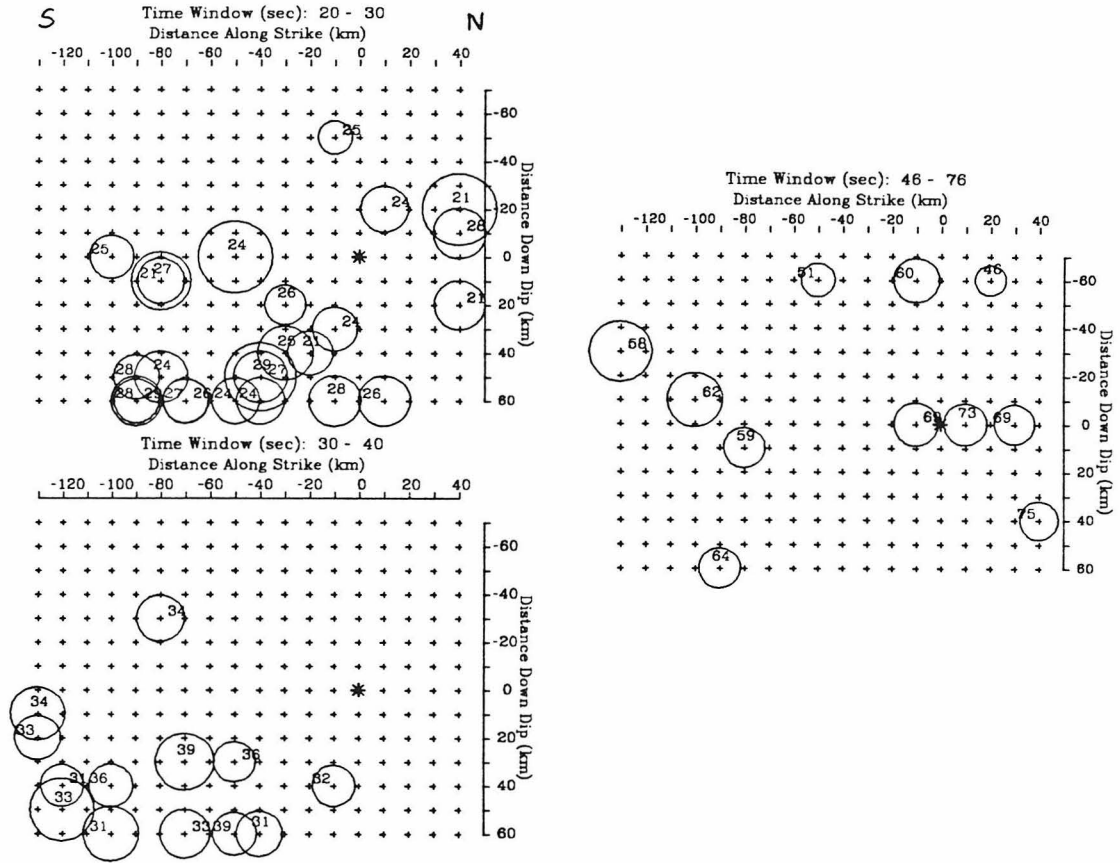
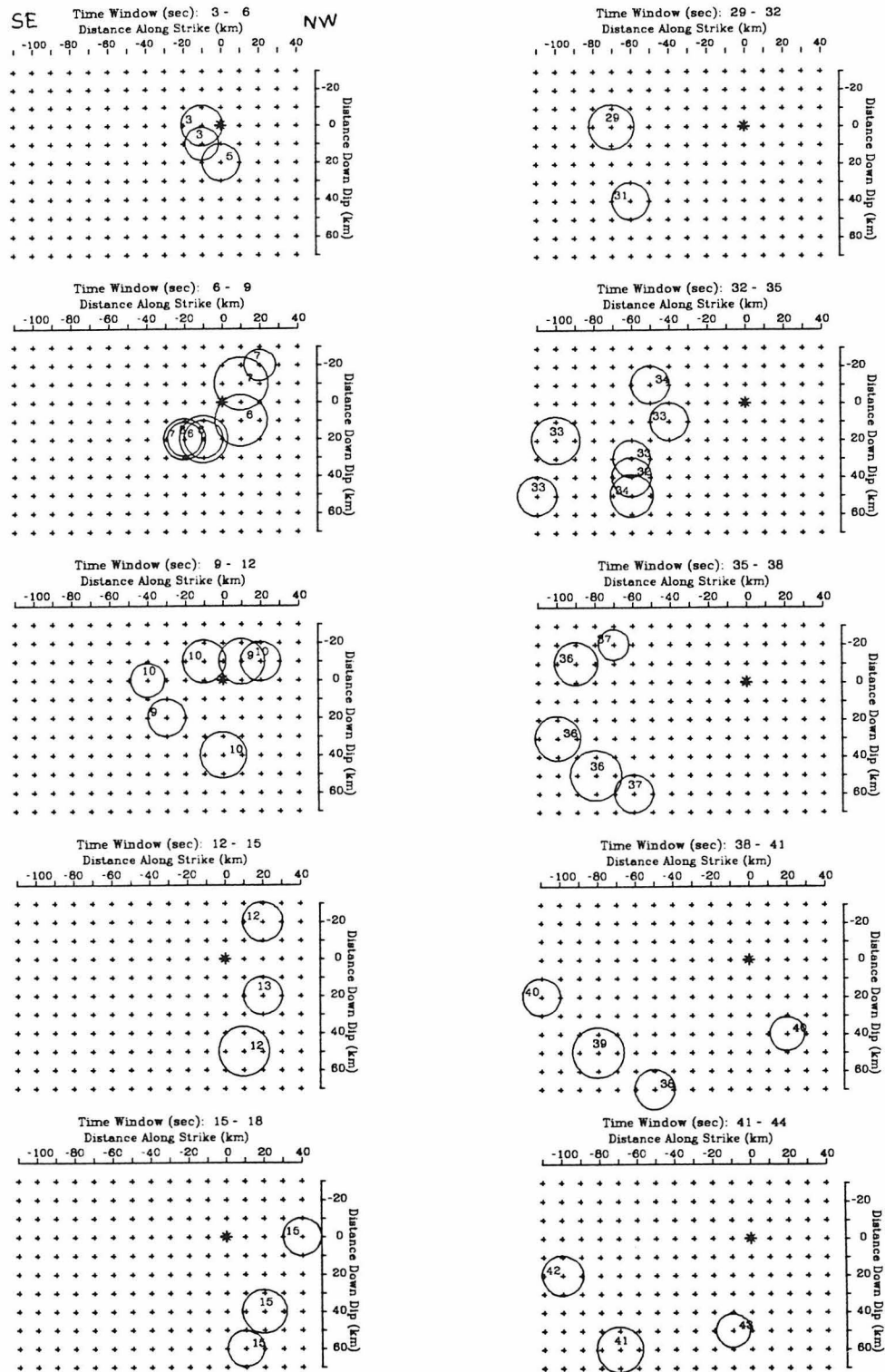Figure 4.11. The 1985 Valparaiso, Chile earthquake. Spatial distribution of moment release displayed in time windows of various durations. Each point source is represented by a circle. The area of the circle estimates the rupture area of the source. The number in each circle gives the initiation time in seconds of the source. Note the orientation of the fault plane. An asterisk marks the hypocenter.

### 1983 Akita-Oki, Japan Earthquake

For this event I used a focal mechanism from Satake (1985) ($\phi{=}10°$, $\delta{=}30°$, $\lambda{=}115°$). The extent of the fault plane was estimated from the aftershock distribution shown in Figure 4 of Sato et al. (1984). 90 sec of record are inverted. The hypocenter is placed at 15 km depth.

Figures 4.12, 4.13, 4.14, and 4.15 show the results of an inversion of the Benioff 1-90 type records using a trapezoid with $\tau_1{=}2$ sec and $\tau_2{=}3$ sec and 50 iterations. The time function (Figure 4.13) shows two main episodes of moment release about 25 sec apart. The spatial distribution of moment release (Figures 4.14 and 4.15) indicates that the first subevent nucleated near the hypocenter and the second about 50 km north. Our time function is similar to that obtained by Kikuchi (unpublished data) from long period WWSSN records and by Hartzell and Heaton (1985) from one Benioff 1-90 record. The time function and spatial distribution of moment release are consistent with the strong motions (Sato, 1985, Table 1, Figures 5 and 6). The rupture process of this earthquake could be considered intermediate between the rupture of the Michoacan and Valparaiso earthquakes, in the sense that the moment is released predominantly but not entirely in two subevents about 50 km and 25 sec apart, while the time function is more irregular than that of the Michoacan earthquake. The seismograms also have an appearance intermediate between the Michoacan and Valparaiso seismograms.

The second subevent about 50 km to the north corresponds to a bend in the fault plane inferred from the aftershock distribution (Sato, 1985; Sato et al., 1984; Satake, 1985). Apparently, this bend in the fault plane behaved as a
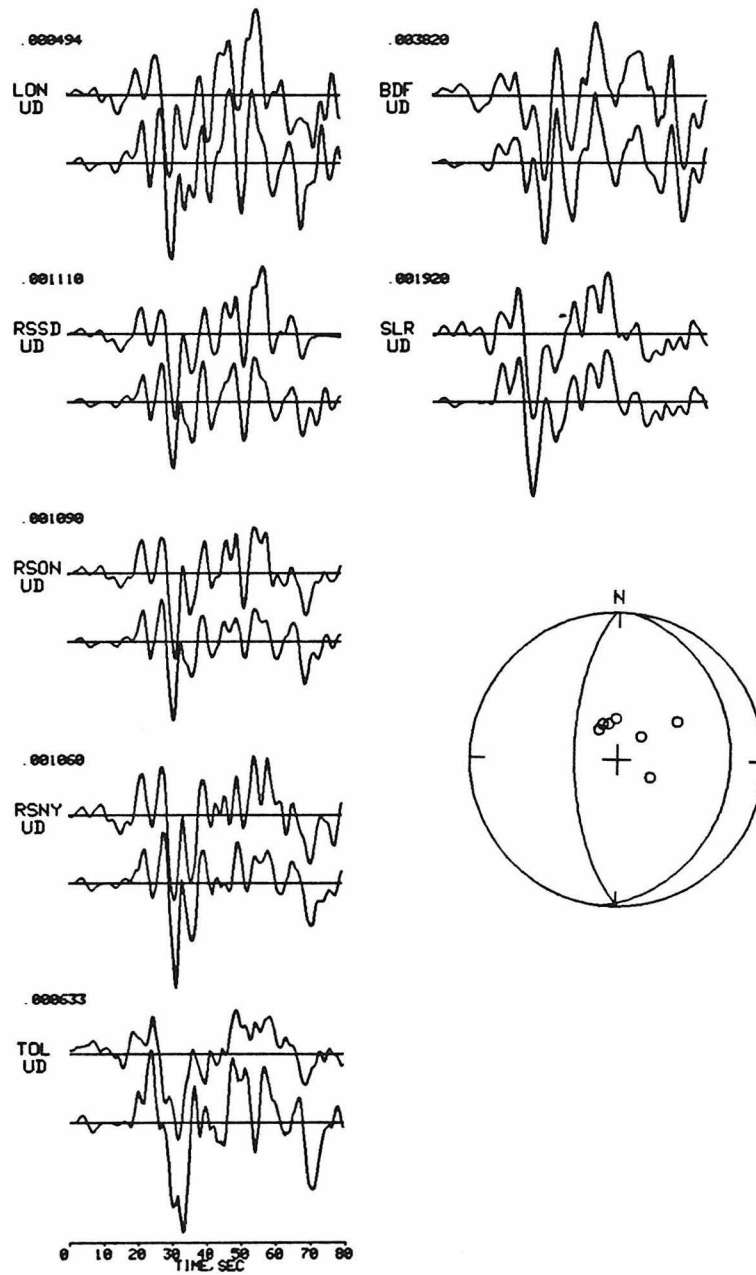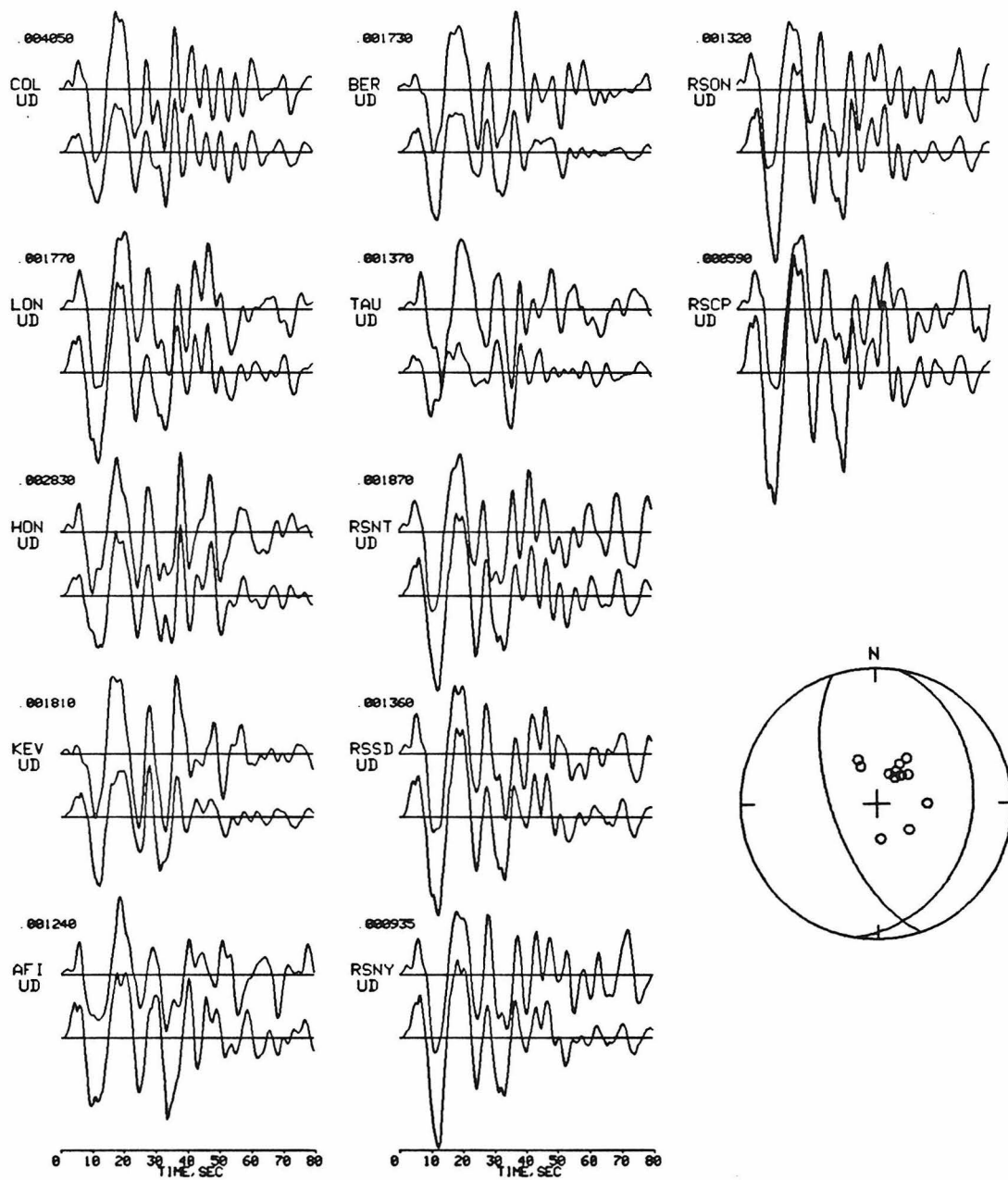
Figure 4.12. The 1983 Akita-Oki, Japan earthquake. Comparison of data (top line) and synthetics (bottom line) from the inversion of GDSN records equalized to a broadband Benioff response. Peak record amplitude is given in cm (e.g., gain is 1).
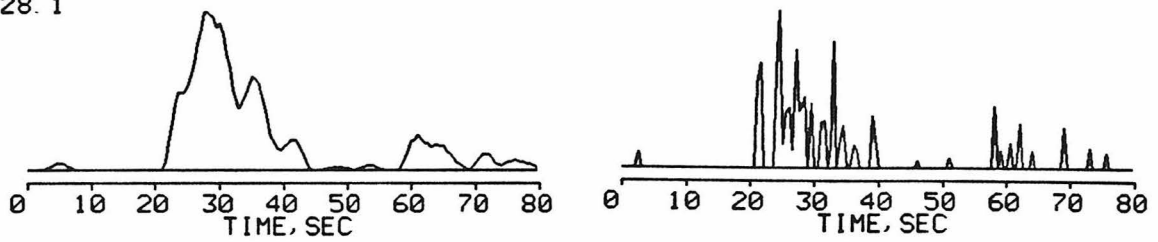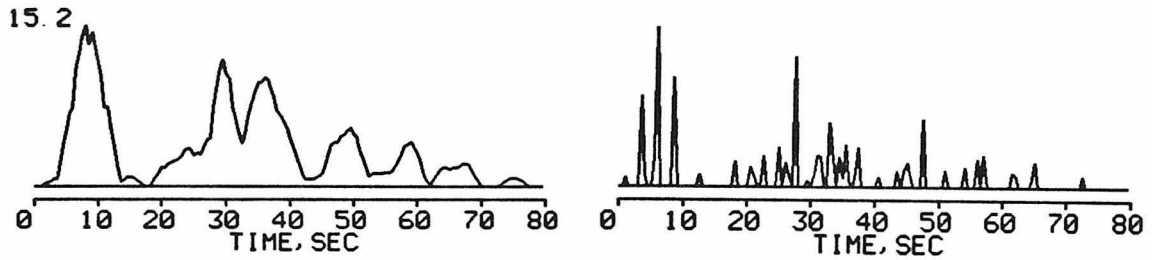
Figure 4.13. The 1983 Akita-Oki, Japan earthquake. Source time function obtained after 50 iterations. The trapezoidal time function of each point source has rise time $\tau_1=2$ sec and duration $\tau_2=3$ sec. Peak moment release rate is given in units of $10^{25}$ dyne-cm/sec. (b). The timing of the initiation of each point source.
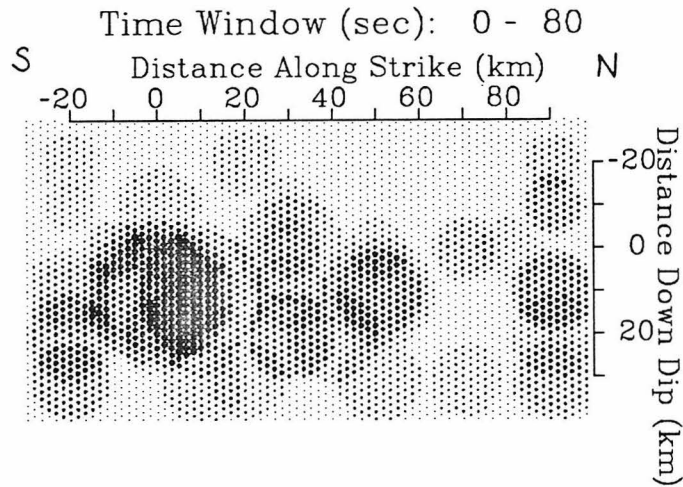


Figure 4.14. The 1983 Akita-Oki, Japan earthquake. Spatial distribution of moment release. Each point source is represented by a circle. The area of the circle estimates the rupture area of the source. The moment releases represented by each circle are summed up over 80 sec. Shading is proportional to the moment release per unit area. Note the orientation of the fault plane. The trench is located towards the top of the figure. An asterisk at (0,0) marks the hypocenter.
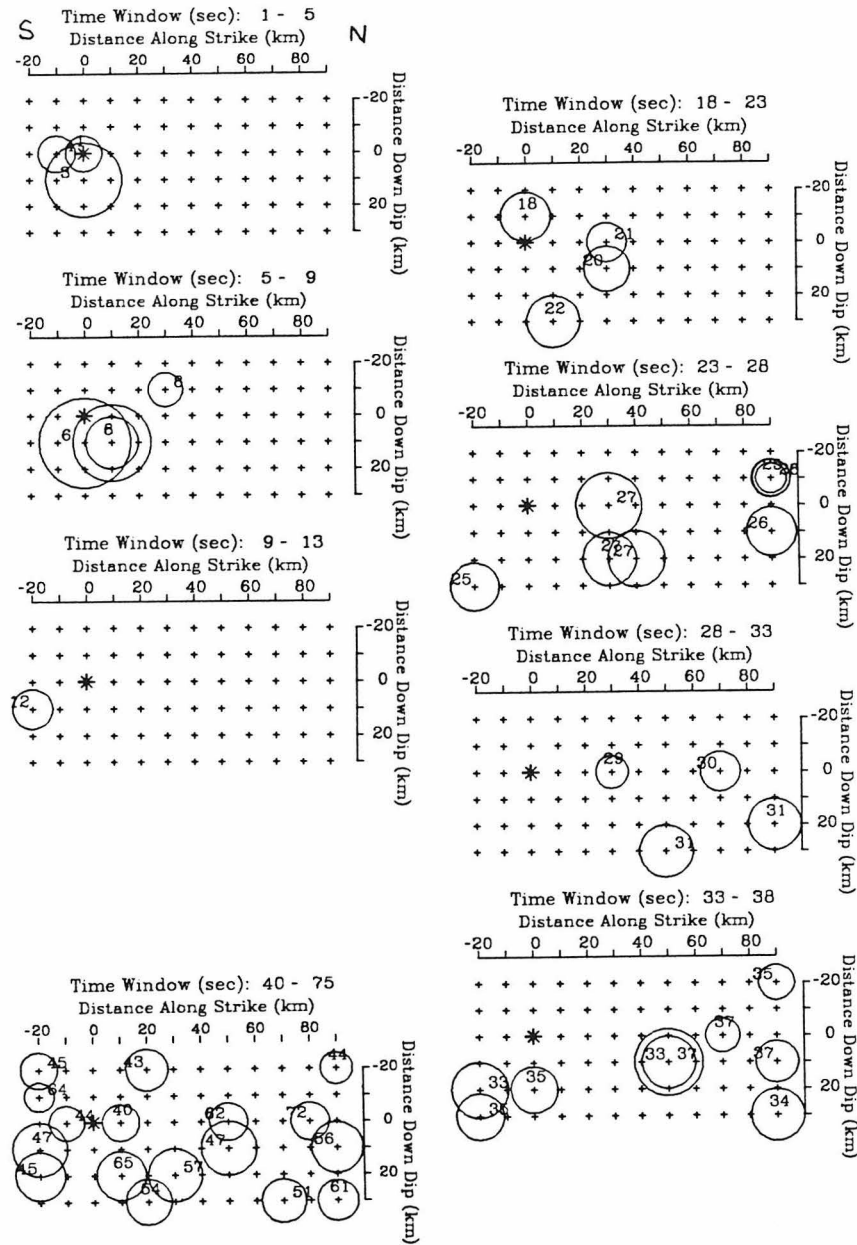
Figure 4.15. The 1983 Akita-Oki, Japan earthquake. Spatial distribution of moment release displayed in time windows of various durations. Each point source is represented by a circle. The area of the circle estimates the rupture area of the source. The number in each circle gives the initiation time in seconds of the source. Note the orientation of the fault plane. An asterisk marks the hypocenter.

geometric asperity in the Akita-Oki earthquake.

## 1986 Andreanof Islands Earthquake

For this event I used a focal mechanism from Hwang and Kanamori (1986) ($\phi=257°$, $\delta=18°$, $\lambda=116°$). The extent of the fault plane was estimated from the distribution of aftershocks relocated by Engdahl (unpublished data). 90 sec of record are inverted. The hypocenter is placed at 30 km depth.

Figures 4.16, 4.17, 4.18, and 4.19 show the results of an inversion of the Benioff 1-90 type records using a trapezoid with $\tau_1=2$ sec and $\tau_2=3$ sec and 80 iterations. This event was not as well recorded by broadband instruments as it should have been. I enlarged the data set by including 7 suitably deconvolved short period SRO, ASRO and DWWSSN records with 6 broadband DWWSSN and RSTN records (see Table 1). The time function (Figure 4.17) shows 3 episodes of moment release - between 8 and 26 sec, between 28 and 55 sec, and between 55 and 75 sec. Figure 4.19 shows the growth of the rupture on the first 28 sec: it grows rapidly outward from the hypocenter at rupture velocities of about 4 km/sec which is the maximum rupture velocity permitted by the inversion; from 28 to 50 sec, the rupture has a complex pattern, with a weak concentration 50 to 80 km west of the hypocenter around 35 sec and 43 sec; from 55 to 75 sec the activity was diffuse. The results can be compared with the results of the same inversion of a somewhat different data set. Hwang and Kanamori (1986) used 6 long-period WWSSN records and 5 broadband GDSN records, equalized to a long-period WWSSN response. They specified a trapezoid with $\tau_1=3$ sec and $\tau_2=6$ sec and iterated 35 times. They
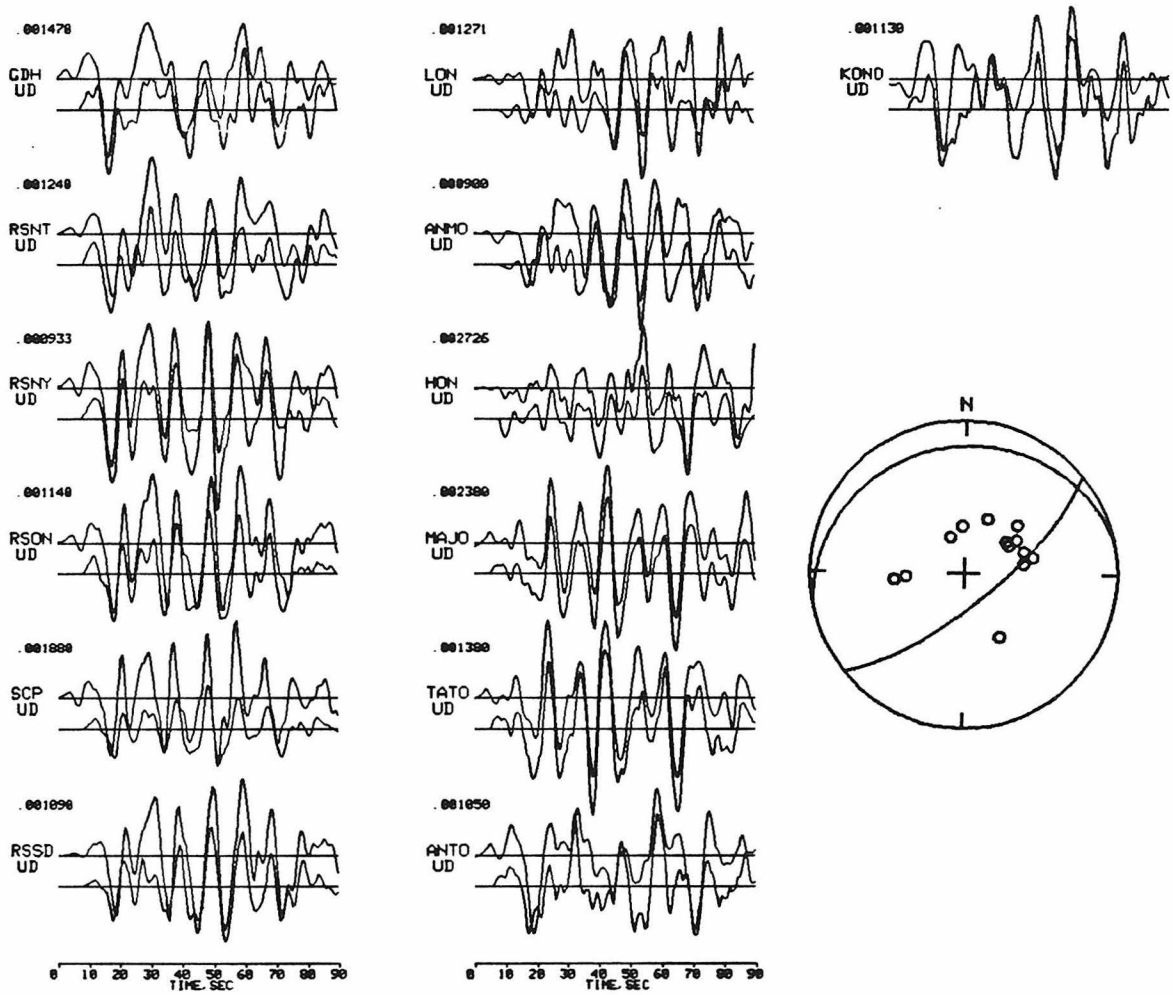
Figure 4.16. The 1986 Andreanof Islands earthquake. Comparison of data (top line) and synthetics (bottom line) from the inversion of GDSN records equalized to a broadband Benioff response. Peak record amplitude is given in cm (e.g., gain is 1).

15.0

TIME, SEC

TIME, SEC
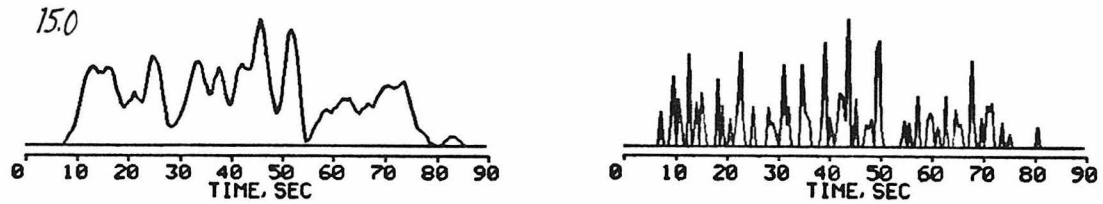
Figure 4.17. The 1986 Andreanof Islands earthquake. Source time function obtained after 80 iterations. The trapezoidal time function of each point source has rise time $\tau_1 = 2$ sec and duration $\tau_2 = 3$ sec. Peak moment release rate is given in units of $10^{25}$ dyne-cm/sec. (b). The timing of the initiation of each point source.

Time Window (sec):  0 - 80

E                                                                    W

Distance Along Strike (km)

-60    -40    -20    0    20    40    60    80    100    120    140

-80

-60

-40

-20

0

20

Distance Down Dip (km)
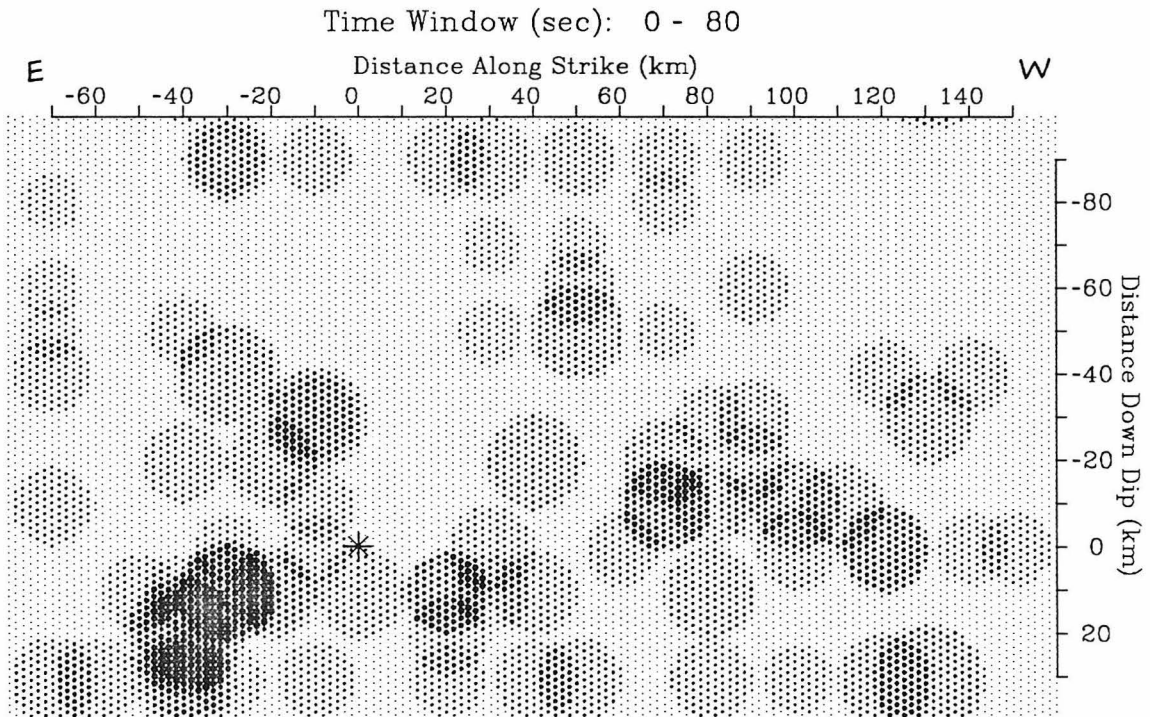
Figure 4.18. The 1986 Andreanof Islands earthquake. Spatial distribution of moment release. Each point source is represented by a circle. The area of the circle estimates the rupture area of the source. The moment releases represented by each circle are summed up over 90 sec. Shading is proportional to the moment release per unit area. Note the orientation of the fault plane. The trench is located towards the top of the figure. An asterisk marks the hypocenter.
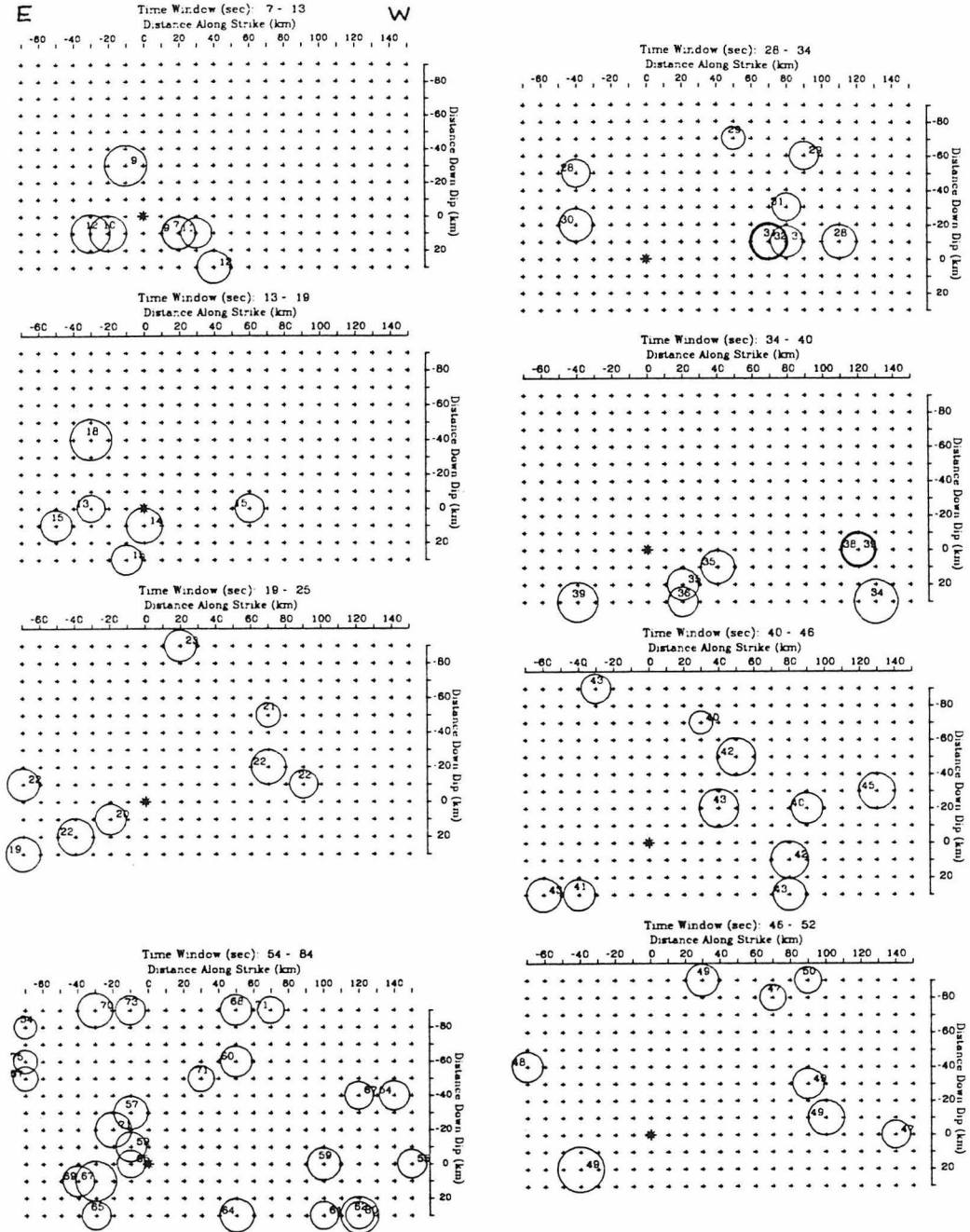
Figure 4.19. The 1986 Andreanof Islands earthquake. Spatial distribution of moment release displayed in time windows of various durations. Each point source is represented by a circle. The area of the circle estimates the rupture area of the source. The number in each circle gives the initiation time in seconds of the source. Note the orientation of the fault plane. An asterisk marks the hypocenter.

found 4 moment release episodes (their Figure 4), two of which correspond to subevents (their Figure 5) - one nucleating about 10 sec into the event near the hypocenter and one nucleating 30 sec into the event about 90 km to the west. The inversion of the shorter period data, while generally similar to that of Hwang and Kanamori (1986) and Christiansen (personal communication), suggests that moment release was more diffuse at short periods than at longer periods. The difference between the long and short periods may reflect the complexity of the interplate coupling in the Aleutian arc.

## 4.4 Discussion and Conclusions

Comparing the source spectra of the earthquakes studied above can yield complementary information. In fact, the source spectrum is proportional to the Fourier transform of the time function. The source spectra are computed from GDSN intermediate and short-period teleseismic records, as described in Chapter 2. This is virtually the same data set used in the inversions. We compute the spectra at periods of 1 to 30 sec. Figure 4.20 shows a representative broadband record, the time function, average spectrum, and spatial distribution of moment release for each earthquake studied in this chapter. This is all essentially the same information (since it comes from the same records) with different elements emphasized.

The earthquakes can be roughly ordered in terms of increasing complexity of the rupture process. Somewhat arbitrarily, I consider that greater clustering of moment release in space and time represents less complexity of the
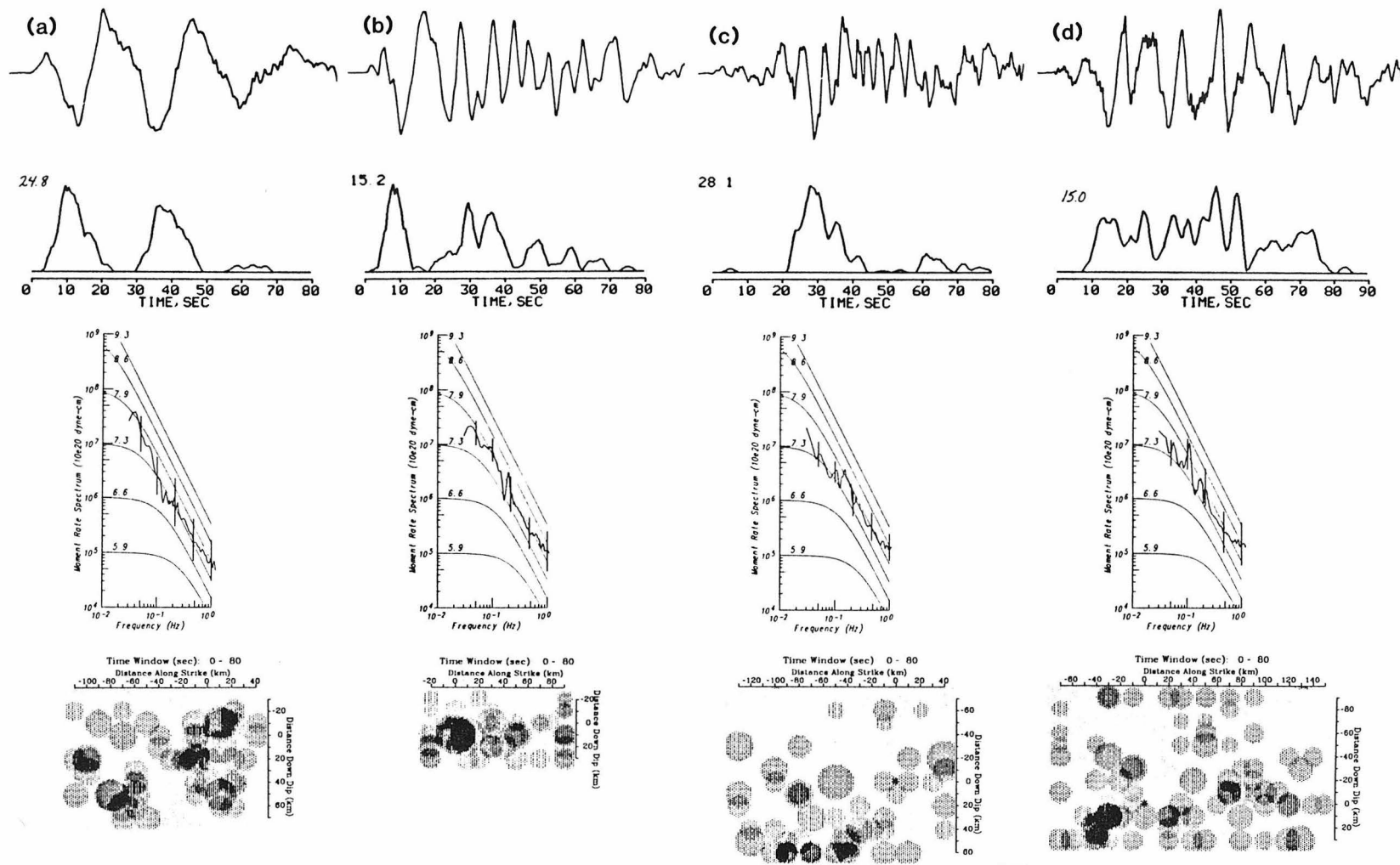
Figure 4.20. A broadband record from station RSNY, and the time function, average spectrum, and spatial distribution of moment release for each of the earthquakes studied here. (a) 1985 Michoacan, Mexico. (b) 1983 Akita-Oki, Japan. (c) 1985 Valparaiso, Chile. (d) 1986 Andreanof Islands, Alaska.

rupture process. With this definition, the Michoacan, Mexico earthquake has the least complexity in its rupture process. The rupture of the Akita-Oki event exhibited somewhat more complexity. This can also be seen in the spectrum. The Valparaiso, Chile earthquake ruptured with yet more complexity. And the Andreanof Islands earthquake had the most complexity of rupture. It has the largest fault plane and moment release, also.

The different styles of rupture of these earthquakes must come from differences in physical properties at the subduction interface. The first-order effects on interplate coupling are due to the age of the subducted plate and the rate of convergence (Ruff and Kanamori, 1980). These effects seem to control the size of the largest earthquake along a subduction zone. However, the earthquakes that we study here are not the largest along their respective zones, except possibly the Akita-Oki earthquake. Second order effects, such as roughness of the subducting seafloor or thickness and porosity of subducted sediments, may thus control the rupture style of these events. Unfortunately, this information is not well enough known at present to permit a comparison of these factors for the earthquakes studied here. Bathymetry, for example, is available on GEBCO maps with a contour interval of 100 m and in digital format with a spacing of 5 minutes. This is probably too coarse to indicate reliably topographic changes of 10's of meters across 3 to 30 km. In addition, the GEBCO map of the seafloor subducting in the Aleutian trench shows considerably less complexity there than seaward of the Mexican trench, probably due merely to less extensive data off the coast of the Aleutians than off the coast of Mexico. A thorough examination of ship-track bathymetry in the various seafloors relevant to the earthquakes studied here is beyond the scope of this

thesis. Also, one would really like to know the bathymetry of the already subducted seafloor, which may well differ from that of the unsubducted seafloor. This kind of information is only available through seismic reflection surveys, so a thorough understanding of the physical reasons for various rupture styles and even the confidence that a given rupture style persists in an area (as it seems to along the Mexican trench) must await more detailed data and a longer historical record.

We have found significant differences between the rupture styles of different shallow subduction earthquakes of similar size. These differences have important implications for the generation of strong motions. This will be explored in the next chapter.

## 4.5 References

Christiansen, D. and L. Ruff, Rupture process of the March 3, 1985 Chilean Earthquake, *Geophys. Res. Lett.*, in press, 1986.

Ekstrom, G.and A. Dziewonski, A very broad band analysis of the Michoacan, Mexico earthquake of September 19, 1985. *Geophys. Res. Lett., 13*, 605-608, 1986.

Fuyukama, E., and K. Irikura, Rupture process of the 1983 Japan Sea (Akita-Oki) earthquake using a waveform inversion method, *Bull. Seism. Soc. Am., 76*, 1623-1640, 1986.

Hartzell, S. and T. Heaton, Teleseismic time functions for large, shallow subduction zone earthquakes, *Bull. Seism. Soc. Am., 75*, 965-1004, 1985.

Hwang, L. and H. Kanamori, Source parameters of the May 7, 1986 Andreanof Islands earthquake, *Geophys. Res. Lett.*, 1986, in press.

Kanamori, H. and D. L. Anderson, Theoretical basis of some empirical relations in seismology, *Bull. Seism. Soc. Am., 65*, 1073-1095.

Kikuchi, M. and H. Kanamori, Inversion of complex body waves, *Bull. Seism. Soc. Am., 72*, 491-506, 1982.

Kikuchi, M. and Y. Fukao, Iterative deconvolution of complex body waves from great earthquakes - the Tokachi-Oki earthquake of 1968, *Phys. Earth Planet. Inter., 37*, 235-248, 1985.

Kikuchi, M. and H. Kanamori, Inversion of complex body waves - II, *Phys. Earth Planet. Inter., 43*, 205-222, 1986.

Kikuchi, M. and Y. Fukao, In version of long period P-waves from great earthquakes along subduction zones, *Tectonophysics*, in press, 1986.

Ruff, L. and H. Kanamori, Seismicity and the subduction process, *Phys. Earth Planet. Inter., 23*, 240-252, 1980.

Satake, K., The mechanism of the 1983 Japan Sea earthquakes inferred from long period surface waves and tsunamis, *Phys. Earth Planet. Inter., 37*, 249-260, 1985.

Sato, T., M. Kosuga, K. Tanaka, and H. Sato, Aftershock distribution of the Nihonkai-Chubu earthquake from relocated hypocenters (abstract, in Japanese), *Programme and Abstracts, Seism. Soc. of Japan, 2*, A84, 1984.

Sato, T., M. Kosuga, K. Tanaka, and H. Sato, Aftershock distribution of the 1983 Nihonkai-Chubu (Japan Sea) earthquake determined from relocated hypocenters (abstract, in Japanese), *J. Phys. Earth*, in press, 1985.

Sato, T., Rupture characteristics of the 1983 Nihonkai-Chubu (Japan Sea) earthquake as inferred from strong motion accelerograms, *J. Phys. Earth,* *33*, 525-557, 1985.

Stolte, C. et al., Fine structure of a post failure Wadati-Benioff zone, *Geophys. Res. Lett., 13*, 577-580, 1986.

UNAM Seismology Group, The September 1985 Michoacan Earthquakes: aftershock distribution and history of rupture, *Geophys. Res. Lett., 13*, 573-576, 1986.

# Chapter 5

# Comparison of Strong Motion Spectra with Teleseismic Spectra

## Abstract

Strong motion spectra of the 1985 Michoacan, Mexico and the 1983 Akita-Oki, Japan earthquakes are compared with their teleseismic spectra. The spectral levels of the Michoacan strong motions, which were recorded by a high-quality digital array, agree to within a factor of 2 with those predicted by the Michoacan teleseismic records. The Michoacan teleseismic spectrum is lower than that of Akita-Oki. This relationship also holds for their strong motion spectra. This consistency means that teleseismic records, which are relatively more abundant, can be used to predict properties of strong motions from large earthquakes.

## 5.1 Introduction

The different styles of rupture found in Chapter 4 from teleseismic body waves undoubtedly affect the generation of strong motions near the earthquake source. In this chapter, I analyze two sets of strong motion records to see whether the differing characteristics seen in the teleseismic spectra are reflected in the strong motions. Because these data sets have only recently become available, this comparison has not been made before.

Of the earthquakes studied in Chapter 4, the 1985 Michoacan, Mexico, 1983 Akita-Oki, Japan, and 1985 Valparaiso, Chile earthquakes each produced a sizeable set of strong motion recordings. The comparison between the peak accelerations of the strong motions of the Michoacan and the Valparaiso earthquakes (Figure 3.7 after Anderson et al., 1986) is consistent with the teleseismic spectra of the two events seen in Figures 3.3 or 5.1. Differences in the siting of accelerographs in the two regions, and differences in the frequencies represented in Figures 3.3 and 3.7 render this comparison not entirely convincing. The strong motions of the Valparaiso earthquake, however, are not yet digitized and available to interested scientists. So, in this chapter, I compare the strong motions of the Michoacan earthquake to those of the Akita-Oki earthquake. In particular, I wish to obtain strong motion spectra that can be compared to the teleseismic source spectra obtained in Chapters 2 and 3. Figure 5.1 shows teleseismic acceleration source spectra for the Michoacan, Mexico, Akita-Oki, Japan, and Valparaiso, Chile earthquakes. These acceleration source spectra show the second derivative with respect to angular frequency of the moment rate or source spectrum defined in equations (2.1) or (5.1). Clear

differences exist between these spectra, with the Michoacan spectrum generally having the lowest level between 1 and 0.1 Hz, despite having the largest seismic moment.
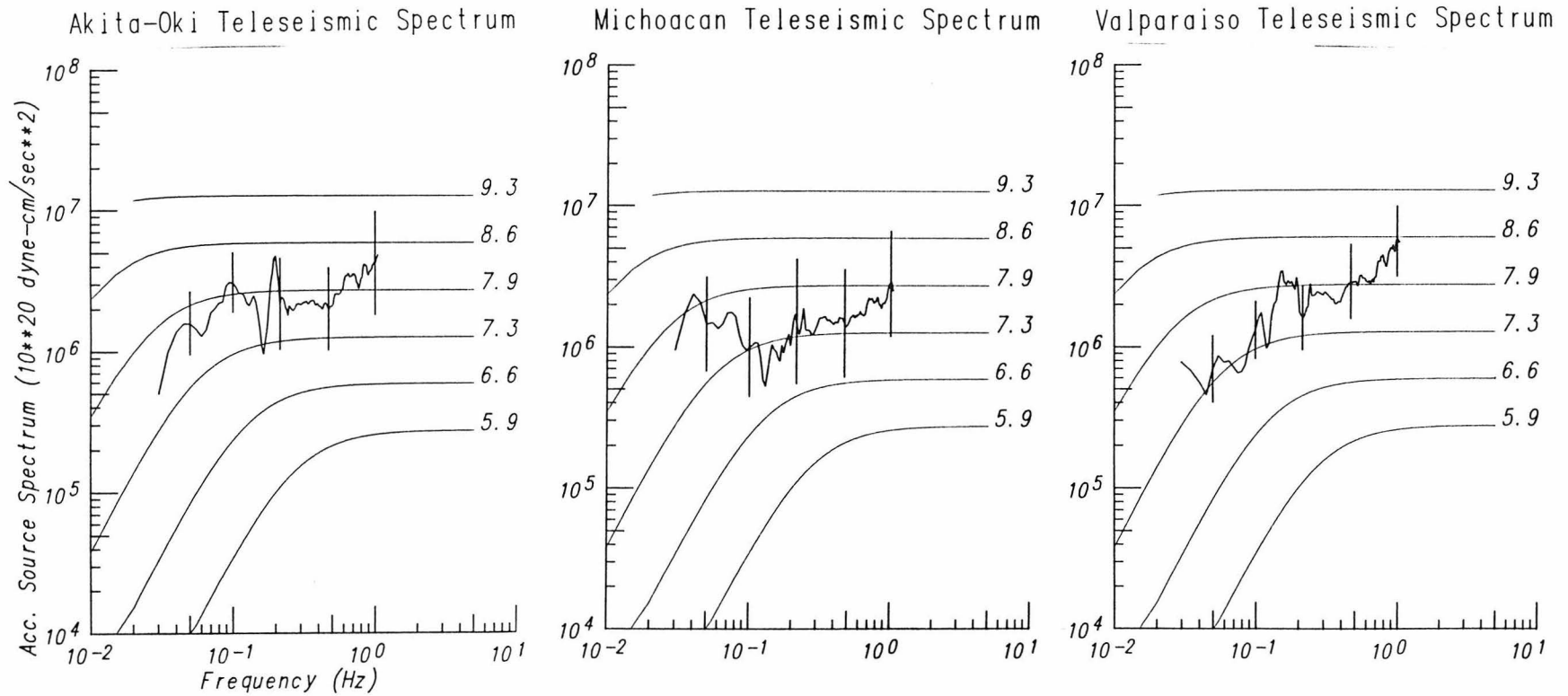
Figure 5.1. Teleseismic acceleration source spectra for the 1983 Akita-Oki, Japan, 1985 Michoacan, Mexico and 1985 Valparaiso, Chile earthquakes. The thin lines show $\omega^{-2}$ spectra (with stress parameter 30 bars) as references. The standard deviations at selected frequencies are shown.

## 5.2 Strong Motion Records
## of the Michoacan, Mexico and Akita-Oki, Japan Earthquakes

Figures 5.2 and 5.3 show the locations of the strong motion stations used in this study. The Guerrero array in coastal Mexico is a recently installed array of digital accelerographs (Anderson et al., 1986). The Japanese strong motions of the Akita-Oki earthquake were gathered from analog Japanese accelerographs operated by several different institutions (Sato, 1985). I selected the largest of the two horizontal components of motion from each of the stations shown in Figure 5.2 and 5.3. For the Michoacan earthquake, the north-south components were the largest.

I wish to obtain strong motion spectra that can be compared with Figure 5.1. An important question is how to correct the strong motions for the amplitude decay with distance between the station and the source. What distance is appropriate for the distance between station and source? And what distance correction is appropriate? To examine these issues, I plot spectral fall-off with distance for three measures of the distances between stations and source. Two standard approaches are to use the distance between the station and the hypocenter, or between the station and the nearest point on the fault plane. Because the length of the rupture can be 100 to 200 km for earthquakes of $M_W=8$, while the distances between the fault plane and the stations can be less than 100 km, one number may not adequately represent the distance between the earthquake source and the station. We can, however, make a reasonable comparison using one number to represent the distance to the fault plane, as seen below.
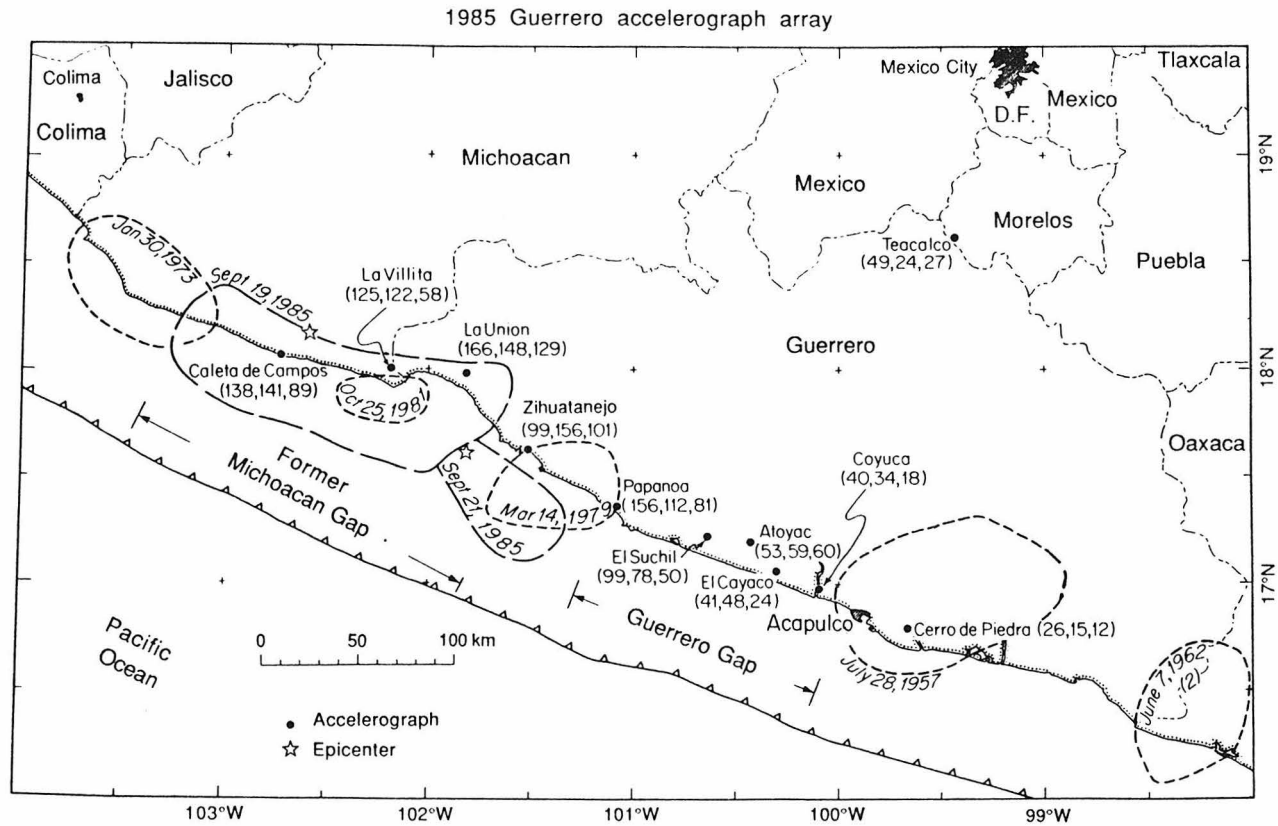
Figure 5.2.  Map of coastal Mexico showing the strong motion stations of the Guerrero array used in this study.  Stars show the epicenters of the Septemeber 19 and 21, 1985 Michoacan earthquakes.  Dashed lines show the aftershock zones of large earthquakes in this region.  Peak accelerations are given for each station for the north, east, and vertical components, respectively.  After Anderson et al. (1986).
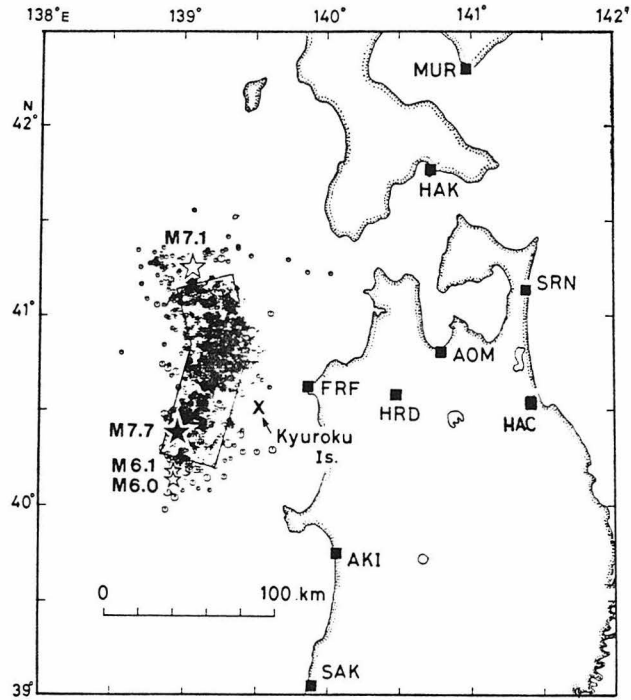
Figure 5.3.  Map of northern Honshu, Japan showing the strong motion stations used in this study, and the distribution of aftershocks of the May 26, 1983 Akita-Oki earthquake, whose epicenter is indicated by a solid star.   After Sato (1985).

Plotted in Figures 5.3, 5.4, 5.5, 5.6, 5.7, 5.8, and 5.9 are spectral amplitudes at 6 frequencies of acceleration of the ground in units of cm/sec vs. three measures of distance. The numbers in the upper right-hand corner of each plot are p and C in

$$y = C \, r^p \, ,$$

where y is the spectral amplitude of acceleration and r is distance. The parameters p and C were determined by a least-squares fit to the data. Figures 5.4 and 5.5 show spectral amplitudes vs. hypocentral distance for the Michoacan and Akita-Oki earthquakes. Figures 5.6 and 5.7 show spectral amplitudes vs. distance from the nearest point on the fault plane. Figures 5.8 and 5.9 show spectral amplitudes vs. distance from the center of the fault plane. For all these plots, the amplitudes of the Michoacan earthquake generally have a lower absolute level for a given distance, a slower fall-off with distance, and less scatter than those of Akita-Oki. The lower absolute level is consistent with the lower level of the Michoacan teleseismic spectrum seen in Figure 5.1. The fall-off with distance seen for the Michoacan strong motions is slower than $\frac{1}{r}$, which is expected for body waves. Presumably, this slow fall-off is due to the geometric effect of the large fault plane for the nearby stations and/or the preponderance of surface waves at the farther stations. The slow fall-off is consistent with the time-domain fall-off for large earthquakes shown in figures 19, 20, and 21 of Heaton et al. (1986). The steep fall-off with distance seen in the Akita-Oki spectral levels is mainly controlled by the two of the most distant stations SRN and MUR. It is not clear why the Akita-Oki spectral levels fall off so rapidly. The Guerrero accelerographs, being digital

and newer, are regarded as more reliable than the Japanese accelerographs. The Japanese strong motion stations are a more heterogeneous group, since stations are operated by several different institutions.

So, what measure of distance is most appropriate? Figures 5.4, 5.6, and 5.8 are actually quite similar. It seems indefensible to use the distance to the hypocenter, if a more representative distance can be easily obtained. Distance to the nearest point on the fault plane may be reasonable for peak values, like peak acceleration. But, distance to the center of the fault plane seems physically more reasonable for integrated quantities such as spectra. Actually, one would like to calculate the harmonic average of the distances from the station to each part of the fault plane, but this will not be very different from the distance to the center of the fault plane. And one could weight the average by the moment release in each part of the fault plane, if this is known. These corrections, however, are not essential for the present comparison.

And what distance correction to use? From the Michoacan data at 1 Hz, a fall-off with distance of $\frac{1}{r^{0.63}}$ is observed. We could use all the strong motion records and correct their spectra with that distance decay. This procedure, however, seems contrived and out of keeping with the philosophy of equations (2.1) and (5.1). It is more straightforward to restrict the calculation of the source spectrum to the closer records, which are mostly composed of body waves, and correct them with a $\frac{1}{r}$ distance decay. This is done in the next section.

Figure 5.4. Spectral amplitudes of accelerations of the 1985 Michoacan, Mexico earthquake vs. distance from the stations to the hypocenter. Each plot shows the spectral amplitudes at a given frequency. The numbers in the upper right hand corners are p and C defined in the text.

1983 Akita-Oki Spectral Amp. vs Hypocentral Distance
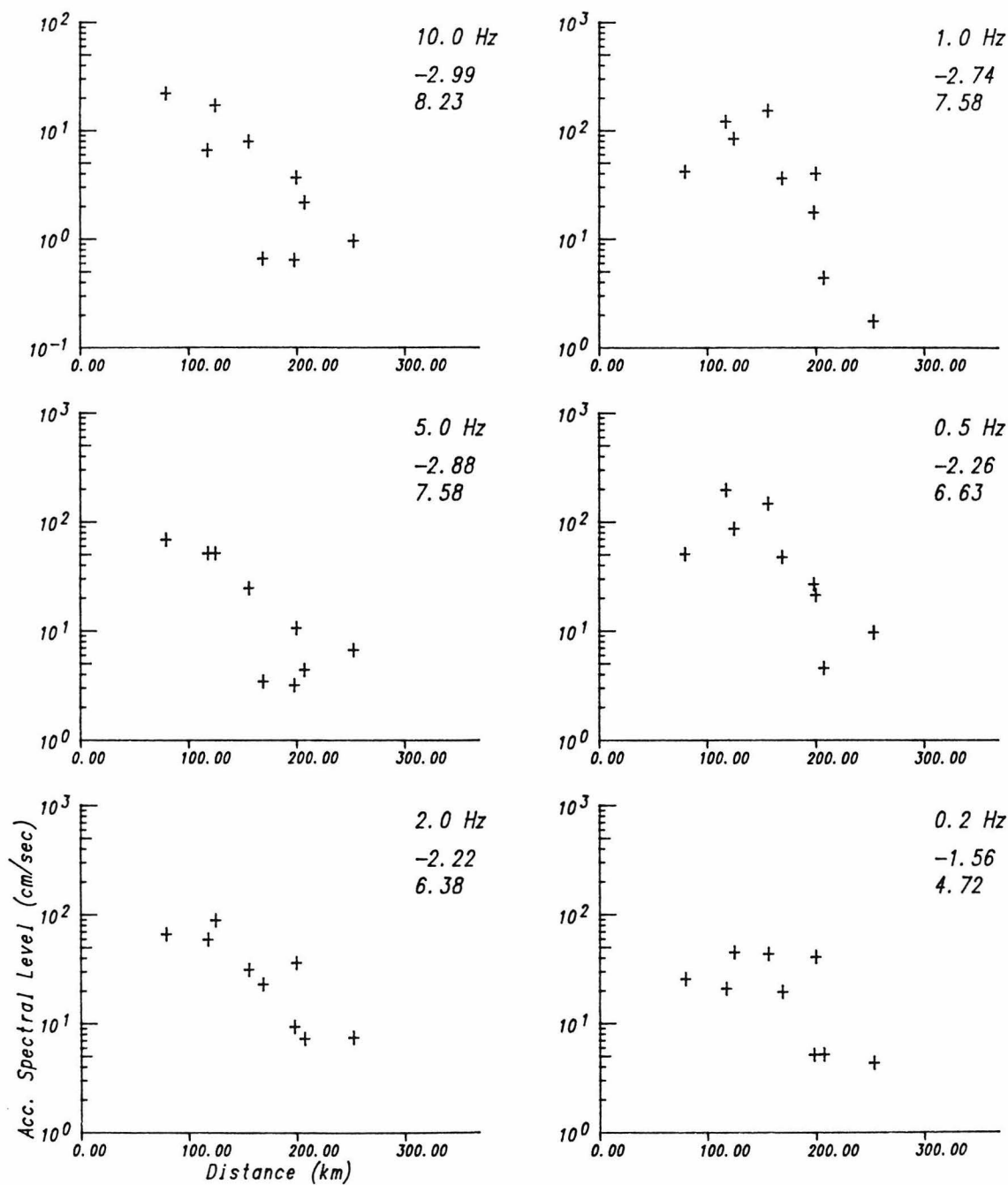


Figure 5.5. Spectral amplitudes of accelerations of the 1983 Akita-Oki, Japan earthquake vs. distance from the stations to the hypocenter. Each plot shows the spectral amplitudes at a given frequency. The numbers in the upper right hand corners are p and C defined in the text.

1985 Michoacan Spectral Amp. vs Distance to Nearest Part of Fault Plane
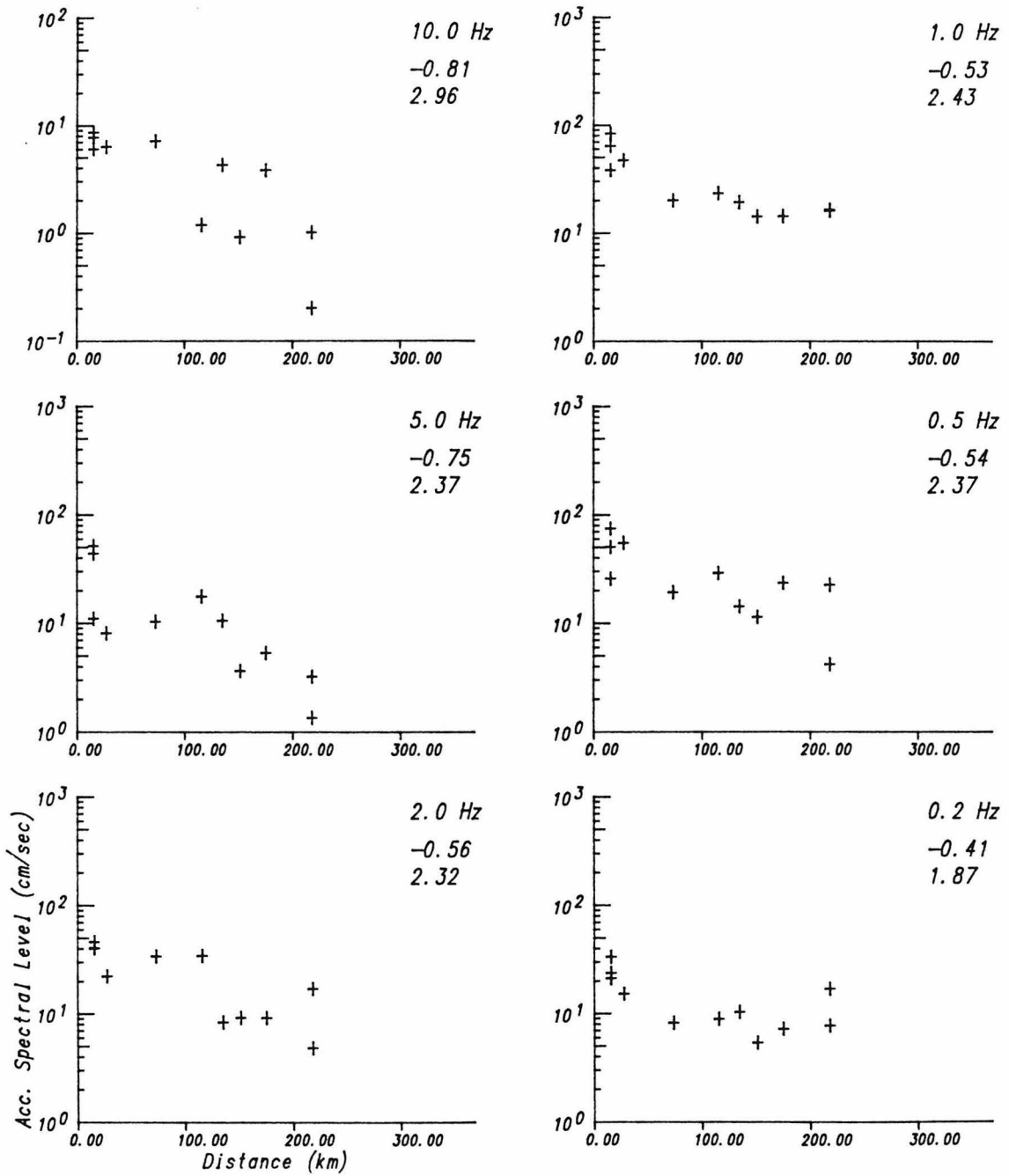
Figure 5.6. Spectral amplitudes of accelerations of the 1985 Michoacan, Mexico earthquake vs. distance from the stations to the nearest part of the fault plane. Each plot shows the spectral amplitudes at a given frequency. The numbers in the upper right hand corners are p and C defined in the text.

1983 Akita-Oki Spectral Amp. vs Distance to Nearest Part of Fault Plane
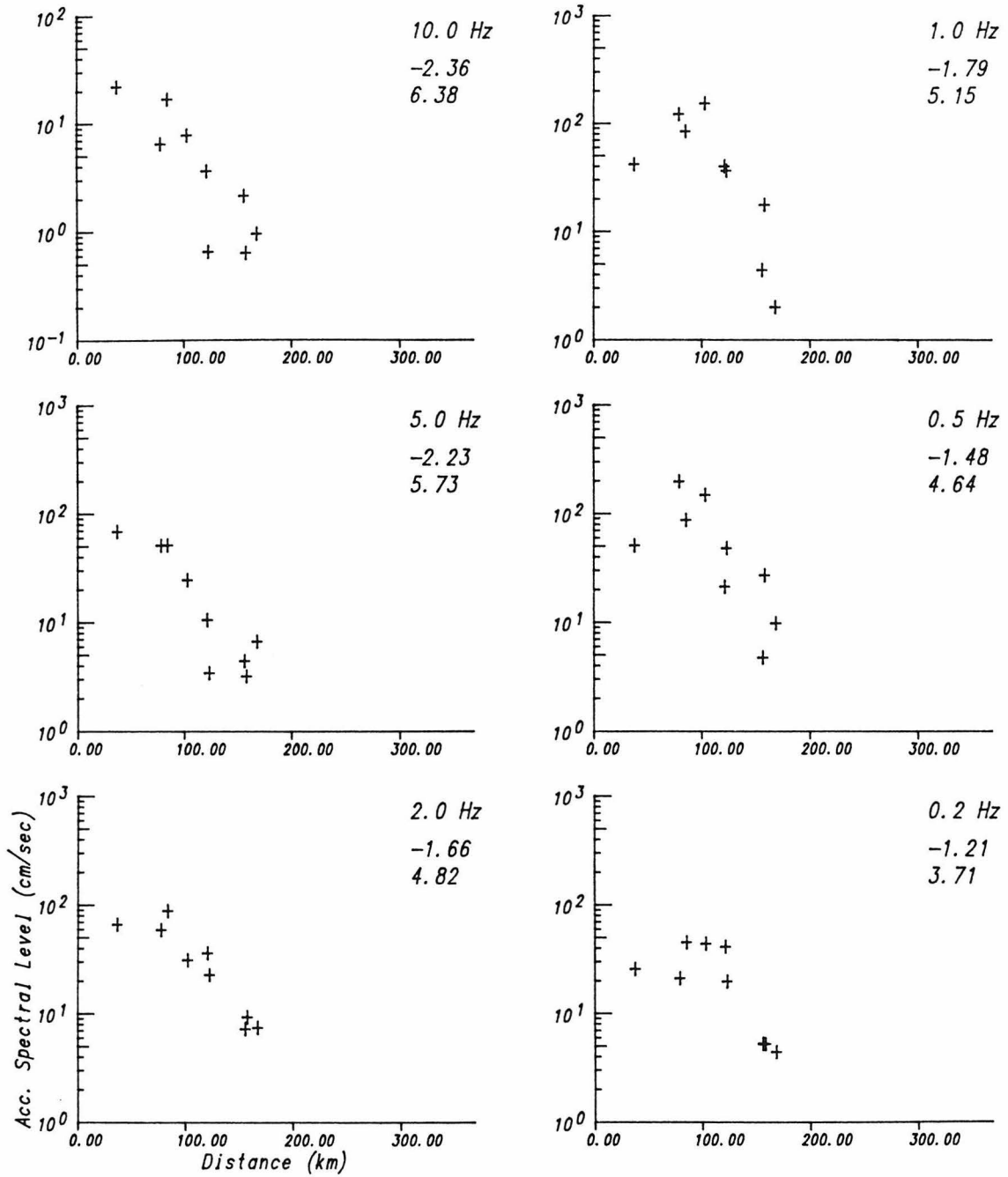


Figure 5.7. Spectral amplitudes of accelerations of the 1983 Akita-Oki, Japan earthquake vs. distance from the stations to the nearest part of the fault plane. Each plot shows the spectral amplitudes at a given frequency. The numbers in the upper right hand corners are p and C defined in the text.

## 1985 Michoacan Spectral Amp. vs Distance to Center of Fault Plane
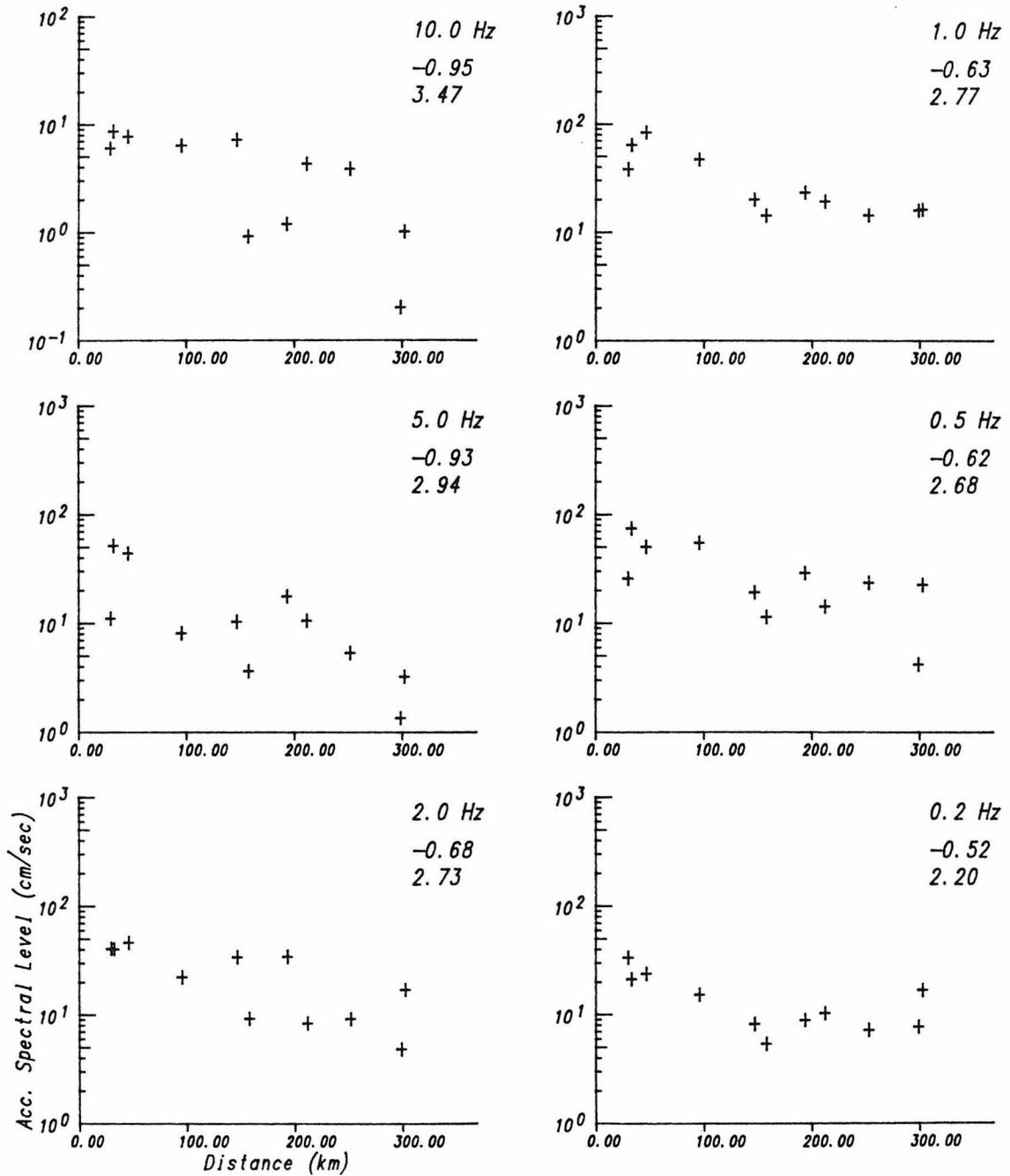


Figure 5.8. Spectral amplitudes of accelerations of the 1985 Michoacan, Mexico earthquake vs. distance from the stations to the center of the fault plane. Each plot shows the spectral amplitudes at a given frequency. The numbers in the upper right hand corners are p and C defined in the text.

**1983 Akita-Oki Spectral Amp. vs Distance to Center of Fault Plane**
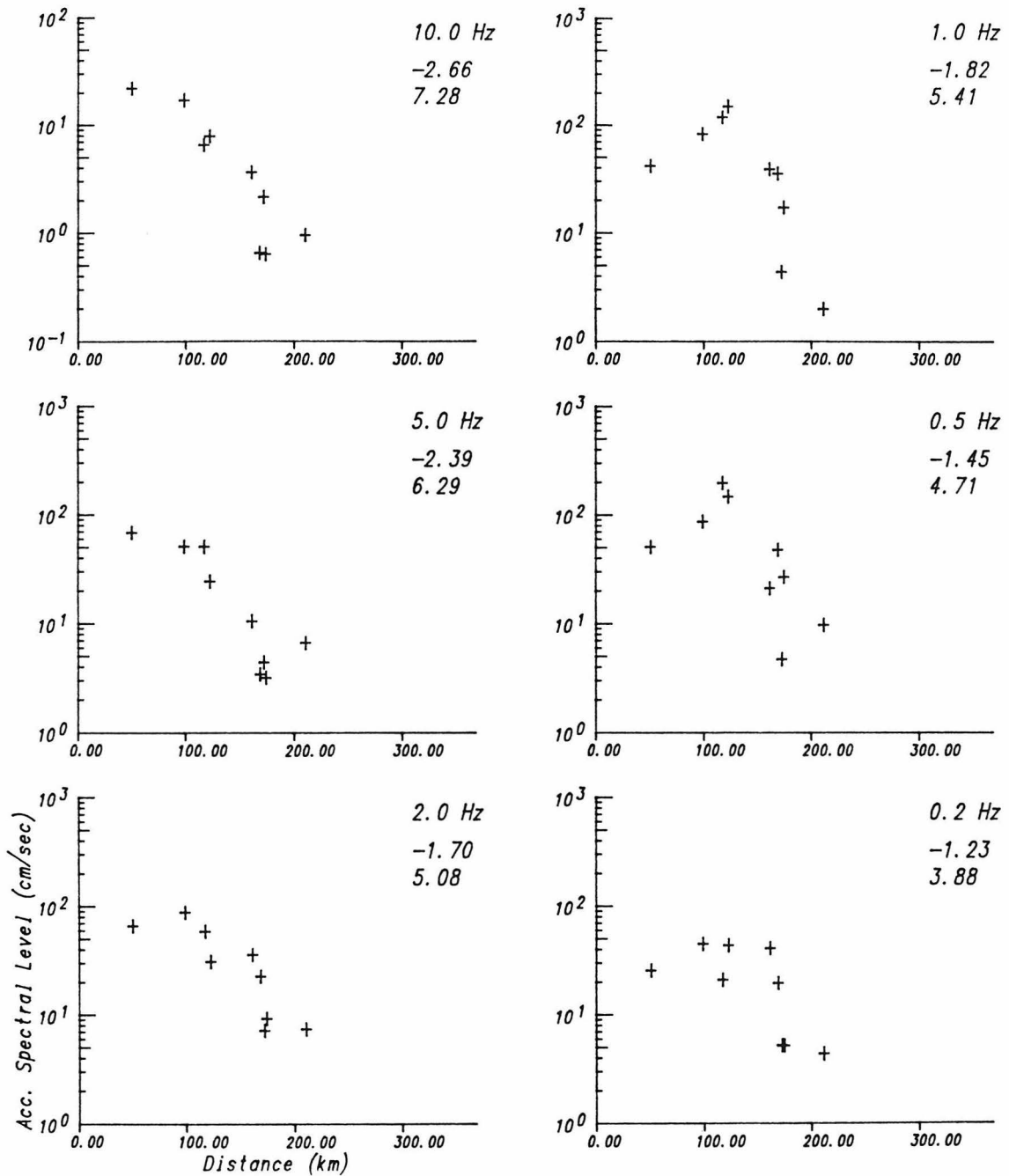


Figure 5.9. Spectral amplitudes of accelerations of the 1983 Akita-Oki, Japan earthquake vs. distance from the stations to the center of the fault plane. Each plot shows the spectral amplitudes at a given frequency. The numbers in the upper right hand corners are p and C defined in the text.

## 5.3    Source Spectra from Strong Motion Records

I wish to determine an average source spectrum from strong motion records that can be compared with the average source spectra determined from teleseismic records in Chapters 2 and 3. I assume that the strong motion records consist primarily of S body waves, and that the far-field approximation applies. This is probably a good assumption at frequencies of 0.2 Hz to 2 Hz for stations between 30 and 100 km from the source. Then in analogy with equation (2.1), we write the moment rate spectrum of strong motions as

$$\hat{M}(\omega) = \frac{4\pi\rho\beta^3\, r}{R_{\theta\phi}\, C}\ e^{\frac{\omega\, r}{2Q\beta_{av}}}\ u(\omega), \tag{5.1}$$

where $\rho$ and $\beta$ are the density and S-wave velocity at the source, $\beta_{av}$ is an average S-wave velocity between the source and the station, r is the distance between the station and the source, $R_{\theta\phi}$ is the radiation pattern of SH waves, C is the free surface receiver effect, Q is the quality factor, and $u(\omega)$ is now the S-wave displacement. The terms $\left[ r\ e^{\frac{\omega r}{2Q\beta_{av}}} \right]$ correspond to $\left[ \frac{1}{g(\Delta)}\ e^{\frac{\omega t^*}{2}} \right]$ in the teleseismic case. The quantity $\omega^2\, \hat{M}(\omega)$ is plotted in Figure 5.10. In the following analysis we take $\beta=3.8$ km/sec, and $\rho=2.8$ gm/cm$^3$, which is consistent with the P-wave velocity and density used in Chapters 2 and 3. $\beta_{av}=3.4$ km/sec. Q is assumed to be 300. We take C=2 to account for the free surface effect for SH waves, and $R_{\theta\phi}=0.63$, which is the value of the S radiation pattern averaged over the entire sphere of take-off angles (Brune, 1970). This implies strong scattering near the source. For the purpose of comparing strong motion spectra with teleseismic spectra determined from
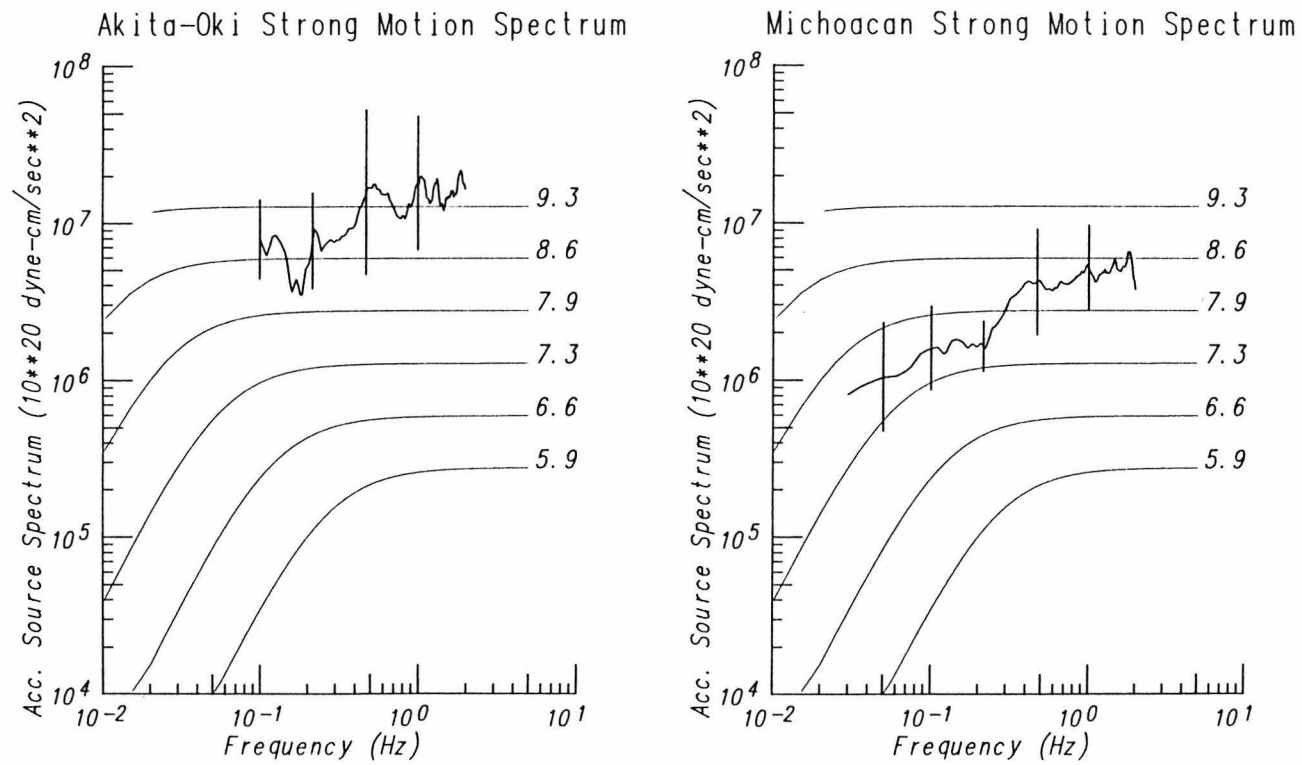
Figure 5.10. Strong motion acceleration source spectra for the 1983 Akita-Oki, Japan and 1985 Michoacan, Mexico earthquakes. The thin lines show $\omega^{-2}$ spectra (with stress parameter 30 bars) as references. The standard deviations at selected frequencies are shown.

GDSN records, we are interested in the frequency band 0.03 Hz to 1 Hz. Analog strong motion records that are digitized by hand, however, like those of the Akita-Oki earthquake are only reliable down to frequencies of about 0.2 Hz. Figure 5.10 shows the acceleration source spectra of the Michoacan and Akita-Oki strong motion records. To compute these spectra, only stations at distances less than 150 km from the center of the fault plane (Caleta de Campos, La Villita, La Union, and Zihuatanejo for the Michoacan earthquake, and FRF, HRD, AOM, and AKI for the Akita-Oki earthquake) were used. This restriction justifies somewhat the assumption that the records used in equation (5.1) do indeed consist primarily of S body waves, and not surface waves. Also, Q (which is poorly known) is less important for shorter distances.

## 5.4  Discussion and Conclusions

Compare the strong motion spectrum for each earthquake in Figure 5.10 to its teleseismic spectrum in Figure 5.1. Ideally, they should be equal. Note that the strong motion spectra are plotted to 2 Hz, while the teleseismic spectra are plotted to 1 Hz. The strong motion spectrum of the Akita-Oki earthquake is 3 to 4 times larger than the teleseismic spectrum. This discrepancy is not really surprising when one considers the uncertainties about the siting of the Japanese accelerographs, and the unknown and complicated structure in that region. The strong motion spectrum of the Michoacan earthquake, however, agrees to within a factor of 2 with its teleseismic spectrum except at 0.1 to 0.03 Hz. At those low frequencies the digital strong motion data are still

reliable, but a near-field geometrical effect may be important. The bump at those frequencies in the Michoacan teleseismic spectrum may be due to the interference of the two subevents about 25 sec apart in time, which are seen clearly in the teleseismic records (Figures 3.2 and 4.4). Only one subevent is seen in the strong motion displacements (integrated by John Anderson, unpublished data) except at station La Villita midway between the two asperities. So, the agreement of the strong motion spectrum with the teleseismic spectrum of the Michoacan earthquake is encouraging.

Figure 5.10 shows that the level of the Akita-Oki strong motion spectrum is 3 to 4 times higher than that of Michoacan. This is greater than the factor of 1.5 that the Akita-Oki teleseismic spectrum is higher than that of Michoacan (Figure 5.1). It is quite possible that part of the difference between the Akita-Oki and the Michoacan strong motions may be due to site conditions. The stations of the Guerrero array are mostly located on competent rock. The Japanese strong motion stations are probably not. Nonetheless, the fairly good agreement between the teleseismic and strong motion spectral levels of the Michoacan earthquake, as well as the consistency between the relative spectral levels of the teleseismic and strong motions between the two earthquakes is quite striking and encouraging. It suggests that teleseismic records, which are relatively abundant, may indeed be used to infer properties of strong motions from large earthquakes.

--

## 5.5   References

Anderson, J. G., P. Bodin, J. N. Brune, J. Prince, S. K. Singh, R. Quaas, and M. Onate, Strong ground motion from the Michoacan, Mexico earthquake, *Science, 233*, 1043-1049, 1986.

Brune, J. N., Tectonic stress and the spectra of seismic shear waves from earthquakes, *J. Geophys. Res., 75*, 4997-5009, 1970.

Heaton, T. H., F. Tajima, and A. Wildenstein-Mori, Estimating ground motions using recorded accelerograms, *Surveys in Geophysics, 8*, 25-83, 1986.

Houston, H., and H. Kanamori, Source spectra of great earthquakes: teleseismic constraints on rupture process and strong motion, *Bull. Seism. Soc. Am., 76*, 19-42, 1986.

Sato, T., Rupture characteristics of the 1983 Nihonkai-Chubu (Japan Sea) earthquake as inferred from strong motion accelerograms, *J. Phys. Earth, 33*, 525-557, 1985.

# Appendix

1964MAR28        ALASKA

|     | DIST  | AZIM   | AMP   | PERIOD | CODA | TMAX | MB   |
|-----|-------|--------|-------|--------|------|------|------|
| ANP | 68.76 | 283.59 | 25.23 | 2.10   | 4.50 | 1.20 | 8.08 |
| ATL | 48.50 | 94.88  | 7.50  | 1.75   | 5.50 | 2.00 | 7.53 |
| ATU | 81.03 | 7.02   | 8.67  | 1.75   | 6.00 | 1.80 | 7.50 |
| BOG | 77.99 | 102.37 | 13.09 | 2.10   | 6.00 | 1.20 | 7.70 |
| CAR | 76.31 | 93.11  | 9.17  | 1.75   | 6.00 | 1.60 | 7.62 |
| ESK | 60.55 | 22.53  | 17.50 | 1.75   | 4.50 | 0.80 | 7.90 |
| HKC | 74.66 | 288.16 | 7.00  | 1.75   | 6.00 | 0.90 | 7.40 |
| IST | 78.18 | 2.71   | 9.17  | 1.75   | 6.00 | 0.80 | 7.62 |
| KEV | 49.38 | 2.51   | 11.08 | 1.75   | 5.50 | 1.00 | 7.60 |
| KTG | 43.31 | 23.58  | 9.83  | 1.75   | 6.00 | 1.20 | 7.25 |
| LUB | 40.11 | 112.14 | 16.67 | 1.75   | 6.50 | 3.20 | 7.38 |
| PDA | 70.76 | 45.51  | 26.67 | 1.75   | 4.50 | 0.90 | 8.08 |
| QUI | 79.80 | 108.45 | 9.27  | 1.40   | 6.00 | 1.80 | 7.52 |
| RAB | 79.84 | 241.69 | 7.50  | 1.75   | 6.00 | 2.00 | 7.33 |
| SHA | 48.92 | 100.47 | 32.37 | 2.10   | 4.50 | 1.20 | 7.99 |
| STU | 68.90 | 16.24  | 11.66 | 2.10   | 6.00 | 2.00 | 7.74 |
| TOL | 75.06 | 28.31  | 20.23 | 2.10   | 6.00 | 0.80 | 7.78 |
| VAL | 62.27 | 28.35  | 10.67 | 1.75   | 5.50 | 1.50 | 7.79 |
| UME | 55.06 | 6.60   | 5.84  | 1.47   | 6.00 | 1.20 | 7.40 |
| AVE |       |        |       | 1.81   | 5.63 | 1.43 | 7.64 |
| DEV |       |        |       | 0.20   | 0.62 | 0.59 | 0.24 |

1965FEB04   RAT ISLAND

| | DIST | AZIM | AMP | PERIOD | CODA | TMAX | MB |
|---|---|---|---|---|---|---|---|
| ANP | 50.32 | 261.21 | 7.19 | 2.22 | 5.00 | 0.70 | 7.21 |
| ATU | 88.42 | 340.39 | 1.86 | 1.39 | 6.00 | 2.10 | 7.23 |
| NNA | 108.36 | 86.26 | 0.57 | 1.94 | 5.50 | 0.90 | 7.37 |
| AAE | 110.64 | 317.09 | 0.90 | 1.67 | 6.80 | 2.20 | 7.88 |
| KEV | 57.49 | 348.67 | 0.53 | 1.56 | 3.20 | 0.10 | 6.33 |
| WEL | 92.25 | 182.89 | 1.21 | 1.67 | 7.00 | 1.00 | 6.96 |
| AQU | 85.85 | 349.04 | 2.22 | 1.00 | 4.00 | 1.00 | 7.25 |
| ATL | 68.76 | 62.93 | 2.39 | 1.00 | 4.00 | 2.30 | 7.38 |
| BHP | 90.39 | 75.23 | 1.44 | 1.28 | 3.50 | 1.00 | 7.05 |
| CAR | 96.59 | 64.30 | 0.82 | 1.11 | 7.00 | 0.70 | 7.27 |
| ESK | 73.75 | 1.08 | 3.28 | 1.11 | 3.50 | 2.20 | 7.27 |
| HKC | 57.60 | 264.92 | 5.92 | 2.22 | 4.50 | 2.20 | 7.23 |
| HNR | 62.59 | 200.82 | 9.57 | 2.11 | 4.50 | 2.10 | 7.56 |
| NOR | 47.10 | 3.03 | 2.15 | 1.28 | 6.50 | 3.00 | 7.13 |
| PTO | 87.73 | 5.44 | 2.01 | 1.50 | 5.30 | 2.50 | 7.23 |
| LUB | 58.42 | 74.51 | 1.89 | 1.00 | 4.00 | 0.80 | 7.08 |
| CTA | 76.54 | 211.14 | 1.09 | 1.11 | 6.00 | 2.20 | 6.89 |
| AVE | | | | 1.48 | 5.08 | 1.59 | 7.19 |
| DEV | | | | 0.42 | 1.26 | 0.81 | 0.31 |

1963OCT13 KURILE ISLANDS

|      | DIST  | AZIM   | AMP   | PERIOD | CODA | TMAX | MB   |
|------|-------|--------|-------|--------|------|------|------|
| ATU  | 84.16 | 319.93 | 13.96 | 2.45   | 2.70 | 1.60 | 7.76 |
| ALQ  | 74.91 | 55.68  | 1.77  | 1.75   | 4.00 | 1.50 | 6.81 |
| AFI  | 68.21 | 139.25 | 1.94  | 1.89   | 2.80 | 1.00 | 7.01 |
| BKS  | 63.38 | 62.22  | 0.92  | 1.61   | 3.00 | 1.40 | 6.66 |
| GDH  | 64.90 | 8.89   | 12.90 | 2.31   | 3.00 | 1.70 | 7.75 |
| GEO  | 86.60 | 34.66  | 2.38  | 2.10   | 3.50 | 1.80 | 7.05 |
| IST  | 79.27 | 318.50 | 1.93  | 1.26   | 3.50 | 1.30 | 6.99 |
| KEV  | 58.25 | 339.83 | 1.67  | 1.26   | 4.50 | 1.40 | 6.92 |
| KIP  | 48.73 | 100.90 | 3.23  | 1.40   | 4.00 | 1.00 | 7.16 |
| LUB  | 78.54 | 53.87  | 3.51  | 1.54   | 2.70 | 1.50 | 7.16 |
| MAL  | 95.42 | 339.29 | 1.21  | 1.75   | 3.20 | 1.70 | 7.04 |
| LON  | 58.49 | 53.75  | 2.89  | 1.96   | 3.50 | 1.40 | 6.97 |
| NUR  | 65.81 | 333.60 | 6.78  | 1.89   | 2.50 | 1.40 | 7.56 |
| OXF  | 84.58 | 45.33  | 6.49  | 1.54   | 3.00 | 1.60 | 7.63 |
| PDA  | 97.64 | 356.21 | 1.43  | 2.10   | 3.00 | 1.50 | 7.33 |
| RAB  | 48.92 | 176.60 | 12.48 | 1.96   | 3.30 | 1.50 | 7.60 |
| SHA  | 88.26 | 46.79  | 3.45  | 1.40   | 3.00 | 1.40 | 7.49 |
| UME  | 64.51 | 337.66 | 2.99  | 1.40   | 3.50 | 1.60 | 7.33 |
| STU  | 80.47 | 334.63 | 5.66  | 1.61   | 3.30 | 1.60 | 7.25 |
| TOL  | 92.35 | 340.01 | 1.35  | 1.40   | 4.00 | 1.90 | 7.08 |
| AVE  |       |        |       | 1.73   | 3.30 | 1.49 | 7.23 |
| DEV  |       |        |       | 0.34   | 0.51 | 0.22 | 0.31 |

1977AUG19    SUMBAWA

|      | DIST  | AZIM   | AMP   | PERIOD | CODA | TMAX | MB   |
|------|-------|--------|-------|--------|------|------|------|
| AFI  | 67.99 | 100.55 | 11.43 | 2.22   | 3.00 | 0.80 | 7.71 |
| HLW  | 92.97 | 299.69 | 5.08  | 2.22   | 4.00 | 0.80 | 7.56 |
| SHK  | 47.45 | 16.05  | 3.00  | 1.11   | 3.50 | 0.80 | 7.33 |
| PRE  | 85.35 | 244.80 | 4.87  | 2.22   | 4.00 | 0.60 | 7.34 |
| HOW  | 44.57 | 318.61 | 51.08 | 1.83   | 3.50 | 0.80 | 8.15 |
| NDI  | 56.18 | 315.84 | 8.68  | 1.83   | 5.50 | 1.10 | 7.48 |
| MAT  | 51.01 | 20.56  | 2.27  | 1.83   | 8.00 | 1.10 | 6.79 |
| KOD  | 45.92 | 296.15 | 7.08  | 1.83   | 4.00 | 0.60 | 7.39 |
| AVE  |       |        |       | 1.89   | 4.44 | 0.82 | 7.47 |
| DEV  |       |        |       | 0.34   | 1.51 | 0.18 | 0.36 |

1968MAY16   TOKACHI-OKI

|     | DIST  | AZIM   | AMP  | PERIOD | CODA | TMAX | MB   |
|-----|-------|--------|------|--------|------|------|------|
| AAE | 95.02 | 286.38 | 1.22 | 1.67   | 4.00 | 1.10 | 7.06 |
| ADE | 75.61 | 183.97 | 2.10 | 1.28   | 5.00 | 1.60 | 7.12 |
| AKU | 72.78 | 352.10 | 4.20 | 1.28   | 2.00 | 1.20 | 7.42 |
| ATU | 84.10 | 316.34 | 3.60 | 1.11   | 2.50 | 1.10 | 7.51 |
| BKS | 69.32 | 57.50  | 4.93 | 1.78   | 3.50 | 1.20 | 7.44 |
| BLA | 92.53 | 33.60  | 1.47 | 1.67   | 8.00 | 1.50 | 7.15 |
| COL | 45.03 | 34.21  | 1.99 | 1.28   | 5.50 | 2.10 | 6.89 |
| COR | 64.85 | 52.01  | 3.77 | 1.28   | 3.00 | 1.20 | 7.47 |
| CTA | 60.72 | 176.93 | 2.41 | 1.78   | 6.00 | 1.60 | 7.03 |
| DAL | 88.01 | 46.95  | 1.77 | 1.39   | 3.00 | 1.40 | 7.21 |
| DUG | 73.69 | 50.81  | 0.97 | 1.50   | 5.50 | 0.80 | 6.61 |
| ESK | 80.02 | 341.37 | 2.85 | 1.39   | 3.00 | 1.30 | 7.01 |
| JER | 81.95 | 305.19 | 3.87 | 1.50   | 6.00 | 1.10 | 7.31 |
| LON | 64.54 | 49.38  | 2.19 | 1.39   | 4.00 | 1.20 | 7.20 |
| OXF | 90.61 | 41.14  | 2.56 | 1.28   | 3.50 | 1.30 | 7.40 |
| PMG | 50.17 | 175.18 | 3.43 | 1.83   | 5.00 | 1.60 | 6.97 |
| RAB | 45.58 | 167.71 | 7.85 | 1.39   | 3.50 | 1.30 | 7.55 |
| PTO | 94.49 | 339.16 | 1.01 | 1.39   | 3.00 | 1.40 | 6.96 |
| SCP | 90.46 | 30.05  | 2.28 | 1.39   | 3.50 | 1.50 | 7.22 |
| TAU | 83.49 | 177.10 | 3.24 | 1.56   | 2.80 | 1.50 | 7.32 |
| TUC | 80.10 | 55.80  | 1.96 | 1.83   | 3.00 | 1.50 | 6.73 |
| WES | 91.36 | 24.97  | 2.98 | 1.67   | 2.80 | 1.30 | 7.35 |
| AAM | 86.90 | 32.95  | 2.20 | 1.39   | 3.00 | 1.50 | 7.20 |
| OGD | 91.42 | 27.77  | 2.32 | 2.06   | 3.00 | 1.10 | 7.15 |
| GSC | 74.35 | 56.84  | 2.53 | 1.94   | 4.50 | 1.40 | 6.91 |
| LEM | 57.75 | 223.35 | 9.45 | 1.83   | 4.50 | 1.40 | 7.51 |
| KIP | 52.77 | 92.99  | 5.30 | 2.22   | 3.70 | 1.30 | 7.08 |
|     |       |        |      |        |      |      |      |
| AVE |       |        |      | 1.56   | 3.96 | 1.35 | 7.18 |
| DEV |       |        |      | 0.27   | 1.34 | 0.24 | 0.24 |

1969AUG11   KURILE IS.

|      | DIST  | AZIM   | AMP  | PERIOD | CODA | TMAX | MB   |
|------|-------|--------|------|--------|------|------|------|
| ADE  | 78.43 | 187.61 | 3.16 | 2.11   | 3.50 | 0.70 | 7.07 |
| AFI  | 67.95 | 137.21 | 1.69 | 1.67   | 3.00 | 0.50 | 7.01 |
| ATL  | 89.93 | 41.32  | 1.57 | 1.67   | 2.20 | 0.70 | 6.97 |
| CTA  | 63.18 | 181.63 | 1.34 | 1.83   | 5.00 | 0.80 | 6.77 |
| MUN  | 80.39 | 206.84 | 1.11 | 1.56   | 3.70 | 0.80 | 6.55 |
| PTO  | 93.21 | 342.37 | 1.09 | 1.67   | 2.00 | 0.40 | 7.01 |
| GSC  | 70.26 | 59.91  | 1.21 | 1.67   | 3.80 | 0.70 | 6.76 |
| HLW  | 86.74 | 308.83 | 2.71 | 1.67   | 4.00 | 1.00 | 7.21 |
| LUB  | 80.48 | 52.54  | 1.32 | 1.22   | 3.30 | 0.70 | 6.73 |
| AVE  |       |        |      | 1.67   | 3.39 | 0.70 | 6.90 |
| DEV  |       |        |      | 0.22   | 0.87 | 0.16 | 0.20 |

1979DEC12    COLOMBIA

|      | DIST   | AZIM   | AMP  | PERIOD | CODA | TMAX | MB   |
|------|--------|--------|------|--------|------|------|------|
| AKU  | 77.05  | 21.88  | 1.01 | 1.16   | 2.50 | 0.80 | 6.84 |
| SNA  | 87.14  | 160.68 | 1.44 | 1.36   | 3.70 | 1.20 | 7.02 |
| COL  | 79.51  | 336.21 | 1.09 | 1.36   | 5.00 | 1.10 | 6.60 |
| COR  | 57.72  | 324.12 | 3.95 | 1.50   | 2.50 | 0.90 | 7.22 |
| JCT  | 34.63  | 328.02 | 2.80 | 2.04   | 7.00 | 1.10 | 6.84 |
| GEO  | 37.18  | 3.01   | 4.83 | 2.04   | 3.00 | 1.60 | 6.87 |
| LUB  | 38.14  | 328.89 | 4.70 | 2.38   | 6.50 | 1.10 | 6.79 |
| MAL  | 77.03  | 52.78  | 1.84 | 1.36   | 2.20 | 0.80 | 7.03 |
| NUR  | 95.51  | 28.83  | 1.10 | 2.04   | 2.50 | 1.00 | 7.03 |
| OGD  | 39.52  | 5.68   | 1.97 | 2.04   | 5.00 | 1.20 | 6.39 |
| GSC  | 48.28  | 318.26 | 2.14 | 1.84   | 5.00 | 1.00 | 6.97 |
| PTO  | 74.54  | 47.74  | 1.68 | 1.50   | 3.30 | 0.60 | 6.85 |
| KTG  | 78.02  | 16.88  | 1.99 | 1.77   | 2.60 | 1.10 | 6.95 |
| SHA  | 30.09  | 344.86 | 2.83 | 1.02   | 3.70 | 1.40 | 7.04 |
| TRI  | 91.08  | 44.48  | 2.30 | 1.70   | 2.50 | 1.20 | 7.23 |
| WES  | 41.24  | 9.09   | 3.26 | 1.56   | 2.60 | 1.40 | 6.82 |
| AVE  |        |        |      | 1.67   | 3.72 | 1.09 | 6.91 |
| DEV  |        |        |      | 0.37   | 1.48 | 0.24 | 0.20 |

1976AUG16 MINDANAO ISLAND

|  | DIST | AZIM | AMP | PERIOD | CODA | TMAX | MB |
|-----|--------|--------|-------|--------|------|------|------|
| ATU | 94.35 | 308.77 | 2.36 | 1.50 | 2.00 | 0.90 | 7.30 |
| COP | 96.87 | 327.98 | 1.60 | 1.83 | 3.30 | 0.90 | 7.34 |
| GRM | 99.65 | 237.36 | 2.03 | 2.50 | 2.00 | 1.10 | 7.31 |
| GDH | 104.71 | 359.13 | 0.55 | 2.06 | 2.00 | 0.50 | 7.12 |
| IST | 89.82 | 311.11 | 0.97 | 1.28 | 2.80 | 0.90 | 6.88 |
| KEV | 86.68 | 339.76 | 11.24 | 3.33 | 2.50 | 0.90 | 7.53 |
| KIP | 76.50 | 69.54 | 7.50 | 2.50 | 3.50 | 1.10 | 7.38 |
| MSH | 65.87 | 306.97 | 1.37 | 1.28 | 3.20 | 0.80 | 7.03 |
| MUN | 38.70 | 190.75 | 6.93 | 1.89 | 4.00 | 1.30 | 6.96 |
| NAI | 87.45 | 268.45 | 2.41 | 1.67 | 2.80 | 1.10 | 7.16 |
| NUR | 89.29 | 330.78 | 14.20 | 2.78 | 1.90 | 1.00 | 7.71 |
| PRE | 97.92 | 244.93 | 1.72 | 2.50 | 2.60 | 1.10 | 7.34 |
| RAR | 79.41 | 112.84 | 1.57 | 1.50 | 3.20 | 1.20 | 6.82 |
| KTG | 100.21 | 348.98 | 1.45 | 1.83 | 1.90 | 1.00 | 7.30 |
| STU | 101.29 | 322.24 | 3.23 | 2.94 | 2.20 | 0.90 | 7.34 |
| TAB | 76.58 | 307.53 | 10.17 | 1.83 | 3.00 | 1.10 | 7.64 |
| AVE |  |  |  | 2.08 | 2.68 | 0.99 | 7.26 |
| DEV |  |  |  | 0.60 | 0.63 | 0.18 | 0.25 |

**1974OCT03**      **PERU**

|       | DIST  | AZIM   | AMP  | PERIOD | CODA | TMAX | MB   |
|-------|-------|--------|------|--------|------|------|------|
| AAM   | 54.51 | 354.48 | 5.67 | 1.67   | 3.30 | 0.40 | 7.33 |
| AKU   | 89.17 | 20.90  | 0.93 | 1.28   | 2.00 | 0.60 | 6.86 |
| BKS   | 65.03 | 322.16 | 1.60 | 1.39   | 3.00 | 1.00 | 7.06 |
| COL   | 92.78 | 336.31 | 0.91 | 1.28   | 3.00 | 0.90 | 7.05 |
| JCT   | 47.50 | 333.74 | 1.69 | 1.39   | 4.70 | 0.90 | 6.98 |
| ESK   | 91.25 | 33.41  | 1.79 | 1.94   | 2.00 | 0.30 | 7.06 |
| KIP   | 85.67 | 292.87 | 1.86 | 2.33   | 2.50 | 0.40 | 6.80 |
| SDB   | 88.03 | 104.75 | 2.40 | 2.78   | 3.00 | 0.60 | 7.04 |
| LUB   | 51.06 | 333.82 | 1.33 | 1.00   | 3.50 | 0.40 | 6.82 |
| LUB   | 51.06 | 333.82 | 2.32 | 1.56   | 3.50 | 1.20 | 6.87 |
| OGD   | 53.06 | 2.82   | 2.12 | 2.22   | 5.00 | 0.30 | 6.68 |
| OXF   | 47.78 | 346.81 | 2.25 | 1.11   | 4.00 | 0.80 | 7.21 |
| RAR   | 78.48 | 250.63 | 0.85 | 2.22   | 1.50 | 0.50 | 6.48 |
| SBA   | 83.36 | 191.09 | 8.64 | 2.78   | 3.50 | 0.70 | 7.49 |
| KTG   | 90.66 | 16.16  | 2.54 | 2.22   | 2.30 | 0.30 | 7.16 |
| VAL   | 86.08 | 34.95  | 8.77 | 3.33   | 2.00 | 0.30 | 7.32 |
| WIN   | 89.65 | 112.89 | 1.56 | 2.50   | 3.30 | 0.30 | 6.80 |
| AVE   |       |        |      | 1.94   | 3.06 | 0.58 | 7.00 |
| DEV   |       |        |      | 0.66   | 0.93 | 0.28 | 0.25 |

1980JUL17 SANTA CRUZ ISLAND

|      | DIST  | AZIM   | AMP  | PERIOD | CODA | TMAX | MB   |
|------|-------|--------|------|--------|------|------|------|
| ADE  | 33.27 | 223.17 | 2.58 | 1.36   | 2.20 | 0.50 | 6.98 |
| BKS  | 83.73 | 49.16  | 0.48 | 1.09   | 1.70 | 0.80 | 6.65 |
| COL  | 84.64 | 18.05  | 1.46 | 1.70   | 2.70 | 1.10 | 6.93 |
| COR  | 85.46 | 42.60  | 1.54 | 2.04   | 2.00 | 1.40 | 6.88 |
| DAV  | 44.56 | 293.73 | 4.39 | 2.04   | 3.40 | 1.00 | 7.03 |
| DUG  | 91.43 | 49.23  | 0.24 | 1.70   | 3.50 | 1.20 | 6.25 |
| GUA  | 33.20 | 320.49 | 1.59 | 1.02   | 2.50 | 0.80 | 6.89 |
| HKC  | 61.37 | 304.07 | 2.30 | 1.70   | 1.80 | 0.50 | 7.03 |
| KOD  | 90.66 | 280.26 | 0.35 | 1.36   | 2.50 | 0.50 | 6.51 |
| BOZ  | 93.63 | 44.22  | 1.02 | 2.99   | 2.40 | 1.00 | 6.63 |
| MAT  | 55.32 | 332.93 | 1.17 | 1.56   | 2.50 | 0.80 | 6.68 |
| MUN  | 49.44 | 238.54 | 2.51 | 1.43   | 1.50 | 0.50 | 7.05 |
| NDI  | 94.77 | 298.17 | 0.64 | 1.63   | 1.90 | 0.90 | 6.79 |
| RAR  | 33.92 | 109.42 | 0.96 | 1.50   | 2.50 | 0.80 | 6.51 |
| SBA  | 65.35 | 179.79 | 0.94 | 1.36   | 3.00 | 1.10 | 6.84 |
| ANP  | 57.21 | 311.08 | 4.65 | 2.52   | 2.00 | 0.70 | 7.07 |
| BAG  | 53.22 | 301.56 | 2.35 | 1.16   | 2.30 | 1.00 | 7.01 |
| CHG  | 72.91 | 294.24 | 0.63 | 1.70   | 2.70 | 1.00 | 6.47 |
| POO  | 95.80 | 287.62 | 1.01 | 1.56   | 1.70 | 0.90 | 7.11 |
| TAU  | 34.31 | 204.54 | 0.99 | 1.29   | 2.30 | 0.70 | 6.58 |
| AVE  |       |        |      | 1.64   | 2.35 | 0.86 | 6.79 |
| DEV  |       |        |      | 0.46   | 0.53 | 0.24 | 0.24 |

1978NOV29 OAXACA

|     | DIST  | AZIM   | AMP  | PERIOD | CODA | TMAX | MB   |
|-----|-------|--------|------|--------|------|------|------|
| AKU | 70.72 | 25.46  | 4.07 | 2.38   | 1.30 | 0.30 | 7.13 |
| AFI | 80.04 | 252.39 | 8.97 | 4.08   | 2.00 | 0.10 | 7.04 |
| ARE | 40.74 | 141.40 | 7.59 | 3.74   | 3.50 | 0.20 | 6.81 |
| BEC | 33.15 | 54.91  | 3.00 | 1.02   | 0.35 | 0.10 | 7.17 |
| BKS | 31.32 | 318.80 | 2.88 | 2.38   | 2.50 | 0.25 | 6.78 |
| COR | 36.25 | 327.11 | 1.76 | 1.36   | 3.00 | 0.40 | 6.71 |
| COL | 59.59 | 337.33 | 0.57 | 0.88   | 2.00 | 0.05 | 6.61 |
| ESK | 78.84 | 35.57  | 0.97 | 1.63   | 2.30 | 0.85 | 6.57 |
| KIP | 58.09 | 285.45 | 1.65 | 1.70   | 1.25 | 0.15 | 6.79 |
| KEV | 85.81 | 16.90  | 1.52 | 2.04   | 3.00 | 0.90 | 6.77 |
| NUR | 90.42 | 25.03  | 1.41 | 3.06   | 2.40 | 0.05 | 6.66 |
| OGD | 31.31 | 33.00  | 9.17 | 3.06   | 4.00 | 0.20 | 7.18 |
| PDA | 65.37 | 55.53  | 7.44 | 2.65   | 1.50 | 0.18 | 7.45 |
| PTO | 78.12 | 50.48  | 0.75 | 1.29   | 1.50 | 0.07 | 6.67 |
| STU | 88.13 | 39.55  | 1.36 | 2.38   | 3.30 | 0.80 | 6.86 |
| TRN | 34.64 | 94.53  | 1.83 | 1.36   | 2.10 | 0.37 | 6.83 |
| UME | 86.88 | 23.36  | 1.14 | 2.04   | 4.00 | 0.90 | 6.75 |
| AVE |       |        |      | 2.18   | 2.35 | 0.35 | 6.87 |
| DEV |       |        |      | 0.90   | 0.99 | 0.30 | 0.23 |

1979MAR14 PETATLAN

|     | DIST  | AZIM   | AMP  | PERIOD | CODA | TMAX | MB   |
|-----|-------|--------|------|--------|------|------|------|
| AKU | 71.51 | 25.70  | 4.23 | 2.10   | 0.80 | 0.35 | 7.20 |
| ANT | 50.90 | 142.49 | 1.71 | 1.69   | 2.50 | 0.30 | 6.70 |
| ARE | 44.79 | 137.14 | 1.43 | 1.90   | 2.00 | 0.25 | 6.58 |
| COP | 88.47 | 31.21  | 0.75 | 2.03   | 4.00 | 0.30 | 6.67 |
| COR | 32.69 | 330.50 | 2.02 | 1.56   | 2.00 | 0.45 | 6.81 |
| ESK | 80.43 | 35.01  | 1.26 | 1.36   | 1.20 | 0.45 | 6.67 |
| KEV | 85.83 | 15.86  | 1.60 | 2.03   | 2.00 | 0.39 | 6.80 |
| KIP | 53.26 | 283.98 | 1.36 | 1.36   | 2.60 | 0.40 | 6.70 |
| NNA | 38.03 | 138.59 | 0.80 | 2.03   | 3.89 | 0.20 | 6.10 |
| PDA | 68.44 | 55.73  | 1.67 | 1.22   | 2.00 | 0.40 | 7.13 |
| PTO | 80.83 | 49.83  | 1.17 | 2.03   | 2.50 | 0.14 | 6.56 |
| KTG | 70.16 | 20.63  | 4.00 | 2.44   | 1.90 | 0.16 | 7.11 |
| UME | 87.44 | 22.20  | 0.51 | 1.29   | 1.70 | 0.62 | 6.59 |
| TRN | 39.38 | 94.43  | 1.18 | 1.97   | 3.00 | 0.32 | 6.18 |
| OGD | 32.95 | 38.86  | 0.96 | 1.63   | 3.70 | 0.32 | 6.47 |
| BEC | 36.31 | 58.81  | 6.42 | 2.71   | 2.20 | 0.16 | 6.97 |
| GDH | 59.57 | 17.87  | 0.52 | 1.22   | 3.00 | 0.35 | 6.43 |
| COL | 56.59 | 338.30 | 5.02 | 2.03   | 1.70 | 0.30 | 7.19 |
| AVE |       |        |      | 1.81   | 2.37 | 0.32 | 6.71 |
| DEV |       |        |      | 0.41   | 0.85 | 0.12 | 0.31 |

1976JUL27 TANGSHAN

|  | DIST | AZIM | AMP | PERIOD | CODA | TMAX | MB |
|------|-------|--------|------|--------|------|------|------|
| AAE | 75.94 | 270.15 | 2.33 | 2.33 | 4.00 | 0.40 | 6.90 |
| AAM | 96.27 | 15.92 | 0.62 | 1.39 | 7.00 | 0.25 | 6.95 |
| ATU | 69.91 | 302.93 | 1.35 | 1.39 | 4.00 | 0.20 | 6.89 |
| BKS | 85.27 | 43.52 | 2.11 | 2.11 | 4.30 | 0.40 | 7.00 |
| MSO | 80.04 | 31.13 | 2.22 | 1.83 | 1.80 | 0.25 | 6.78 |
| DUG | 88.17 | 36.38 | 0.93 | 1.39 | 3.90 | 0.50 | 6.93 |
| GDH | 71.39 | 356.79 | 1.98 | 1.61 | 1.70 | 0.30 | 6.99 |
| KIP | 72.28 | 76.65 | 1.52 | 1.39 | 1.70 | 0.25 | 6.94 |
| MAL | 87.43 | 317.18 | 0.44 | 1.39 | 4.30 | 0.20 | 6.50 |
| SNG | 35.73 | 210.31 | 4.31 | 2.11 | 3.00 | 0.30 | 6.91 |
| MUN | 71.13 | 181.52 | 1.53 | 1.83 | 3.70 | 0.20 | 6.82 |
| PMG | 55.72 | 144.30 | 0.89 | 1.22 | 3.30 | 0.20 | 6.66 |
| PTO | 86.13 | 322.51 | 1.81 | 2.17 | 4.90 | 0.20 | 6.82 |
| VAL | 78.38 | 330.19 | 0.32 | 1.06 | 4.60 | 0.20 | 6.38 |
| WES | 98.08 | 6.89 | 0.07 | 1.11 | 4.00 | 0.30 | 6.29 |
| TAU | 86.24 | 158.79 | 0.95 | 1.56 | 3.10 | 0.35 | 6.69 |
| SHI | 53.70 | 280.80 | 1.67 | 1.28 | 2.40 | 0.17 | 6.92 |
| ALQ | 95.36 | 35.24 | 0.66 | 1.56 | 2.60 | 0.30 | 6.83 |
| COL | 56.76 | 30.57 | 0.91 | 1.06 | 3.20 | 0.50 | 6.74 |
| COP | 66.10 | 323.33 | 0.20 | 1.28 | 2.80 | 0.33 | 6.19 |
| MSH | 45.43 | 285.25 | 1.94 | 1.56 | 2.60 | 0.20 | 6.80 |
| AVE |  |  |  | 1.55 | 3.47 | 0.29 | 6.76 |
| DEV |  |  |  | 0.37 | 1.21 | 0.10 | 0.23 |

1976FEB04 GUATEMALA

|      | DIST  | AZIM   | AMP  | PERIOD | CODA | TMAX | MB   |
|------|-------|--------|------|--------|------|------|------|
| BKS  | 36.81 | 314.02 | 2.62 | 2.17   | 4.10 | 0.80 | 6.58 |
| MSO  | 39.88 | 335.04 | 2.14 | 1.94   | 4.00 | 1.90 | 6.44 |
| COL  | 63.16 | 335.93 | 1.03 | 1.28   | 2.80 | 0.55 | 6.81 |
| COR  | 41.02 | 322.44 | 1.93 | 1.67   | 4.30 | 1.10 | 6.56 |
| COP  | 83.97 | 33.90  | 0.93 | 1.28   | 3.30 | 0.60 | 6.86 |
| KEV  | 84.45 | 18.28  | 0.44 | 1.11   | 4.20 | 0.70 | 6.59 |
| KIP  | 65.12 | 286.79 | 1.69 | 1.56   | 4.00 | 0.50 | 7.04 |
| LON  | 41.46 | 326.02 | 0.59 | 1.28   | 4.00 | 2.10 | 6.17 |
| DAG  | 70.80 | 13.29  | 1.56 | 1.39   | 1.90 | 0.60 | 6.95 |
| NUR  | 88.06 | 26.92  | 0.49 | 1.50   | 4.50 | 0.90 | 6.61 |
| KTG  | 68.15 | 19.58  | 0.58 | 1.56   | 4.40 | 0.70 | 6.57 |
| STU  | 84.17 | 41.13  | 1.38 | 2.00   | 4.00 | 0.60 | 6.84 |
| TRI  | 88.04 | 43.16  | 0.47 | 1.17   | 2.20 | 0.80 | 6.70 |
| AFI  | 86.60 | 254.69 | 0.57 | 1.94   | 4.50 | 0.90 | 6.47 |
| TOL  | 76.75 | 51.98  | 1.15 | 1.67   | 4.00 | 1.30 | 6.74 |
| VAL  | 71.37 | 39.90  | 1.26 | 1.56   | 4.00 | 0.80 | 6.81 |
| WES  | 31.11 | 26.20  | 0.86 | 1.50   | 5.80 | 0.30 | 6.46 |
| AVE  |       |        |      | 1.56   | 3.88 | 0.89 | 6.66 |
| DEV  |       |        |      | 0.30   | 0.89 | 0.46 | 0.21 |

1976NOV24 TURKEY

|  | DIST | AZIM | AMP | PERIOD | CODA | TMAX | MB |
|---|---|---|---|---|---|---|---|
| BLA | 88.51 | 318.81 | 0.77 | 2.78 | 2.20 | 0.12 | 6.44 |
| LEM | 74.34 | 112.54 | 0.68 | 1.78 | 4.50 | 0.50 | 6.39 |
| MSO | 89.40 | 345.95 | 0.53 | 2.11 | 2.00 | 0.15 | 6.40 |
| DAV | 79.00 | 89.78 | 2.54 | 2.06 | 2.70 | 0.65 | 6.89 |
| GDH | 56.66 | 334.98 | 1.19 | 1.44 | 1.50 | 0.30 | 6.71 |
| KEV | 32.08 | 348.93 | 1.22 | 1.94 | 4.00 | 0.18 | 6.50 |
| MAT | 70.96 | 58.19 | 0.57 | 1.67 | 1.60 | 0.18 | 6.44 |
| SNG | 59.77 | 106.55 | 1.23 | 1.78 | 1.20 | 0.10 | 6.64 |
| DAG | 46.17 | 343.50 | 0.36 | 1.39 | 3.50 | 0.15 | 6.21 |
| POO | 32.94 | 119.84 | 0.72 | 1.67 | 3.00 | 0.22 | 6.34 |
| SHK | 68.33 | 62.64 | 2.68 | 2.11 | 1.00 | 0.26 | 7.10 |
| VAL | 39.28 | 307.42 | 1.64 | 1.78 | 1.90 | 0.10 | 6.37 |
| WIN | 66.28 | 207.22 | 0.60 | 1.33 | 1.00 | 0.13 | 6.66 |
| ATL | 93.46 | 318.94 | 0.29 | 1.56 | 1.70 | 0.20 | 6.47 |
| BAG | 69.51 | 85.20 | 1.51 | 1.67 | 1.20 | 0.12 | 6.86 |
| COL | 75.98 | 5.17 | 0.96 | 1.72 | 1.20 | 0.15 | 6.65 |
| PRE | 66.12 | 195.57 | 0.82 | 1.44 | 0.90 | 0.20 | 6.75 |
| AVE | | | | 1.78 | 2.06 | 0.22 | 6.58 |
| DEV | | | | 0.34 | 1.07 | 0.14 | 0.23 |

1967JUL22   TURKEY

|      | DIST  | AZIM   | AMP  | PERIOD | CODA | TMAX | MB   |
|------|-------|--------|------|--------|------|------|------|
| ALQ  | 95.06 | 325.88 | 0.10 | 1.78   | 3.00 | 0.25 | 5.94 |
| AAM  | 78.32 | 316.35 | 0.36 | 1.22   | 1.80 | 0.15 | 6.37 |
| ANP  | 74.65 | 69.97  | 0.84 | 1.39   | 2.20 | 0.28 | 6.58 |
| ATL  | 85.02 | 310.48 | 0.75 | 1.28   | 0.70 | 0.10 | 6.77 |
| BAG  | 79.42 | 77.52  | 0.75 | 1.17   | 1.20 | 0.22 | 6.61 |
| BEC  | 73.40 | 298.47 | 0.96 | 2.11   | 2.00 | 0.10 | 6.56 |
| BLA  | 80.09 | 310.88 | 0.39 | 1.67   | 3.00 | 0.10 | 6.07 |
| BOZ  | 87.74 | 334.56 | 0.20 | 1.11   | 2.00 | 0.20 | 6.37 |
| BUL  | 60.52 | 182.24 | 0.43 | 1.33   | 2.20 | 0.14 | 6.41 |
| CAR  | 88.94 | 282.86 | 0.29 | 1.28   | 2.00 | 0.33 | 6.35 |
| CHG  | 61.68 | 88.96  | 0.90 | 1.67   | 1.40 | 0.20 | 6.73 |
| COL  | 74.77 | 359.33 | 0.76 | 1.44   | 1.60 | 0.24 | 6.52 |
| DAL  | 92.24 | 318.04 | 0.55 | 1.78   | 2.00 | 0.20 | 6.59 |
| DUG  | 92.93 | 332.86 | 0.11 | 1.11   | 1.70 | 0.10 | 6.21 |
| FLO  | 84.36 | 317.73 | 0.72 | 1.67   | 1.70 | 0.22 | 6.64 |
| GDH  | 50.67 | 332.71 | 1.47 | 1.94   | 2.00 | 0.10 | 6.58 |
| GEO  | 77.01 | 310.30 | 0.90 | 1.61   | 1.70 | 0.10 | 6.65 |
| GOL  | 90.55 | 327.63 | 0.14 | 1.44   | 2.30 | 0.20 | 6.08 |
| KTG  | 39.95 | 335.32 | 0.40 | 1.06   | 2.50 | 0.15 | 5.97 |
| LON  | 89.58 | 341.48 | 0.40 | 2.22   | 2.70 | 0.22 | 6.25 |
| NAI  | 42.11 | 170.87 | 0.20 | 1.17   | 2.90 | 0.50 | 5.72 |
| NDI  | 39.66 | 92.64  | 1.84 | 1.67   | 2.70 | 0.42 | 6.44 |
| AVE  |       |        |      | 1.51   | 2.06 | 0.21 | 6.38 |
| DEV  |       |        |      | 0.32   | 0.58 | 0.10 | 0.28 |

1971 SAN FERNANDO FEB 9

|      | DIST  | AZIM   | AMP  | PERIOD | CODA | TMAX | MB   |
|------|-------|--------|------|--------|------|------|------|
| MAT  | 79.72 | 307.24 | 0.63 | 1.39   | 0.55 | 0.03 | 6.36 |
| BLA  | 30.76 | 73.67  | 0.96 | 1.50   | 1.70 | 0.18 | 6.50 |
| ARE  | 67.40 | 130.68 | 0.63 | 1.39   | 0.80 | 0.02 | 6.66 |
| NAT  | 87.17 | 98.51  | 0.30 | 1.39   | 0.80 | 0.02 | 6.33 |
| NUR  | 80.69 | 17.56  | 0.72 | 1.06   | 0.20 | 0.03 | 6.63 |
| OGD  | 34.93 | 65.89  | 0.75 | 1.17   | 0.45 | 0.02 | 6.51 |
| PTO  | 80.94 | 46.05  | 0.20 | 1.00   | 0.55 | 0.02 | 6.10 |
| PEL  | 80.71 | 141.06 | 0.59 | 1.39   | 1.00 | 0.02 | 6.43 |
| STU  | 84.98 | 31.74  | 0.29 | 1.33   | 1.20 | 0.02 | 6.34 |
| TOL  | 84.42 | 44.81  | 0.86 | 1.33   | 0.40 | 0.02 | 6.81 |
| TRI  | 89.33 | 31.37  | 0.12 | 1.56   | 0.80 | 0.02 | 5.88 |
| UME  | 76.77 | 17.54  | 0.63 | 1.11   | 0.35 | 0.03 | 6.65 |
| ANT  | 73.55 | 134.80 | 0.45 | 1.17   | 0.70 | 0.02 | 6.39 |
| BHP  | 43.63 | 116.24 | 0.36 | 1.00   | 1.50 | 0.04 | 6.05 |
| CAR  | 52.48 | 104.23 | 0.44 | 1.00   | 0.70 | 0.02 | 6.35 |
| GIE  | 42.54 | 135.93 | 0.90 | 1.17   | 0.25 | 0.02 | 6.39 |
| HNR  | 88.49 | 257.60 | 0.79 | 1.22   | 1.50 | 0.02 | 6.91 |
| KIP  | 37.13 | 260.16 | 1.08 | 1.17   | 0.50 | 0.02 | 6.47 |
| KTG  | 60.10 | 22.74  | 0.48 | 1.17   | 0.80 | 0.02 | 6.41 |
| AKU  | 63.19 | 27.16  | 0.22 | 1.11   | 0.60 | 0.02 | 6.19 |
| AFI  | 69.87 | 236.16 | 0.32 | 1.72   | 0.80 | 0.03 | 6.17 |
| COP  | 80.94 | 25.74  | 0.48 | 1.17   | 0.80 | 0.02 | 6.41 |
| ESK  | 74.90 | 32.41  | 0.31 | 1.33   | 1.50 | 0.02 | 6.17 |
| GDH  | 49.40 | 25.14  | 1.06 | 1.67   | 1.70 | 0.20 | 6.60 |
| KEV  | 73.12 | 11.93  | 0.36 | 1.00   | 0.30 | 0.02 | 6.45 |
| COL  | 35.33 | 338.74 | 0.56 | 1.17   | 1.00 | 0.03 | 6.38 |
| AVE  |       |        |      | 1.26   | 0.82 | 0.03 | 6.41 |
| DEV  |       |        |      | 0.20   | 0.44 | 0.04 | 0.23 |

19790CT15   IMPERIAL VALLEY

|      | DIST  | AZIM   | AMP  | PERIOD | CODA | TMAX | MB   |
|------|-------|--------|------|--------|------|------|------|
| ARE  | 64.34 | 132.50 | 0.10 | 1.36   | 1.90 | 0.25 | 5.86 |
| ANT  | 70.52 | 136.65 | 0.15 | 1.36   | 1.80 | 0.20 | 5.94 |
| BOG  | 47.53 | 116.97 | 0.20 | 1.22   | 1.40 | 0.20 | 6.12 |
| CAR  | 49.59 | 105.03 | 0.16 | 1.22   | 1.50 | 0.15 | 5.82 |
| COL  | 37.90 | 338.12 | 0.50 | 1.70   | 1.80 | 0.30 | 5.97 |
| KTG  | 60.76 | 22.69  | 0.34 | 1.90   | 1.80 | 0.30 | 6.15 |
| KON  | 77.49 | 25.24  | 0.20 | 1.84   | 2.00 | 0.25 | 5.94 |
| LPS  | 30.02 | 121.30 | 0.19 | 2.04   | 2.10 | 0.40 | 5.57 |
| NNA  | 57.62 | 133.85 | 0.09 | 1.36   | 1.20 | 0.20 | 5.61 |
| NUR  | 81.58 | 18.76  | 0.22 | 2.04   | 1.60 | 0.30 | 5.93 |
| DAG  | 60.00 | 15.32  | 0.15 | 1.36   | 1.90 | 0.20 | 5.84 |
| SJG  | 46.34 | 95.78  | 0.37 | 1.77   | 3.00 | 0.45 | 6.12 |
| STU  | 85.11 | 33.13  | 0.09 | 1.27   | 1.40 | 0.20 | 5.84 |
| UME  | 77.67 | 18.54  | 0.15 | 1.56   | 2.00 | 0.30 | 5.89 |
| LOR  | 83.53 | 36.76  | 0.17 | 1.29   | 1.60 | 0.20 | 6.12 |
| KEV  | 74.31 | 12.76  | 0.27 | 2.04   | 1.50 | 0.25 | 5.93 |
| LPB  | 66.55 | 129.87 | 0.13 | 1.84   | 2.00 | 0.80 | 5.86 |
| MAL  | 85.56 | 48.83  | 0.12 | 1.77   | 1.50 | 0.50 | 5.75 |
| MAT  | 82.79 | 308.87 | 0.21 | 1.36   | 1.30 | 0.30 | 6.19 |
| AVE  |       |        |      | 1.60   | 1.75 | 0.30 | 5.92 |
| DEV  |       |        |      | 0.29   | 0.39 | 0.15 | 0.17 |